Non-Uniform Radial Meanline Method for Off-Design Performance Estimation of Multistage Axial Compressors

by

David Andrew Birkenheier

B.S.E., Aerospace Engineering, University of Michigan (2015)

Submitted to the Department of Aeronautics and Astronautics
in partial fulfillment of the requirements for the degree of

Master of Science in Aeronautics and Astronautics

at the

MASSACHUSETTS INSTITUTE OF TECHNOLOGY

June 2018

Signature redacted

Author .....
Department of Aeronautics and Astronautics
May 25, 2018

Signature redacted

Certified by .....
Zoltán Spakovszky
Professor of Aeronautics and Astronautics
Thesis Supervisor

Signature redacted

Accepted by .....
Hamsa Balakrishnan
Associate Professor of Aeronautics and Astronautics
Chair, Graduate Program Committee

Non-Uniform Radial Meanline Method for Off-Design Performance Estimation of Multistage Axial Compressors

by

David Andrew Birkenheier

Submitted to the Department of Aeronautics and Astronautics
on May 25, 2018, in partial fulfillment of the
requirements for the degree of
Master of Science in Aeronautics and Astronautics

Abstract

The increasing use of renewable energy sources necessitates power-generating gas turbines capable of frequently and rapidly starting up to supplement the energy supply when renewable sources alone cannot meet demand [1], [2]. This makes the off-design performance of such gas turbines more important as they spend more of their operational life off the design point. Currently off-design performance cannot be estimated with high fidelity until late in the gas turbine compressor design process at which point the design is largely fixed and only limited changes can be made. This thesis presents a Non-Uniform Radial Meanline method for multistage axial compressor off-design performance estimation, capturing the transfer of radial flow non-uniformity and its impact on compressor blade row performance. This method enables the high-fidelity characterization of blade row performance and the stage matching of multistage compressors with non-uniformity effects included.

A new representation of non-uniform radial flow profiles using orthonormal basis functions was developed to provide a compact representation suitable for inclusion in a one-dimensional performance estimation method. The link between radial flow non-uniformity and compressor blade row performance was characterized using three-dimensional embedded stage calculations. An initial implementation of the Non-Uniform Radial Meanline method was demonstrated for different compressor inlet non-uniformities. The computations show that the new approach provides an effective means of incorporating radial flow non-uniformity into a one-dimensional compressor performance estimation method.

Thesis Supervisor: Zoltán Spakovszky
Title: Professor of Aeronautics and Astronautics

Acknowledgments

I would like to express my deep gratitude for Professor Spakovszky's guidance on this work and the truly exceptional experience he has given me in the GTL. Professor Greitzer also has my deepest gratitude for his invaluable guidance. I would like to thank Professor Cumpsty for his insightful contributions during his visits to the lab, and especially for coining the NURM name.

My thanks to Mitsubishi Heavy Industries for their sponsorship of this project and their advice over the phone and in person at the workshops, and to Mr. Tom Walker for his contributions every week.

My thanks to the grad students of the GTL. Alex, for getting me up to speed during my first few weeks and for the thought-provoking conversations over the past year. Andras and Jinwook, for keeping the computers running. Reed, for your mathematical insights. In Young, Yuan Kang, Javier, Vaishnavi, Jonas, Aurélien, Aidan, Denis, William, Tom, thank you all for the conversations and camaraderie.

And my thanks to my parents Jane and John and my sister Anna. The older I get the clearer it becomes how indispensable your support has always been and continues to be.

Contents

List of Figures

List of Tables

Nomenclature

$\dot{m}$	mass flow rate
$\hat{f}$	orthonormal basis function
A	area
b	basis function coefficient
f	basis function representation of radial flow profile
g	weighted polynomial
h	enthalpy
i	incidence
k_a	non-uniformity transfer function
k_b	blockage factor
M	mach number
N	non-uniformity parameter or corrected rotor speed
P	pressure
R	specific gas constant
r	radius

SH shape parameter

T temperature

U blade speed

V velocity in absolute frame

W velocity in relative frame

Subscripts

abs absolute reference frame

eff effective

inc incidence

$isen$ isentropic

$mean$ meanline

rel relative reference frame

t stagnation state

x axial

Greek Symbols

α absolute flow angle

β relative flow angle

χ blade metal angle

δ deviation angle

η efficiency

γ ratio of specific heats

Ω rotor angular velocity [rad/s]

ω stagnation pressure loss coefficient

ϕ flow coefficient

π overall compressor pressure ratio

ψ work coefficient

ρ density

Superscripts

$-$ 1D meanline value

$\hat{}$ normalized

Chapter 1

Introduction

1.1 Problem Definition

Renewable energy sources make up an increasing proportion of the overall energy system [1]. The inherent intermittent nature of wind and solar energy necessitates conventional power sources capable of frequently and rapidly ramping up and down to meet demand when renewable sources alone are not sufficient [1], [2]. Gas turbine power plants are thermally better suited to peaking operation than coal-fired power plants [3], presenting an opportunity for the power gas turbine industry to capitalize on the rise of renewable energy by meeting the need for flexible conventional power sources.

Conventional gas turbine power plants have traditionally run at their design operating point for extended periods of time with only infrequent shutdowns for maintenance. Before the advent of renewable sources, power generating gas turbines were designed to last 25,000 hours and 800 start-ups between major overhauls [4]. The design process has accordingly emphasized design point performance over transient operation. As a result, typical start up times for heavy-duty combined cycle gas turbines are as long as 4 hours for a cold start [2]. The increased importance of transient operations to accommodate renewable energy sources is setting new design requirements for power gas turbines with an increased emphasis on off-design performance.

This thesis is focused on an off-design performance estimation tool for multistage

axial compressors such as those used in power generating gas turbines. The compressor design process typically begins with meanline calculations to set the 1D design including meanline velocity triangles and number of stages [5]. A streamline curvature method is usually used to determine the radial flow profiles on a circumferentially-averaged basis, and 3D blades are designed to achieve the required radial flow profiles. Off-design performance assessment in the early stages of the design process has been a long-standing challenge [6]. Currently off-design performance cannot be estimated with high fidelity until late in the design process when 3D computational fluid dynamics (CFD) computations can be run. At this point the design is largely fixed and only limited changes can be made to improve off-design performance.

One of the most important and challenging aspects of compressor design for both the design operating point and off-design conditions is stage matching [7]. In a properly matched compressor each stage operates at its intended condition (intended corrected flow per unit area and pressure rise) for a given overall compressor operating point. The pressure rise across each stage causes a density rise, and the stage outlet area must be sized to provide an appropriate inlet corrected flow per unit area for the downstream stage. Put another way, for a given swing in inlet corrected flow changes in exit corrected flow will be exacerbated leading to larger swings in incidence for the downstream stage. Any error in stage pressure rise estimation during the preliminary stages of design will result in improper gas path area distribution and improper corrected flow into downstream stages. This can have a significant impact on blade performance and might require a mjor redesign effort [5]. The primary challenge in matching stages at the design point is prediction of blockage [7]. Endwall boundary layers reduce the flow area, which increases the corrected flow per unit area. In spite of the importance of blockage prediction to compressor design, this is an ongoing area of research [7].

The challenges of stage matching are especially severe in the large, high pressure ratio compressors required for power generating gas turbines. Several design features have been developed to ameliorate these challenges [8]. Bleeds are used to remove flow from the compressor between stages, reducing the mass flow into the rear stages

and alleviating the choking at lower-than-design rotor speeds or inlet flows. Variable stator vanes are also used to set the proper corrected flow by controlling swirl. Modern aircraft engines also use multiple independent shafts to allow for higher rotor speeds in the rear stages than the front stages and alleviate the rear stage choking and front stage stalling at low rotor speeds. However, this design option is not feasible in large power generating gas turbines because the shaft must run at the cycle frequency of the electrical grid.

Radial flow non-uniformity plays an important role in stage matching because of the change in flow area caused by endwall boundary layers and because non-uniformity directly impacts blade row performance [6]. The impact of non-uniformity on performance is especially important at off-design conditions, particularly if stages choke or stall, and non-uniform outlet flows from one stage impact downstream stages [6].

In the current design process, stage matching is often set by a streamline curvature method. The challenges presented by off-design stage matching highlight the opportunity for improvement of the overall compressor design by incorporating off-design performance estimations into the early stages of the design process when the gas path is being determined.

As the importance of transient operation grows, there remains a lack of rigorous 1D or streamline curvature methods for off-design flows in power gas turbine compressors. In addition, there is a lack of feedback from the later, high-fidelity stages of the design process into the early stages where fundamental decisions such as meanline velocity triangles, number of stages and annulus area schedule are made. The off-design performance estimation method presented in this thesis incorporates radial flow non-uniformity and its impact on blade row performance into a 1D meanline framework, facilitating the estimation of off-design performance early in the design process. Blade row performance, the linkage between inlet flow non-uniformity and performance, and the transfer of non-uniformity through the compressor are characterized using 3D CFD computations to bring high-fidelity information upstream into the design process.

1.2 Previous Work

The importance of endwall boundary layer prediction in stage matching and performance estimation has motivated much research. Early models used empirical correlations based on previous compressors of similar design [5]. Smith [9] studied non-uniformity in a repeating stage environment, representative of stages in the mid or aft section of the compressor where the flow has reached an equilibrium such that the stage inlet profiles are repeated at the stage exit [10]. Blockage was quantified using the endwall boundary layer displacement thickness normalized by blade staggered spacing (the distance between blades measured perpendicular to the chord lines). The investigation found that blockage increased with tip clearance and with blade loading. Horlock [10] extended Smith's reasoning by using conservation of momentum across a repeating stage to explain the decrease in blockage across the "non-clearance" blade row of a repeating stage which balances the increase in blockage brought about by leakage flow across an unshrouded rotor or cantilevered stator.

Methods for explicit calculation of the endwall boundary layers in 2D streamline curvature methods have been developed such as those of Dunham [11], Gallimore [12], and Howard and Gallimore [13].

Khalid, et al., [14] developed a 1D method for quantifying blockage similar to boundary layer displacement thickness but with the velocity component in the integration set by the mainflow direction and with velocity gradients used to demarcate the defect region. This quantification was used to investigate the impact of tip leakage flow on blockage. Utilizing an analogy between tip leakage flow and a velocity defect passing through an adverse pressure gradient, it was shown that blockage can be represented as a function of a single loading parameter defined as the difference between the static pressure rise and the total pressure defect in the velocity defect region, both normalized by inlet freestream dynamic head.

Kulkarni [15] developed another 1D method for quantifying blockage by solving a closed form equation for effective area using corrected flow per unit area and mass flow rate. Corrected flow per unit area governs the performance of a compressor blade

row and is a function of only the Mach number and flow angle:

$$\frac{\dot{m}\sqrt{RT_t}}{AP_t\sqrt{\gamma}} = \frac{Mcos(\alpha)}{(1+\frac{\gamma-1}{2}M^2)^{\frac{\gamma+1}{2(\gamma-1)}}} \tag{1.1}$$

This equation must be satisfied for each streamtube. However, to be satisfied on a 1D average basis it requires an effective area A_{eff} less than the geometric annulus area because of the endwall blockage. The effective area varies with operating point, and can be calculated from the total and static pressure, total and static temperature, and flow angle at a station by using Equation 1.1 and the isentropic relations, given in Equation 1.2 below. The resulting effective area is given in Equation 1.3.

$$\frac{P}{P_t} = \left(1+\frac{\gamma-1}{2}M^2\right)^{-(\frac{\gamma}{\gamma-1})} \tag{1.2}$$

$$A_{eff} = \frac{\dot{m}\sqrt{RT_t}}{P_t\sqrt{\gamma}(\frac{P}{P_t})^{\frac{\gamma+1}{2\gamma}}cos(\alpha)\sqrt{\left((\frac{P}{P_t})^{-(\frac{\gamma-1}{\gamma})}-1\right)\frac{2}{\gamma-1}}} \tag{1.3}$$

Kulkarni then defined a blockage factor as:

$$k_b = 1 - \frac{A_{eff}}{A_{annulus}} \tag{1.4}$$

This quantification will be used in this thesis to capture blockage. Kulkarni incorporated blockage information into a 1D stage-stacking method by representing the blockage factor as a function of flow coefficient, using CFD results from points across the compressor operating map to determine the functional relationship. This method has the advantage of incorporating high-fidelity information from 3D CFD computations into the 1D phase of the design process. Joerger [16] adapted Kulkarni's for use in a meanline calculation. The method presented in this thesis builds on this by incorporating 2D radial flow non-uniformity into Joerger's 1D meanline framework.

Less is known about the impact of radial non-uniformity on performance apart from boundary layer effects. Robbins and Dugan note that inlet flow distortion influences stage performance but also note a lack of quantitative information available

on this phenomenon [6]. In the present thesis a non-uniformity parameter is introduced to quantitatively characterize the non-uniformity at each station. Using this quantification the variation in non-uniformity across the compressor operating map is assessed as shown in Figure 1-1. The link between radial flow non-uniformity and performance is characterized and quantified. It is confirmed that non-uniformity, or "maldistribution" in the words of Robbins and Dugan, has an appreciable impact on blade row performance. Three profiles of varying non-uniformity are show in Figure 1-2 at the inlet to an embedded rotor. At the same corrected flow on a 1D basis, the three profiles produce a 5% change in stagnation pressure loss coefficient and an 8% change in deviation angle, as shown in Figure 1-3. These findings motivate the incorporation of radial flow non-uniformity and its impact on performance into a 1D off-design performance estimation method.

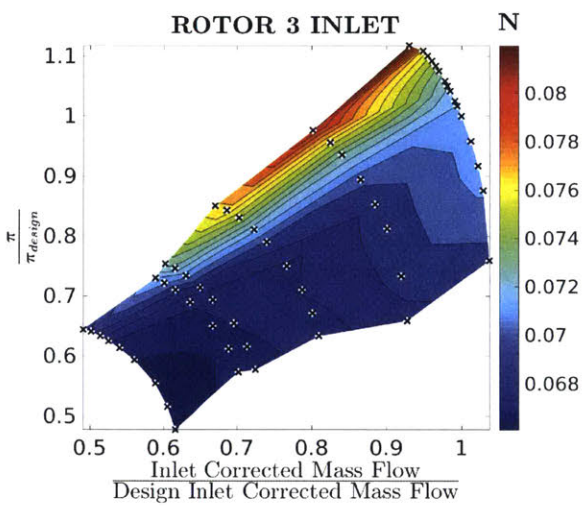

Figure 1-1: Non-uniformity varies across operating map, as shown by non-uniformity parameter N.

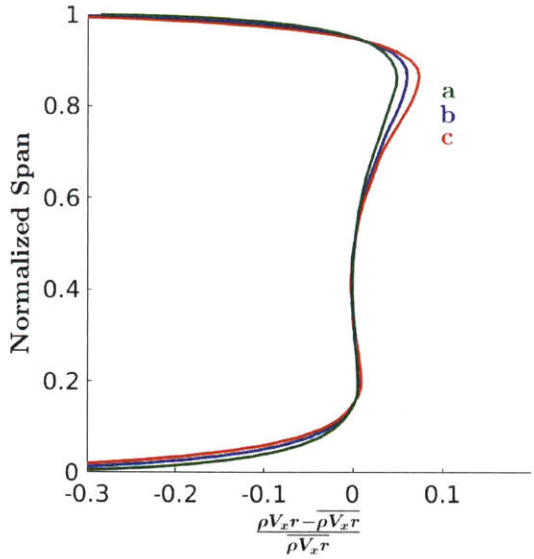

Figure 1-2: Profiles of varying non-uniformity at inlet to embedded compressor rotor.

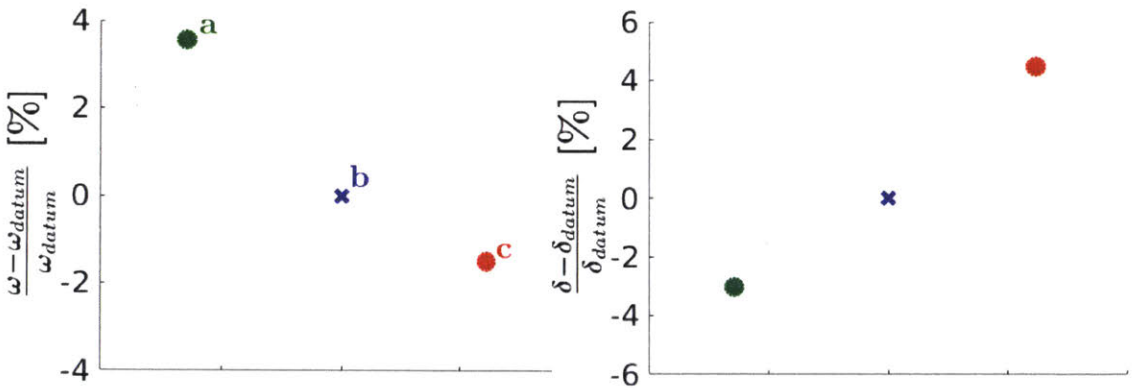

Figure 1-3: Variations in inlet radial flow non-uniformity have appreciable impact on blade row performance.

1.3 Objectives and Conceptual Approach

1.3.1 Non-Uniform Radial Meanline (NURM) Method

The main objective of this thesis is the development of a Non-Uniform Radial Meanline method for the estimation of the off-design performance of multistage axial compressors including the radial non-uniformity at each station and its impact on performance.

1.3.2 Conceptual Approach

The off-design performance estimation method is based on a meanline calculation framework. The approach is sketched in Figure 1-4. Blade row performance is characterized by stagnation pressure loss coefficient, deviation angle, and radial flow non-uniformity. The impact of non-uniformity is accounted for in the loss coefficient, deviation angle, and blockage. The blade row outlet meanline conditions are calculated based on the upstream conditions using continuity, conservation of rothalpy, and velocity triangles. The transfer of non-uniformity across each blade row sets the inlet non-uniformity of the downstream blade row. The blade row loss coefficient and deviation angle characteristics are determined using multi-stage steady 3D Reynolds-Averaged Navier-Stokes (RANS) CFD computations. The link between non-uniformity and performance and the transfer of non-uniformity across each blade row is characterized using embedded stage 3D RANS computations. This brings information from high-fidelity 3D computations into the early stages of the design process.

1.3.3 Research Objectives

This thesis adresses the following objectives:

- Capture radial flow non-uniformity in a compact manner suitable for incorporation into a meanline framework
- Characterize the link between non-uniformity and performance
- Capture the transfer of non-uniformity through the compressor

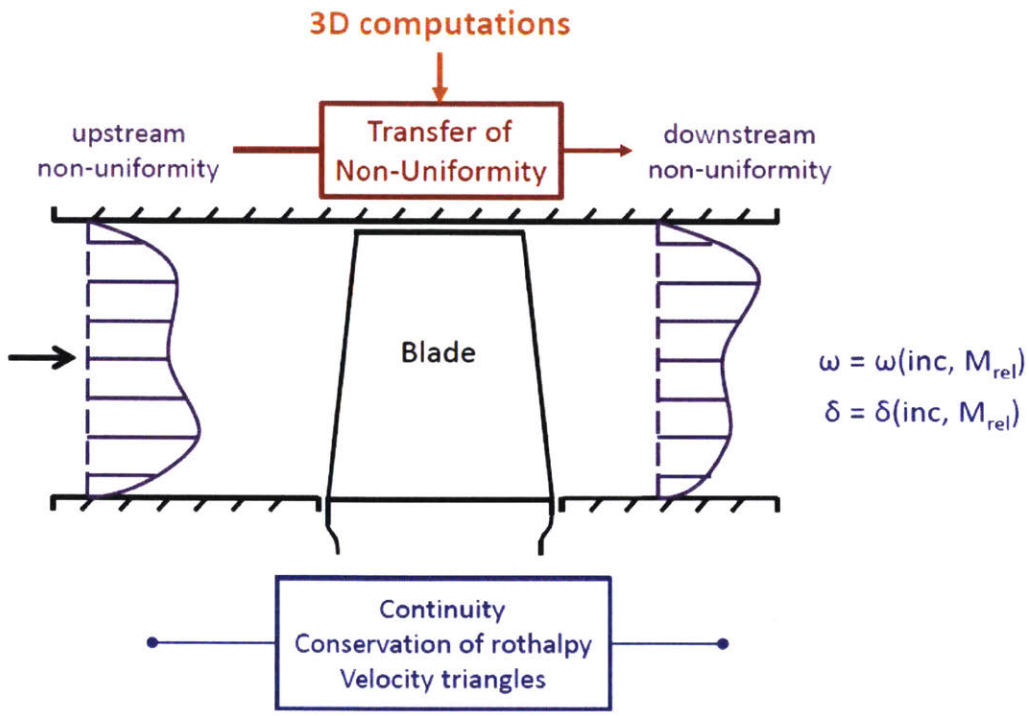

Figure 1-4: Non-Uniform Radial Meanline method captures non-uniformity, its impact on blade row performance, and its transfer across each blade row.

1.4 Thesis Contributions

Flow non-uniformity is characterized using a new parameter across a compressor operating map. A novel approach was developed for the representation of non-uniform radial flow profiles using a compact set of basis functions [1]. Embedded-stage CFD computations show this representation method effectively captures the radial profiles in a compressor. The linkage between non-uniformity and blade row performance is characterized using a sensitivity study. The transfer of non-uniformity across each blade row is captured via so-called transfer functions. These new elements were integrated into a meanline framework to enable the high-fidelity characterization of blade row performance and the stage matching of multi-stage compressors with non-uniformity effects included. The inclusion of radial flow profiles at each station also provides the possibility for future capabilities previously unavailable in a meanline

[1]The basis function formulation was conceived in discussion with Reed LaFleche [17]

method such as stall point assessment on a blade row basis. A preliminary implementation of the method shows it effectively transfers non-uniformity through the compressor.

1.5 Organization of Thesis

This thesis is organized as follows: Chapter 2 gives a brief assessment of the radial flow non-uniformity present in a representative multistage axial compressor. Chapter 3 presents a method for the representation of radially non-uniform flow profiles using a set of orthonormal basis functions. Chapter 4 details the characterization of the link between non-uniformity and performance, including the transfer of non-uniformity across each blade row. A preliminary implementation of the NURM method is presented in Chapter 5 incorporating the developments of Chapters 3 and 4. Chapter 6 demonstrates the capabilities of the preliminary implementation. The conclusions of the thesis and suggested future work are provided in Chapter 7. In Appendix A a detailed description of the calculations used in the preliminary implementation to compute the conditions across a stage of the compressor is given.

1.6 Test Compressor

The CFD computations required for the assessment and characterization of non-uniformity and the formulation and demonstration of the preliminary implementation of the NURM method were performed using geometry from a four-stage compressor representative of the middle stages of a compressor of advanced design as used in a power gas turbine. The compressor has shrouded stators and does not include any bleed flows. The geometry is shown in Figure 1-5 below.

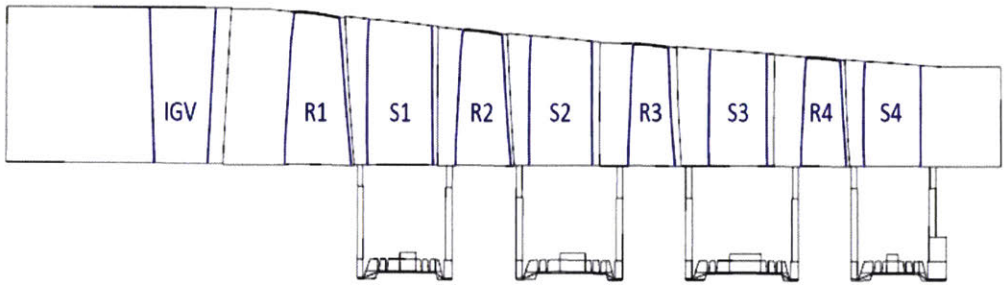

Figure 1-5: Test compressor geometry with underplatform cavities, no interstage bleeds.

Chapter 2

Non-Uniformity Assessment

To incorporate radial non-uniformity into an off-design performance estimation method, the characteristics of the non-uniformity and its trends through the compressor and across the operating map must be characterized. Radial profiles from the test compressor rotor 3 inlet are shown in Figure 2-1. By the third stage of the test compressor the flow is fully developed and is taken to be representative of an embedded stage in a power gas turbine compressor. The overall non-uniformity is made up of elements including endwall blockage, radial mass flow distribution, and tip leakage effects. The overall non-uniformity and its constituent elements vary across the operating map, which indicates that variation with operating point will need to be captured in the incorporation of non-uniformity into the performance estimation method.

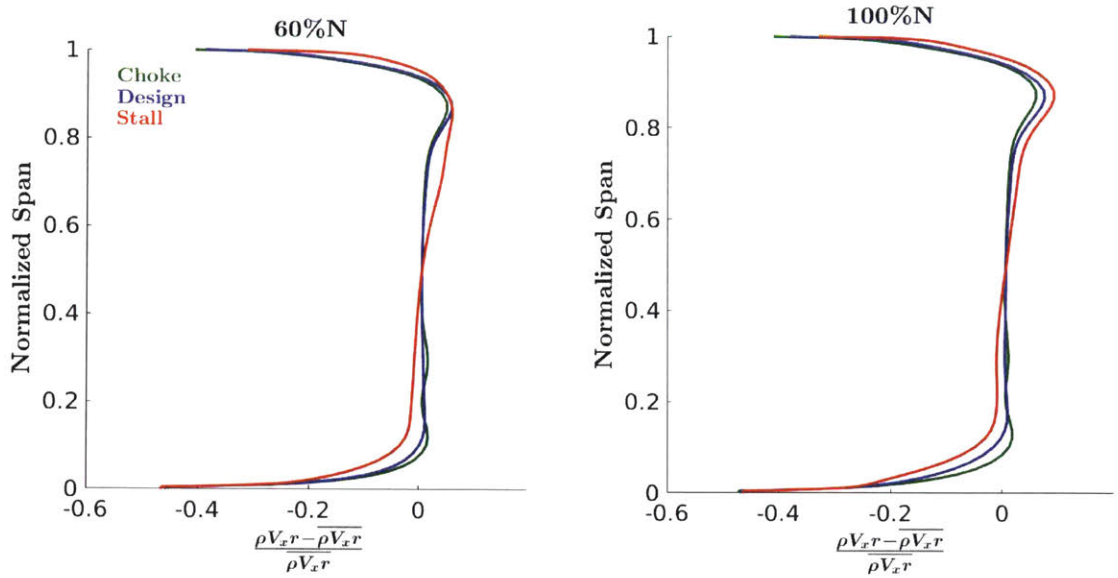

Figure 2-1: Test compressor rotor 3 inlet flow profiles show departures from average value vary across operating map. Variations must be characterized to incorporate non-uniformity into NURM.

2.1 Trends in Non-Uniformity Across Map and Through Compressor

To characterize the trends in non-uniformity across the compressor operating map, overall radial flow non-uniformity can be captured in a scalar using the Non-Uniformity Parameter N, defined as the root-mean square of departures from the average value of the mass flow rate per unit span profile, $\rho V_x r$:

$$N = \sqrt{\frac{1}{R_{max} - R_{min}} \int_{R_{min}}^{R_{max}} \left(\frac{\rho V_x r - \overline{\rho V_x r}}{\overline{\rho V_x r}} \right)^2 dr} \tag{2.1}$$

This characterization captures the non-uniformity of the radial distribution of streamtube mass flow and thus relates to the distribution of work done by the blade row.

The scalar characterization of non-uniformity allows for a quantitative assessment of its variation within a compressor. Figure 2-2 shows the variation in N across the operating map for rotor 3 inlet of the test compressor. The pressure rise and

corrected mass flow plotted are the overall compressor pressure rise and compressor inlet corrected mass flow. Contours of blade row stagnation pressure loss are shown in Figure 2-3 for comparison. It might be expected that non-uniformity would be lowest near the design point where performance is best. In fact, the non-uniformity increases from choke to stall and with increasing speed. The trends in non-uniformity are consistent with the stronger adverse pressure gradients near stall which increase the size of the endwall boundary layers and also with the higher blade loading near stall which increases the likelihood of regions of separated flow forming and causing non-uniformity. The trends in non-uniformity are also consistent with the profiles blockage and radial mass flow skew in Figure 2-1, both increasing from choke to stall.

Non-uniformity is higher at the stator inlet than the rotor inlet, indicating that non-uniformity is exacerbated across rotors and attenuated across stators. This is consistent with Horlock's [10] model of "non-clearance" rows reducing blockage to satisfy the repeating stage assumptions. Figure 2-4 shows the non-uniformity at all stator inlets. Non-uniformity increases in magnitude moving downstream through the compressor. This is indicative of the approximate nature of the repeating stage model because while the profiles at stage inlet and exit resemble each other, they continue to change slightly as the non-uniformity in the flow increases after each stage. All of these changes, with operating point, between rotor and stator, and moving downstream through the compressor, will need to be captured to properly incorporate non-uniformity into a performance estimation method.

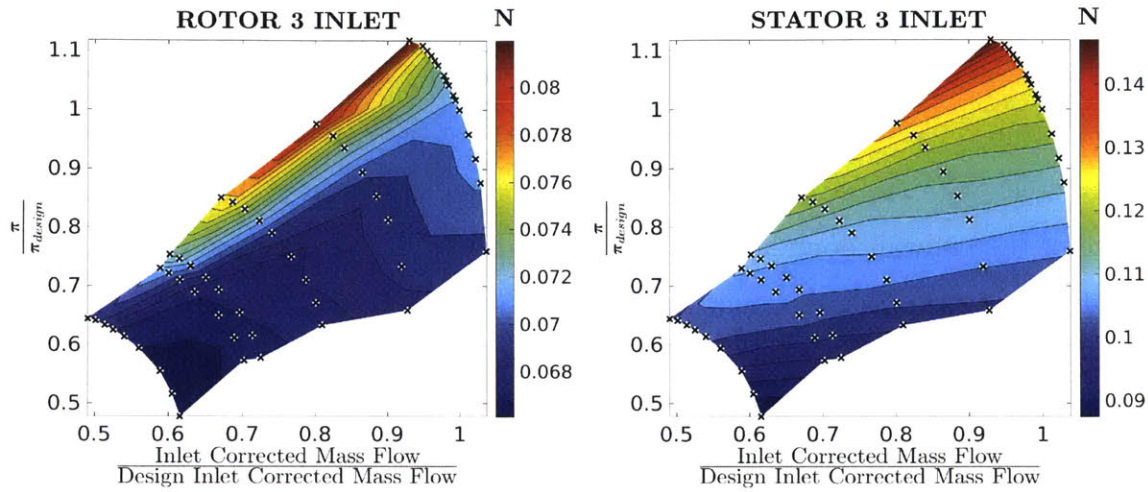

Figure 2-2: Level of flow non-uniformity varies across operating map. Stator inlet non-uniformity is greater than that at rotor inlet.

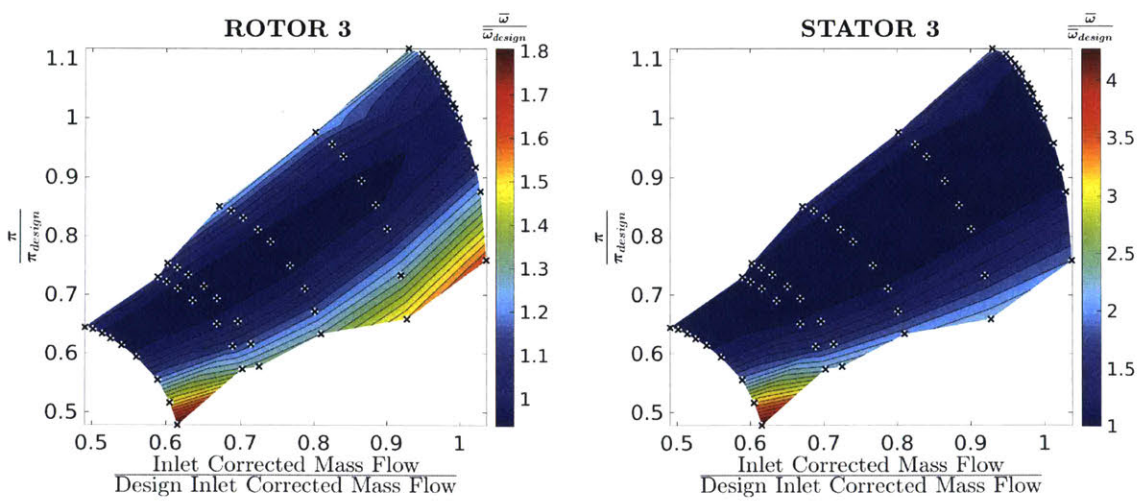

Figure 2-3: Low blade row inlet flow non-uniformity does not necessarily correspond to low stagnation pressure loss across blade row.

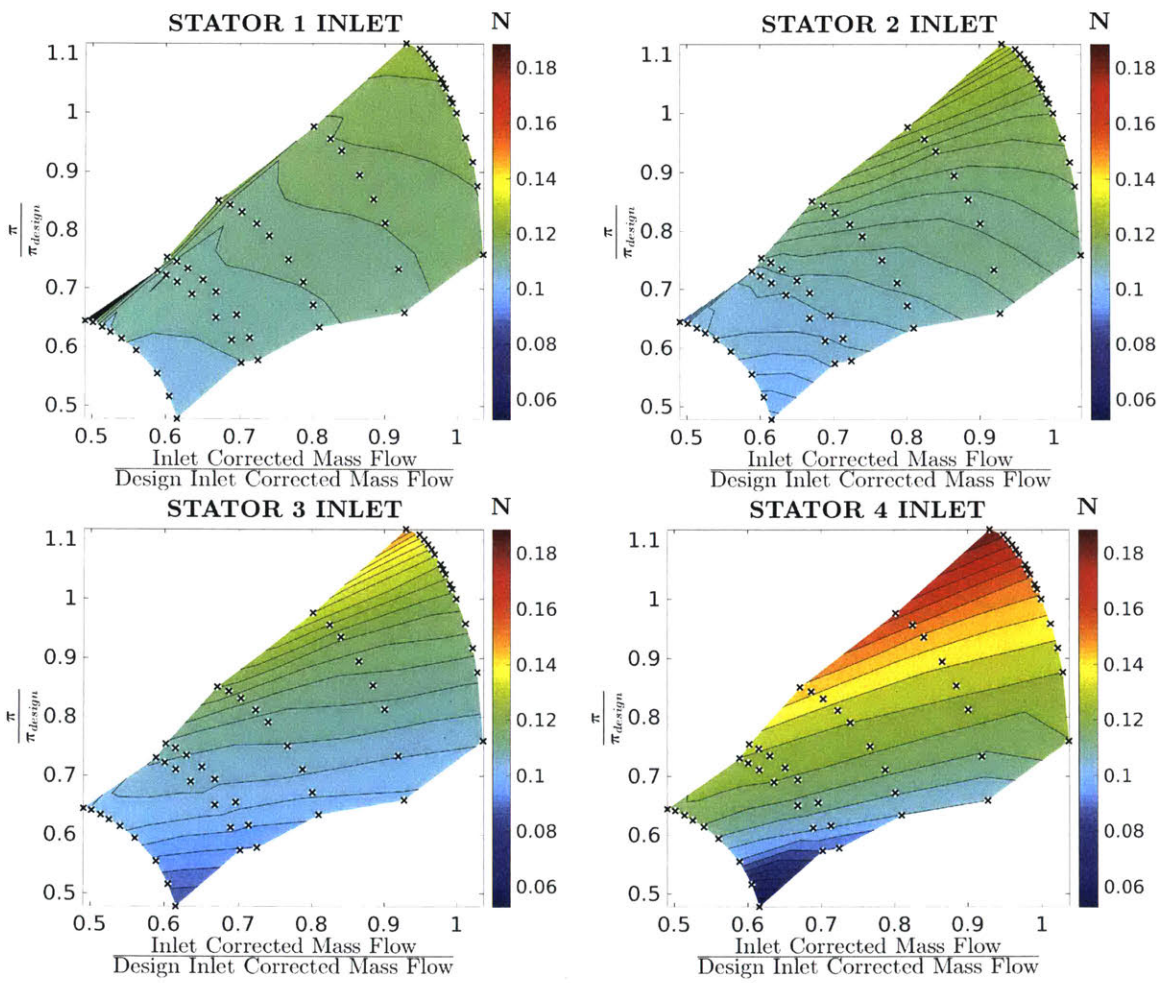

Figure 2-4: Level of flow non-uniformity increases through compressor.

Chapter 3

Representation of Radially Non-Uniform Flow Profiles

Radial flow profiles must be represented using a compact set of parameters to be incorporated into the NURM method. This is accomplished using a set of orthonormal basis functions based on weighted polynomials [17]. Combinations of the basis functions represent physical flow features such as endwall blockage and radial skew in mass flow. The radial non-uniformity at a station is characterized by the profiles of non-dimensional mass flow rate per unit span, which captures the non-uniformity in streamtube massflow and the associated impact on the radial work distribution, incidence, which captures non-uniformity in the velocity triangles across the span, and total temperature, which relates to the radial work distribution. Embedded stage CFD computations, representative of a typical stage in a full compressor, demonstrate this basis function representation method to be effective and suitable for use in the NURM method.

3.1 Basis Function Approach

Radial profiles can be represented by a linear combination of basis functions. The function space is spanned by the first five powers of the weighted polynomial g which is a function of the normalized radius $\hat{r}$:

$$g(\hat{r}) = \hat{r} - (\hat{r} - \frac{1}{2})\sqrt{\hat{r} - \hat{r}^2}, \quad \hat{r} = \frac{r - r_{min}}{r_{max} - r_{min}} \tag{3.1}$$

This formulation adds weight to the regions near the hub and shroud, allowing for the effective representation of flow features common to axial compressors which occur near the hub or shroud such as endwall boundary layers and tip leakage flow. The powers g^0, g^1, g^2, g^3, and g^4 provide a linearly independent set of functions which can be orthogonalized and normalized to produce a set of five orthonormal basis functions $\hat{f}_0$, $\hat{f}_1$, $\hat{f}_2$, $\hat{f}_3$, and $\hat{f}_4$. These span a function space which effectively approximates the space of non-uniform flow profiles in axial compressors. Projecting a radial flow profile onto this finite dimensional function space yields 5 coefficients denoted b_0, b_1, b_2, b_3, and b_4. The basis function representation f is then given by:

$$f = \sum_{i=0}^{4} b_i \hat{f}_i(\hat{r}) \tag{3.2}$$

3.1.1 Basis Function $\hat{f}_0$

$\hat{f}_0$ is constant across the span and its corresponding coefficient b_0 represents the arithmetic average of radial profiles $\frac{\rho V_x r - \overline{\rho V_x r}}{\overline{\rho V_x r}}$, $i - \bar{i}$, or $\frac{T_t - \overline{T}_t}{\overline{T}_t}$. $\hat{f}_0$ is the only basis function with a non-zero radial integral as a result of the orthogonalization. Basis function $\hat{f}_0$ is plotted in Figure 3-1.

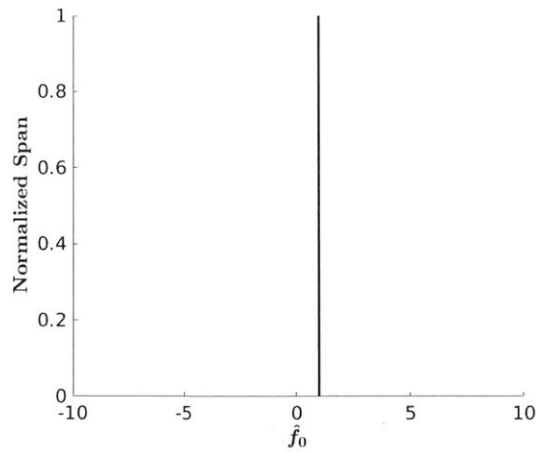

Figure 3-1: Basis function $\hat{f}_0$ is constant in span.

3.1.2 Basis Functions $\hat{f}_1$, $\hat{f}_2$, $\hat{f}_3$, and $\hat{f}_4$

Basis functions $\hat{f}_1$, $\hat{f}_2$, $\hat{f}_3$, and $\hat{f}_4$ each have zero radial integral and together represent the non-uniformity of the profile. Basis functions $\hat{f}_1$ and $\hat{f}_3$ are odd about mid-span. They capture the radial skewness of the profile. $\hat{f}_1$ represents radial skewness with higher flow near the shroud than the hub, while $\hat{f}_3$ represents radial skewness with higher flow near the hub than the shroud. $\hat{f}_3$ also demonstrates the impact of the weighted polynomials in its accentuated behavior near the endwalls. Basis functions $\hat{f}_2$ and $\hat{f}_4$ are even about mid-span and capture the endwall boundary layer profiles. $\hat{f}_2$ resembles a Poiseuille flow profile with thick, high shape factor boundary layers such as would be observed in a strong adverse pressure gradient. $\hat{f}_4$ shows the effect of the weighted polynomials with accentuated behavior near the endwalls. It is representative of thinner boundary layers such as would be produced in a flow with a weaker adverse pressure gradient. Basis functions $\hat{f}_1 - \hat{f}_4$ are shown in Figure 3-2.

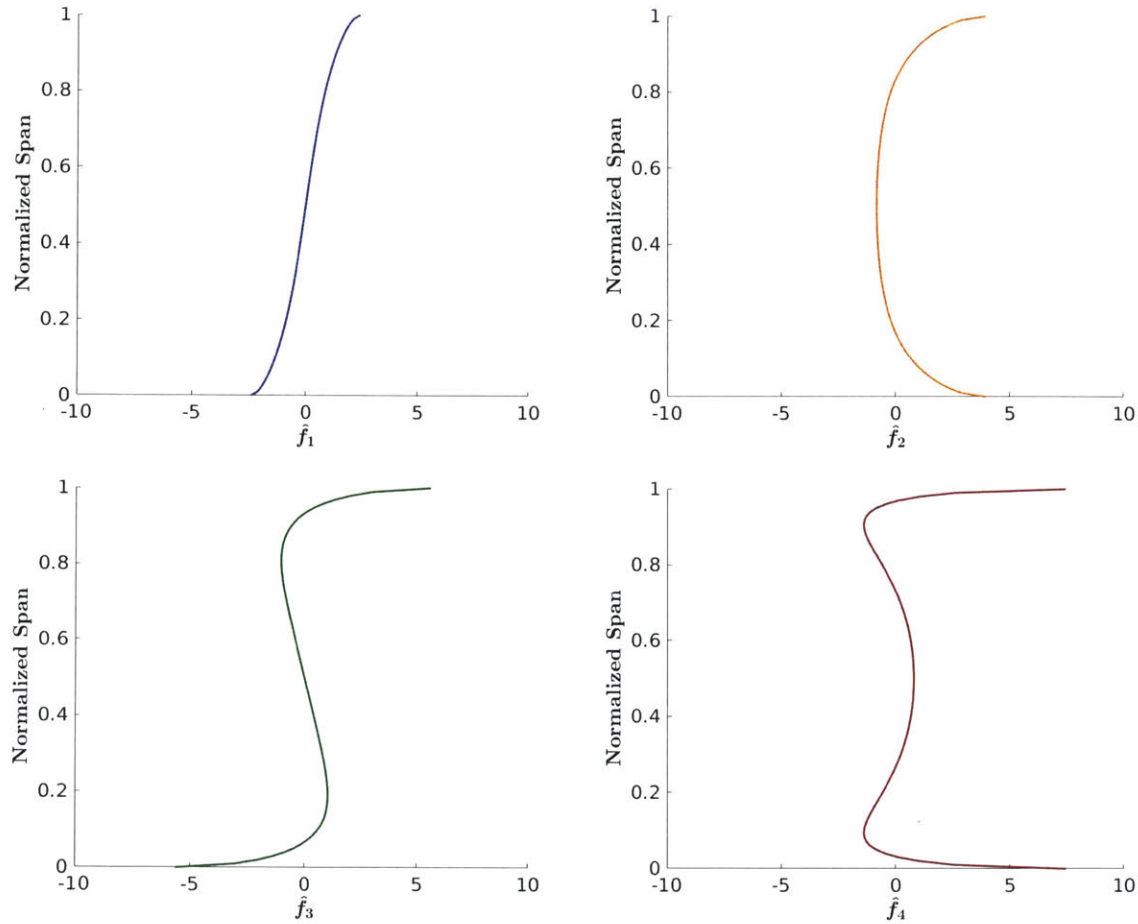

Figure 3-2: Odd basis functions $\hat{f}_1$ and $\hat{f}_3$ capture skew, even basis functions $\hat{f}_2$ and $\hat{f}_4$ capture blockage.

Figure 3-3 shows the build-up of the radial profile of mass flow rate per unit span for the design point at the rotor 3 inlet. The first basis function $\hat{f}_0$ sets the position along the abscissa. $\hat{f}_1$ adds radial skewness and $\hat{f}_2$ adds the general shape of the endwall blockage. $\hat{f}_3$ has little impact in this case because the true profile is radially skewed with higher flow near the shroud than the hub. $\hat{f}_4$ captures the details in the shape of the boundary layers and the curvature near mid-span. The final basis function representation approximates the true CFD profile in both overall non-uniformity and constituent non-uniformity components endwall blockage and radial skew in mass flow. Figure 3-4 shows that adding a sixth basis function does not impact the effectiveness of the representation. From Figure 3-3 it is clear that the fifth basis function is necessary to capture critical elements of the true radial profile

such as the endwall boundary layer profiles. This indicates that a five-term basis function representation provides a good balance between effectiveness and simplicity.

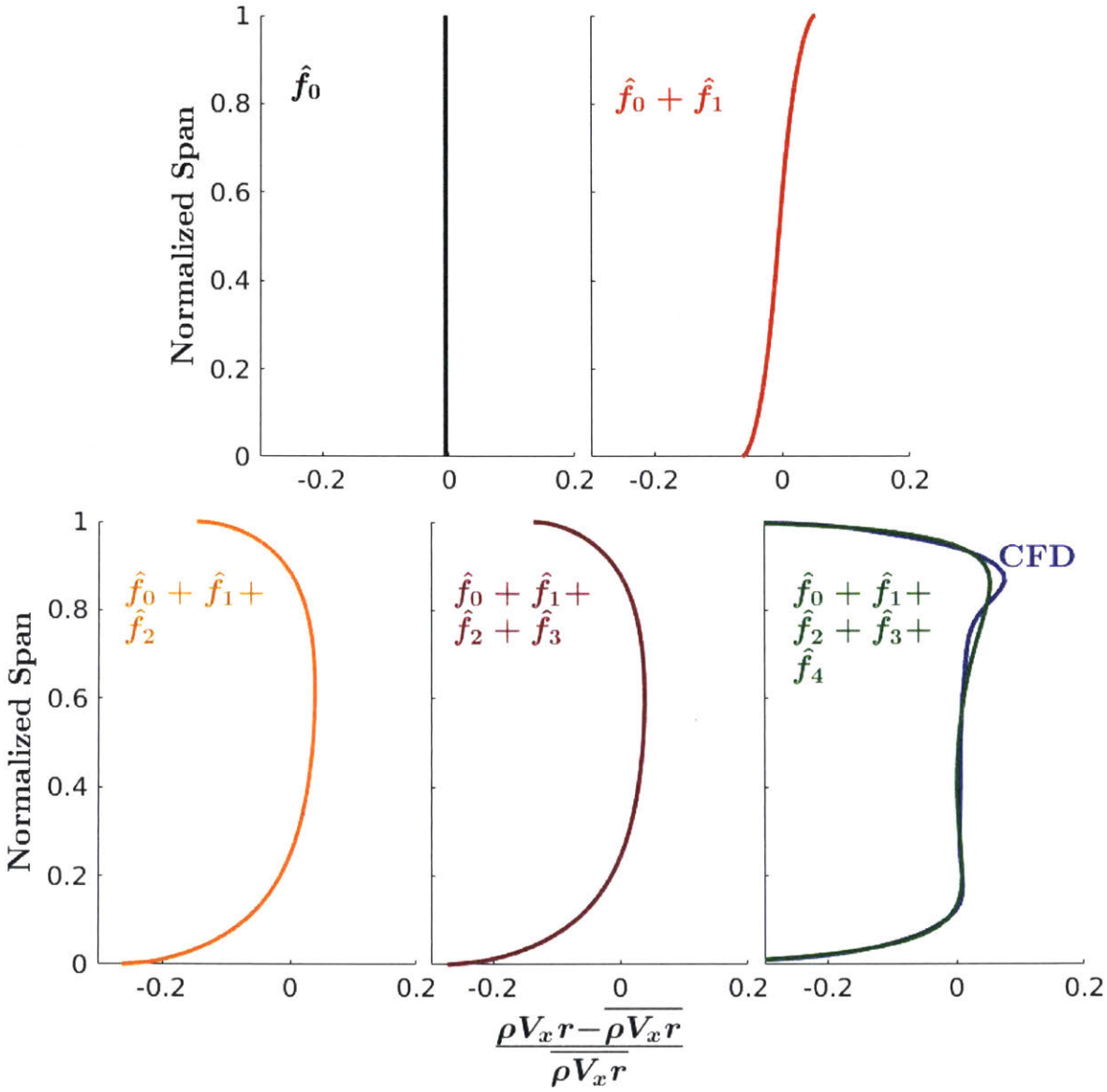

Figure 3-3: Each basis function contributes to overall representation of flow profile.

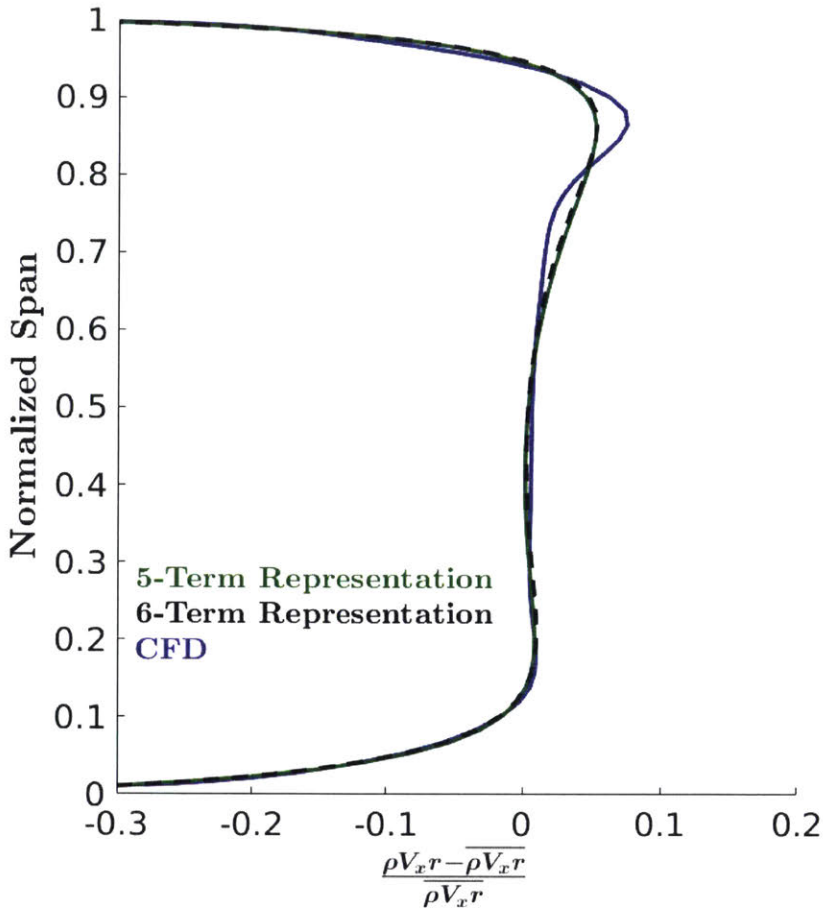

Figure 3-4: Adding sixth term to basis function representation does not alter representation effectiveness.

3.2 Evaluation of Flow Non-Uniformity Representation

The effectiveness of the basis function representation method was evaluated by using embedded stage CFD computations to assess the impact of the representation error on stage performance. The third stage of the test compressor was used as a representative embedded stage. The mesh representing the third stage in the multistage computations was extracted from the multistage mesh and used without modification to provide consistency between the embedded stage and multistage results. The rotor 3 inlet mixing plane from the multistage computations became the domain inlet

for the embedded stage computations. The short distance between the inlet where the boundary conditions were imposed and the rotor provided better control over the profiles at the rotor than would have been possible with a longer inlet duct. Upstream boundary conditions were imposed as radial profiles in axial velocity, tangential velocity, and static temperature. The outlet boundary condition was a static pressure boundary condition with radial equilibrium enforced. This computational setup gave the best control over the inlet $\rho V_x r$ profile and also had the benefit of setting the inlet Mach number and flow angle, giving direct control over the corrected flow per unit area. The computational domain is sketched in Figure 3-5.

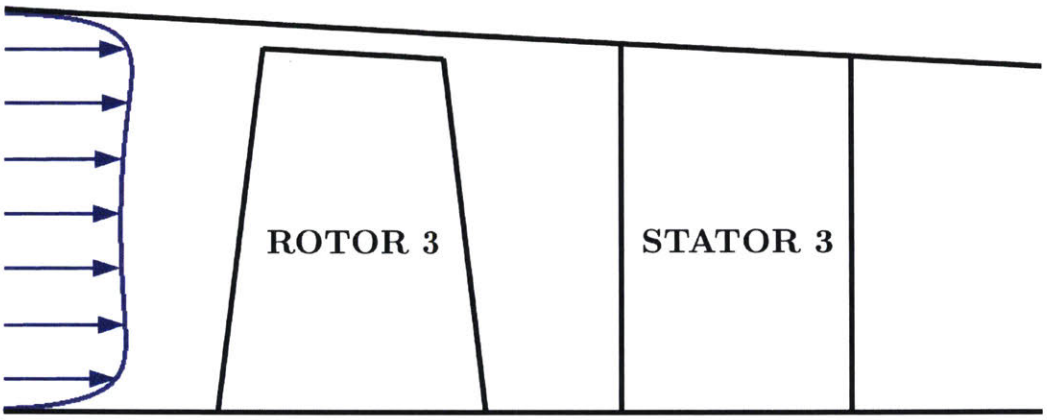

Figure 3-5: Embedded stage computational domain used in sensitivity study CFD computations. Upstream boundary conditions imposed as radial profiles. Shrouded stator cavities not modeled.

Datum computations were run with boundary condition profiles extracted directly from the rotor 3 inlet mixing plane in the corresponding multi-stage CFD computations. Test computations were then run with inlet boundary conditions calculated from basis function representations of the multi-stage CFD profiles. The inlet velocity and static temperature profiles used as boundary conditions were calculated from basis function representations of $\rho V_x r$, incidence, total pressure, and total temperature profiles. The results given in Table 3.1 show that the basis function representation effectively represents the true profiles found in multi-stage axial compressors because the basis function representations capture the stage performance, which is the ultimate goal of the performance estimation method. Stage efficiency error is less than

0.05% and rotor work coefficient error is less than 0.0025 at all three operating points tested across the 100% speed line.

	$\eta - \eta_{datum}$ [%]	$\psi - \psi_{datum}$
Choke	-0.01	-0.0018
Design Point	-0.04	-0.0017
Near Stall	-0.05	-0.0023

Table 3.1: Embedded stage CFD computations show basis function representation method effectively captures stage performance associated with radially non-uniform flow profiles. All computations run at 100%N.

The basis function representation method also effectively represents radial flow profiles of mass flow rate per unit span, incidence, and total temperature across the compressor operating map as shown in Figures 3-6, 3-7, and 3-8, respectively. Finally, the basis function method effectively represents radial flow profiles at all stations through the compressor including both rotors and stators as shown in Figure 3-9. Thus the basis function representation method is suitable for use in incorporating non-uniformity into the NURM method because it captures the non-uniformity at all necessary conditions and stations.

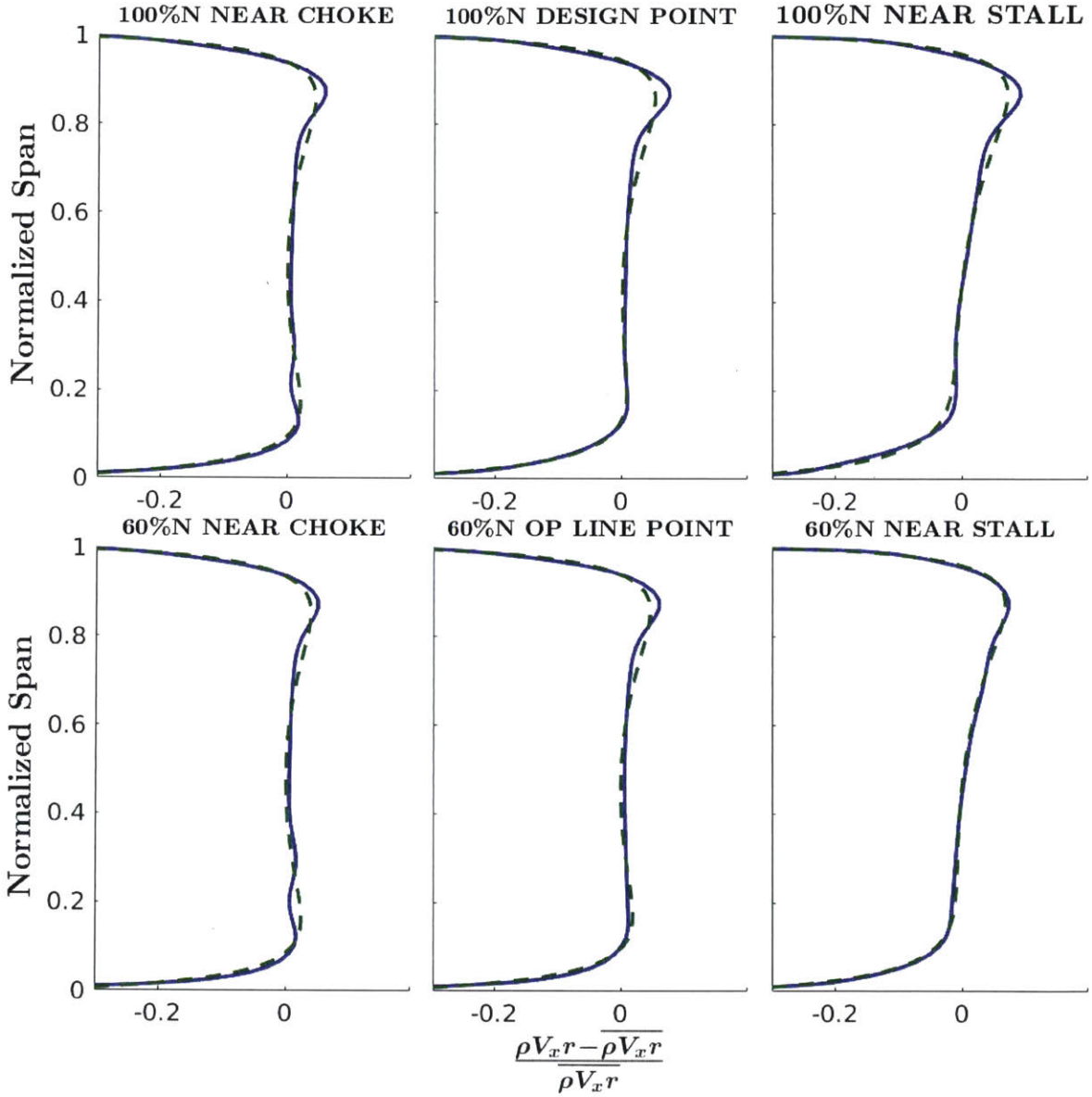

Figure 3-6: Basis function representation method effectively represents radial profiles of mass flow rate per unit span across compressor operating map. Rotor 3 inlet profiles shown. Dashed profiles are basis function representations of solid CFD profiles.

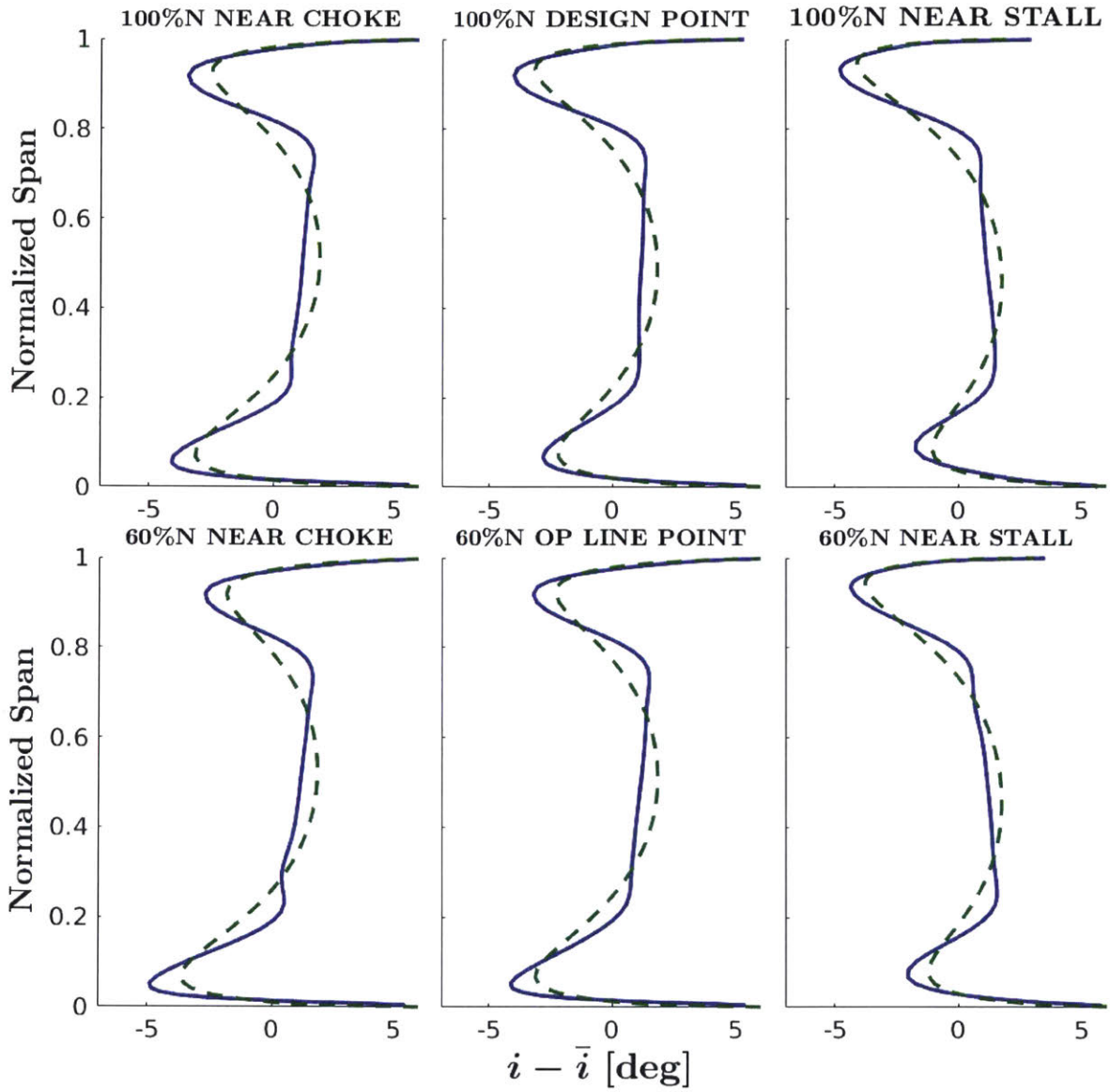

Figure 3-7: Basis function representation method also effectively represents radial profiles of incidence across compressor operating map. Rotor 3 inlet profiles shown. Dashed profiles are basis function representations of solid CFD profiles.

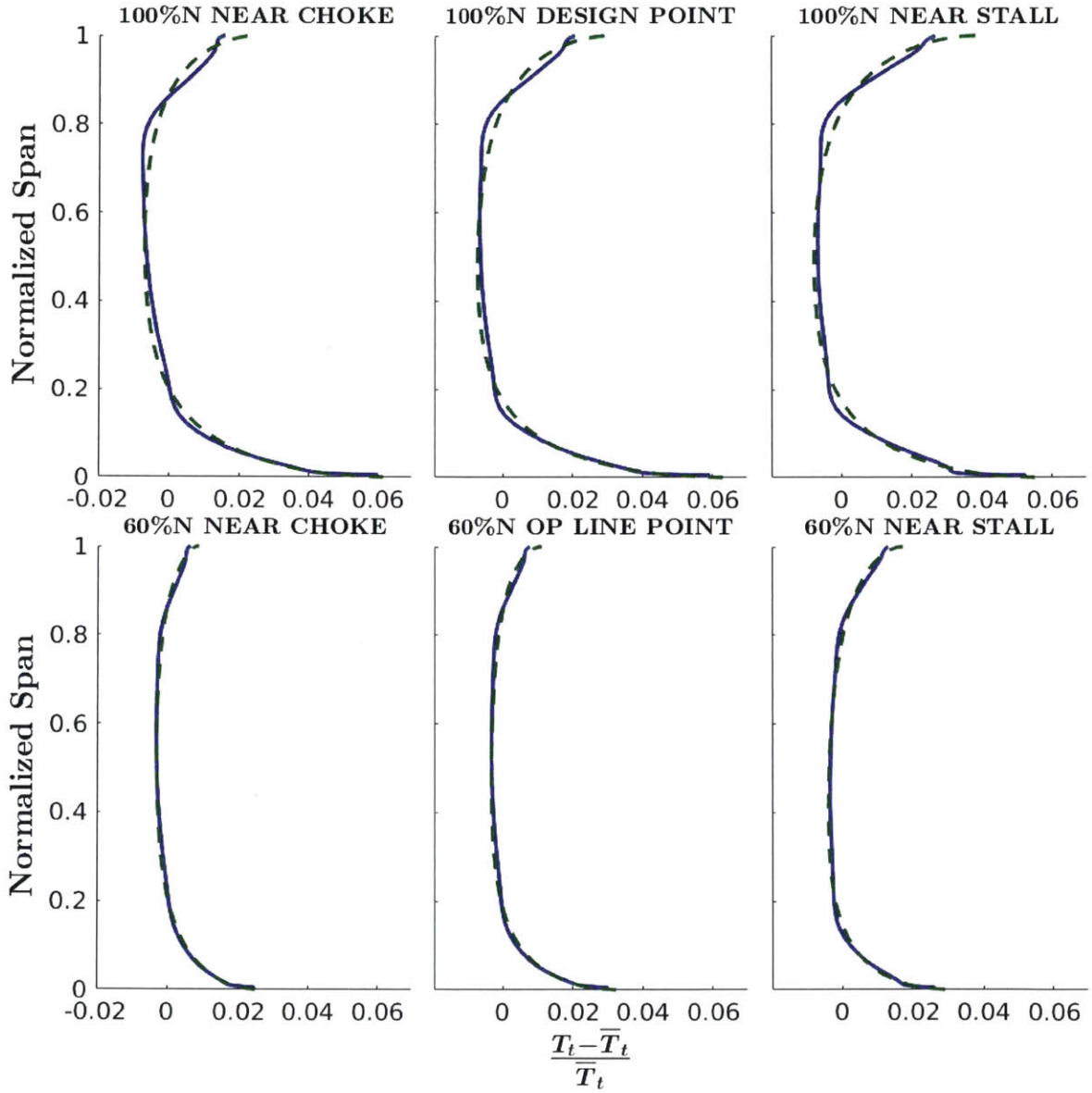

Figure 3-8: Basis function representation method effectively represents radial profiles of total temperature across compressor operating map. Rotor 3 inlet profiles shown. Dashed profiles are basis function representations of solid CFD profiles.

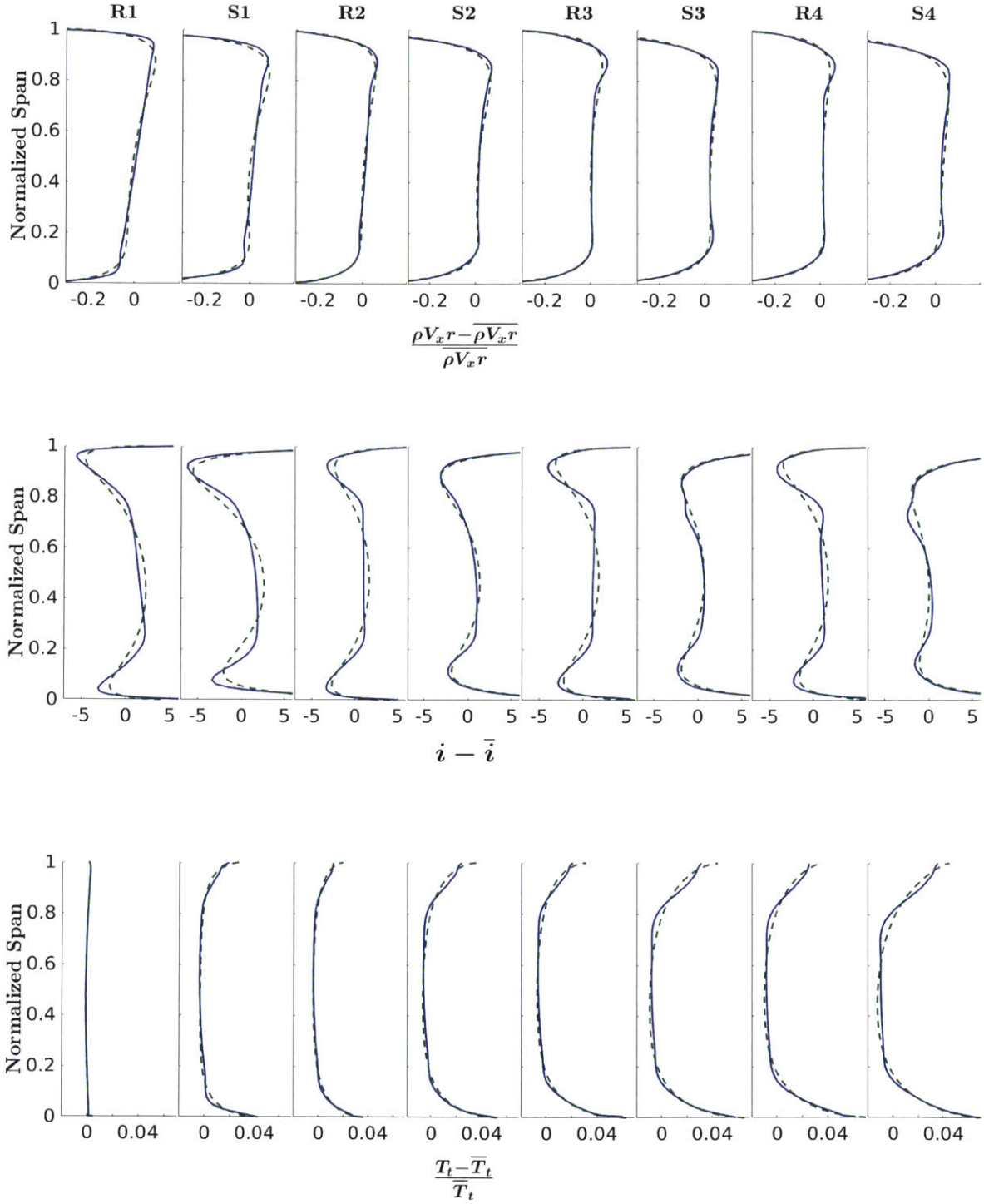

Figure 3-9: Basis function representation method is effective at all stations of test compressor. 100%N design point shown. Dashed profiles are basis function representations of solid CFD profiles.

3.3 Interpretation of Shape Parameters

Four shape parameters defined using the coefficients $b_1 - b_4$ characterize physical aspects of the flow profiles and represent non-uniformity in a compact set of parameters that are more physically meaningful than the basis function coefficients. The connection of the shape parameters to physical aspects of the flow profiles also facilitates the characterization of the link between non-uniformity and performance. Dependence of performance on non-uniformity can be assessed quantitatively by varying the shape parameters, and thus a physical aspect of the flow profiles, and measuring the impact on performance. This process and the resulting quantification of the link between non-uniformity and performance is detailed in Chapter 4.

3.3.1 Overall Non-Uniformity: Shape Parameter n

The overall non-uniformity of a profile is quantified using the root-mean square (RMS) of departures from the average value of the profile, as shown in Equation 3.3. This formulation is described in Chapter 2 as a means of capturing the overall non-uniformity of the mass flow rate per unit span profile in a scalar. It can be applied to the incidence and total temperature profiles to capture their non-uniformity as well.

$$\begin{aligned}
&\text{Mass Flow Rate Per Unit Span:} && \sqrt{\frac{1}{R_{max}-R_{min}}\int_{R_{min}}^{R_{max}}\left(\frac{\rho V_x r - \overline{\rho V_x r}}{\overline{\rho V_x r}}\right)^2 dr} \\
&\text{Incidence:} && \sqrt{\frac{1}{R_{max}-R_{min}}\int_{R_{min}}^{R_{max}}(i-\bar{i})^2 dr} \\
&\text{Total Temperature:} && \sqrt{\frac{1}{R_{max}-R_{min}}\int_{R_{min}}^{R_{max}}\left(\frac{T_t - \overline{T_t}}{\overline{T_t}}\right)^2 dr}
\end{aligned} \tag{3.3}$$

The RMS of a basis function representation profile is given by:

$$(RMS)_{basis\ function} = \sqrt{\int_0^1 \left(\sum_{i=0}^{4} b_i \hat{f}_i(\hat{r}) \right)^2 d\hat{r}} \tag{3.4}$$

Using the orthogonality of the basis functions and removing b_0 to eliminate the influence of the average value of the profile, the shape parameter n is defined as:

$$n = \sqrt{b_1^2 + b_2^2 + b_3^2 + b_4^2} \approx (RMS)_{basis\ function} \tag{3.5}$$

Figure 3-10 shows the impact of varying shape parameter n. Changing the RMS scales the difference from the average at each radial location, such that a profile with lower n such as the green profile is closer to 0 at all radii than the datum profile.

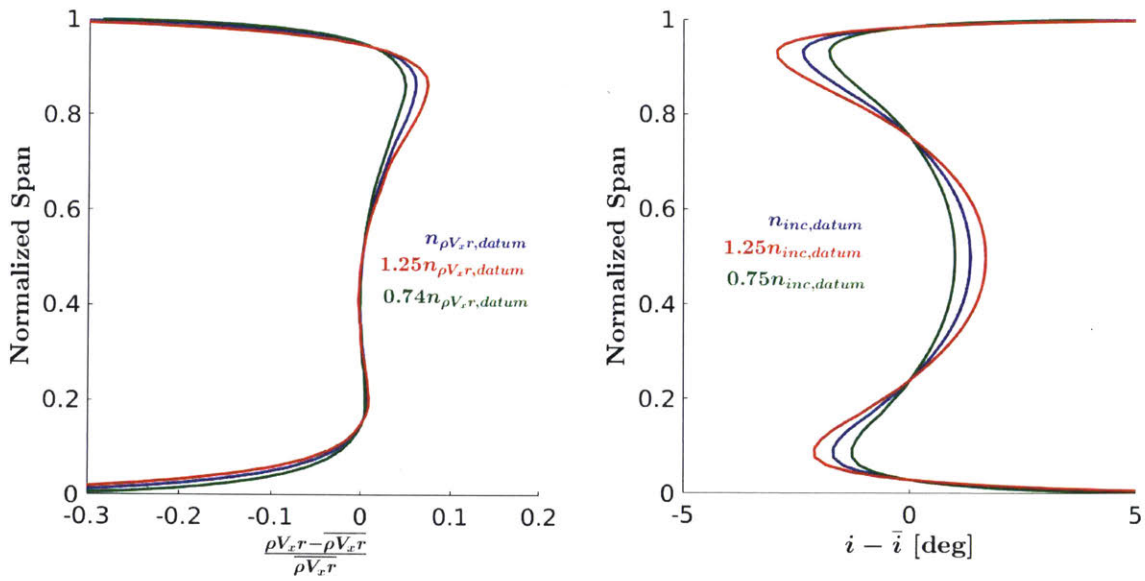

Figure 3-10: Variation in n at 100%N design point rotor 3 inlet.

3.3.2 Relative Importance of Radial Skew and Blockage: Shape Parameter θ_s

Shape parameter θ_s represents the ratio of the magnitudes of the coefficients of the odd basis functions to those of the even basis functions:

$$\theta_s = atan\left(\frac{\sqrt{b_1^2 + b_3^2}}{\sqrt{b_2^2 + b_4^2}}\right) \tag{3.6}$$

Profiles with larger coefficients of odd basis functions than even basis functions reflect radial skew. Figure 3-11 shows the impact of varying θ_s. The mass flow rate per unit span profile shows that a higher θ_s indicates a more radially skewed profile. The incidence profile is only weakly impacted by changes in θ_s because the profile is nearly entirely even; varying the relative strength of the odd coefficients has little impact on the profile.

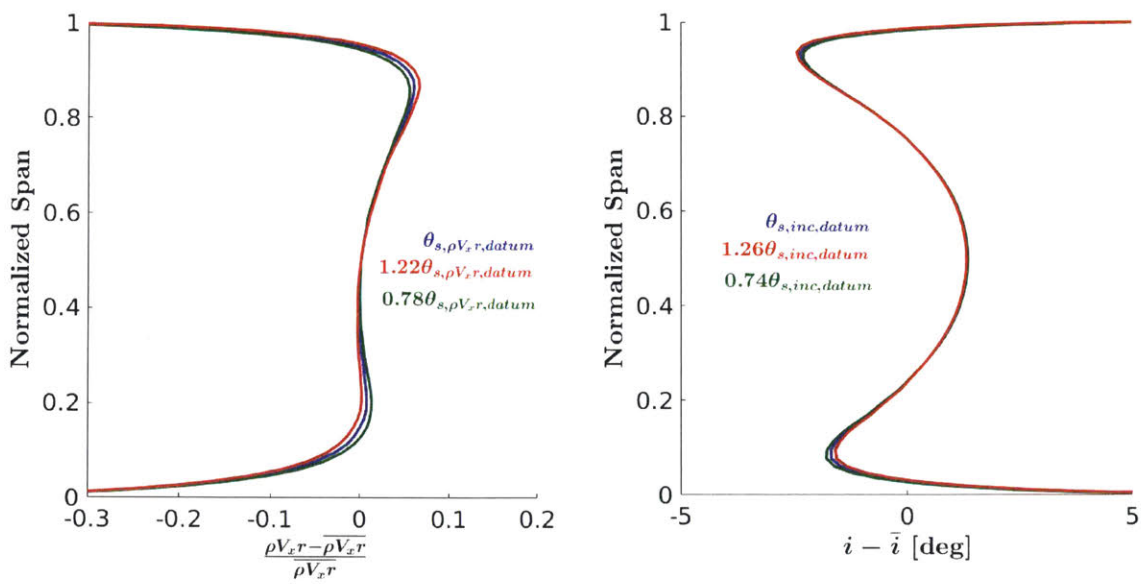

Figure 3-11: Variation in θ_s at 100%N design point rotor 3 inlet.

3.3.3 Shape of Radial Skewness: Shape Parameter θ_o

Shape parameter θ_o represents the ratio of the two odd basis functions:

$$\theta_o = atan2(b_1, b_3) \tag{3.7}$$

Where $atan2$ is defined as:

$$atan2(x,y) = \begin{cases} atan(\frac{y}{x}) & \text{for x} > 0 \\ atan(\frac{y}{x}) + \pi sign(y) & \text{for x} < 0 \\ sign(y) & \text{for x} = 0 \\ Undefined & \text{for x} = \text{y} = 0 \end{cases} \tag{3.8}$$

Figure 3-12 shows the impact of varying θ_o. The mass flow rate per unit span profiles show stronger influence of $\hat{f}_1$ moving from green to red with increasing θ_o. This results in radial skewness with higher flow near the shroud than the hub. Again, the incidence profile is only weakly affected because the datum profile is almost entirely even so the odd basis functions do not play a significant role in determining the shape of the profile.

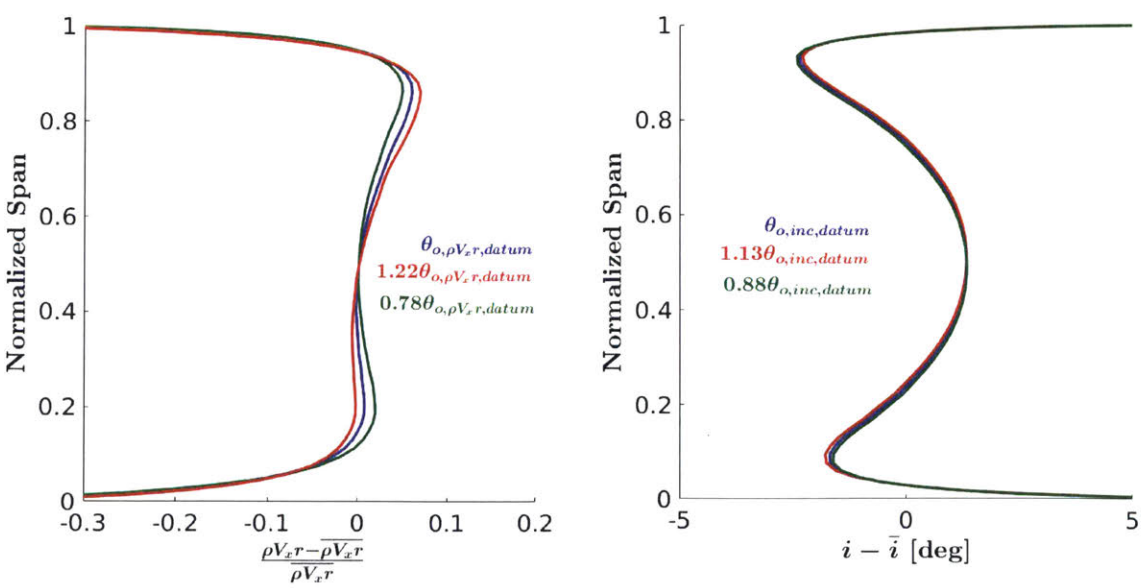

Figure 3-12: Variation in θ_o at 100%N design point rotor 3 inlet.

3.3.4 Shape of Boundary Layer Profiles: Shape Parameter θ_e

Shape parameter θ_e represents the ratio of the two even basis functions:

$$\theta_e = atan2(b_2, b_4) \tag{3.9}$$

Figure 3-13 shows the impact of varying θ_e. The mass flow rate per unit span profiles show the impact on the boundary layer profiles of varying the relative strengths of $\hat{f}_2$ and $\hat{f}_4$. The red profile shows the thinner boundary layers associated with a strong $\hat{f}_4$ while the green profile is closer to the Poiseuille flow-like shape of $\hat{f}_2$. Once again, the incidence profile is not significantly affected by variations in θ_e because the profile is dominated by $\hat{f}_4$.

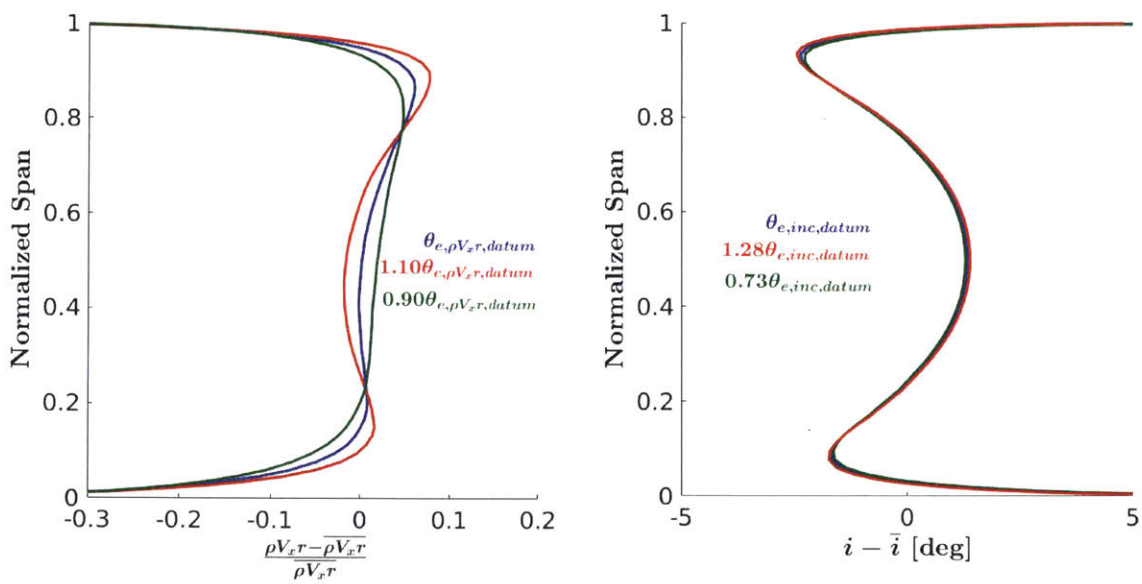

Figure 3-13: Variation in θ_e at 100%N design point.

3.4 Conclusions

It was demonstrated that radial flow profiles typical in axial flow compressors can be represented in a compact set of parameters suitable for incorporation into the NURM method through the use of orthonormal basis functions. The basis functions are derived from weighted polynomials which emphasize the endwall regions to facilitate effective representation of the profiles found in multi-stage axial compressors. This single set of basis functions is suitable for all relevant flow quantities ($\rho V_x r$, incidence,

and total temperature) at all operating points and all stations in the compressor. Embedded stage CFD computations confirm the effectiveness of the representation method. Shape parameters defined as combinations of the basis functions characterize physical flow features present in the radial profiles such as endwall blockage and radial skew in mass flow and provide a means of quantitatively assessing the link between non-uniformity and performance.

Chapter 4

Characterization of Link Between Non-Uniformity and Performance

The basis function representation method described in Chapter 3 enables the incorporation of radially non-uniform flow profiles into a 1D performance estimation method. In order to make use of those profiles in performance estimation, the link between non-uniformity and performance must be quantitatively characterized in a manner suitable for incorporation into the NURM method. This method characterizes blade row performance using stagnation pressure loss coefficient, deviation angle, and blockage. The link between non-uniformity and performance is characterized using the influence of non-uniformity on the same performance parameters. The results of the characterization are also used to determine which shape parameters are most important and which are negligible so that negligible shape parameters can be omitted to simplify the method. The key outcomes are:

- Impact of non-uniformity on performance is characterized quantitatively in a manner suitable for incorporation into the NURM method
- Changes in $\rho V_x r$ and incidence non-uniformity cause changes on order of 1% in blade row performance, are important to be captured in NURM method
- Changes in total temperature non-uniformity cause changes on order of 0.1%

in blade row performance, are negligible compared to effects of changes in $\rho V_x r$ and incidence non-uniformity

- Dependence on operating point of impact of non-uniformity on performance captured in NURM method using sensitivity study data from multiple operating points

4.1 Sensitivity Study

The partial derivatives of loss coefficient, deviation angle, and blockage factor with respect to each shape parameter of the $\rho V_x r$, incidence and total temperature profiles were determined using embedded stage CFD computations with variations in the stage inlet shape parameters. These variations cause changes in the radial profiles at the stage inlet, which in turn cause changes in the stage performance. Figure 4-1 shows examples of variations in inlet conditions resulting from variations in shape parameters. Each shape parameter was varied by roughly $\pm 25\%$. This variation is representative of the variation seen across the test compressor operating map, provides sufficient variation in radial profiles to induce a response in blade row performance, and is small enough to remain within the effective range for linear partial derivatives. While the radial profiles were varied the mass average Mach number and flow angle, and thus the stage operating point, were held constant to ascertain the impact of variations in non-uniformity alone. This procedure was repeated at six operating points across the compressor operating map to capture the variation in sensitivity across the map. These points are marked in Figure 4-2 on the datum map of the test compressor.

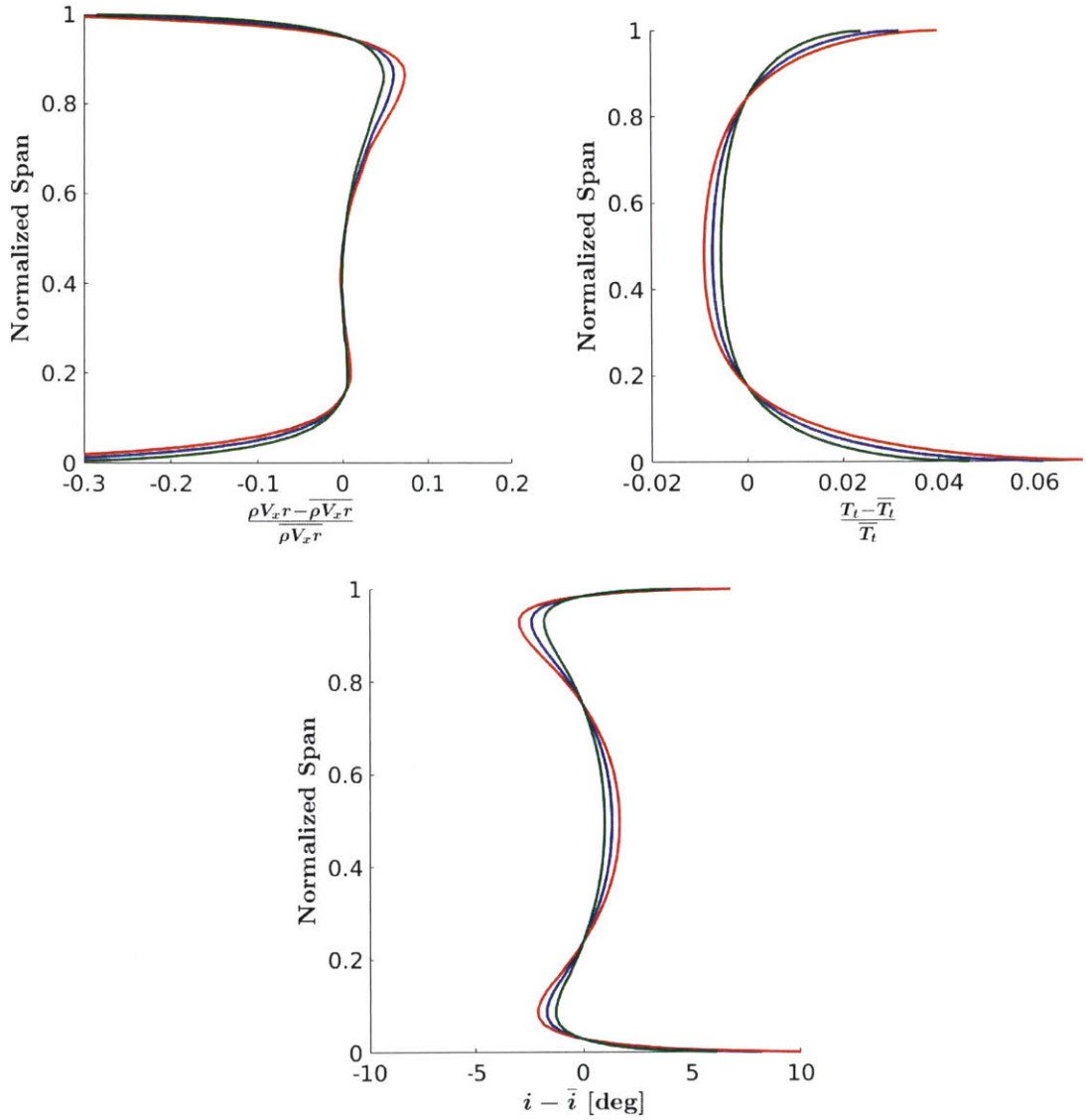

Figure 4-1: Variations in shape parameter n produce variations in flow profiles of $\rho V_x r$, total temperature, and incidence. Profiles shown at rotor 3 inlet, design point.

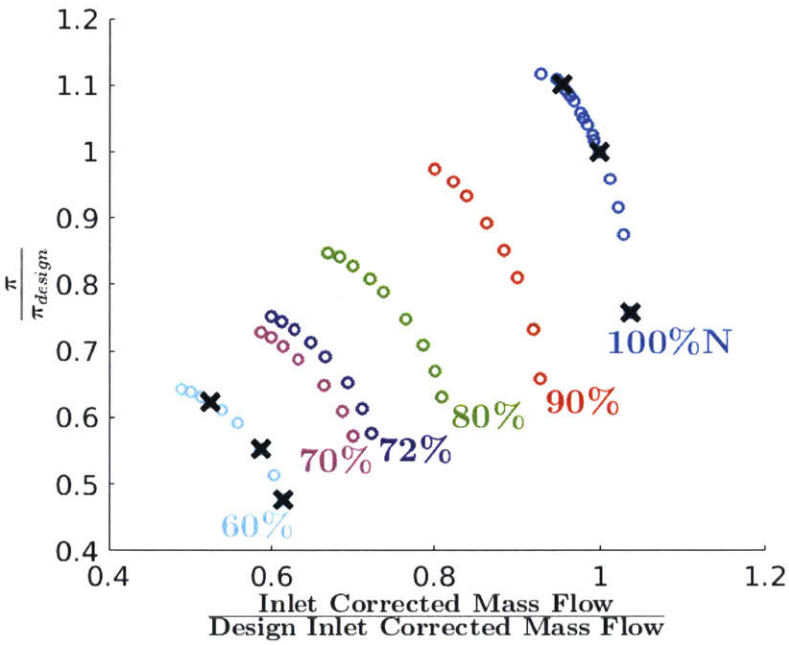

Figure 4-2: Sensitivity study conducted at six operating points spanning map to capture variation across map in impact of inlet flow non-uniformity on blade row performance.

4.1.1 Embedded Stage Computation Configuration

The embedded stage computations utilized the third stage of the test compressor in isolation. The flow in this stage is fully developed and representative of the flow in an embedded stage of a full compressor of a gas turbine. In this preliminary implementation of the NURM method, the sensitivities obtained from this data were used for all stages. In the final implementation of the method, sensitivity data should be obtained for each stage.

The computational domain was the same as described in Section 3.2. The inlet boundary conditions were imposed as radial profiles of axial velocity, tangential velocity, and static temperature upstream of the rotor. A static pressure was specified as the outlet boundary condition downstream of the stator with radial equilibrium enforced. Basis function representations of $\rho V_x r$, P_t, T_t, and incidence were used to calculate the necessary inlet boundary condition profiles.

4.2 Sensitivity Results

The results of this study represent the first quantitative characterization of the impact of overall radial flow non-uniformity, or "maldistribution" [6], on compressor blade row performance. Figure 4-3 shows the impact of changes in $n_{\rho V_x r}$ on loss coefficient, deviation, and blockage at the 100% speed near stall point. This point is useful in examining the underlying mechanisms because it exhibits the largest performance changes. Deviation and blockage increase as expected with increasing maldistribution, while loss coefficient decreases. The magnitudes of the changes shown are on the order of 10%. This indicates that non-uniformity has a significant impact on performance which merits incorporation into the estimation of off-design performance.

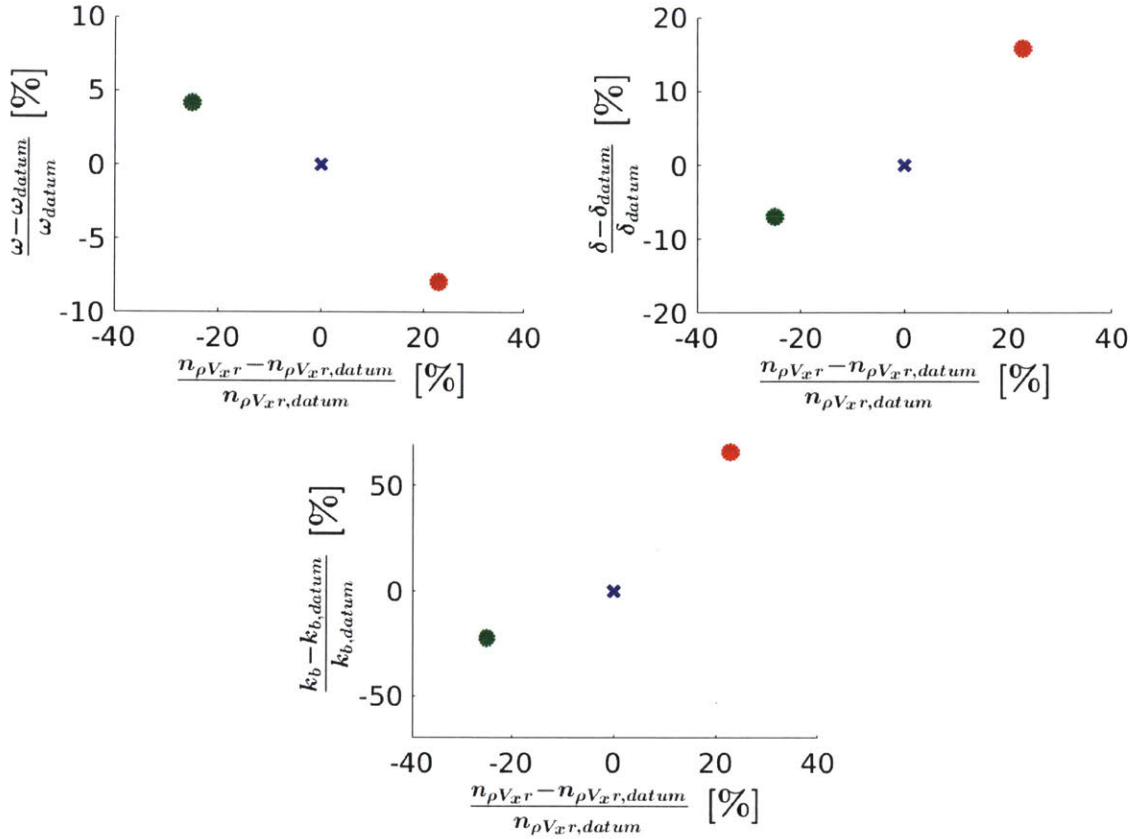

Figure 4-3: Non-uniformity appreciably impacts blade row performance. 100% speed near stall point shown.

The causes underlying these trends are best understood through an examination of the changes in inlet flow. Figure 4-4 shows the baseline and perturbed inlet $\rho V_x r$ profiles. The vertical dashed line marks the average $\rho V_x r$. The overall non-uniformity reflects the difference from average at each radius. Accordingly, the flow can be split into three regions. Below 49% span and above 96% span the baseline profile is less than average, meaning that an increase in non-uniformity results in reduced mass flow. Between 49 and 96% span the baseline mass flow rate is above average, so an increase in non-uniformity corresponds to an increase in mass flow. Distinct mechanisms govern the performance changes in each of these regions. Hub corner separation, tip leakage flow, and blade loading govern the trends near the hub, near the tip and in the midspan region, respectively. For example, the same three regions appear in the radial profiles of relative total pressure loss across the stage, as shown in Figure 4-5.

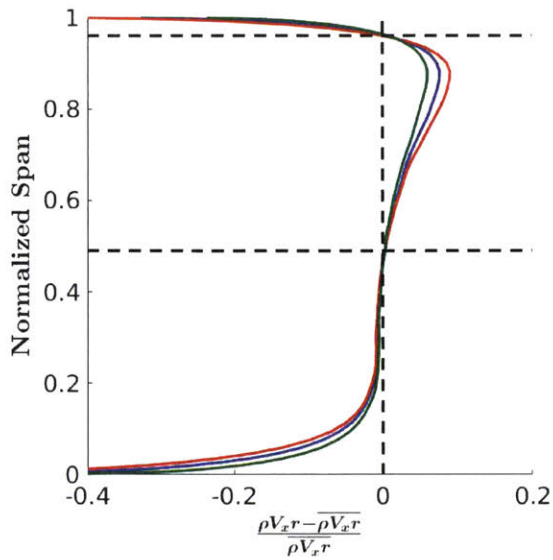

Figure 4-4: Changing inlet non-uniformity scales difference from average at each radius. Rotor inlet profiles shown.

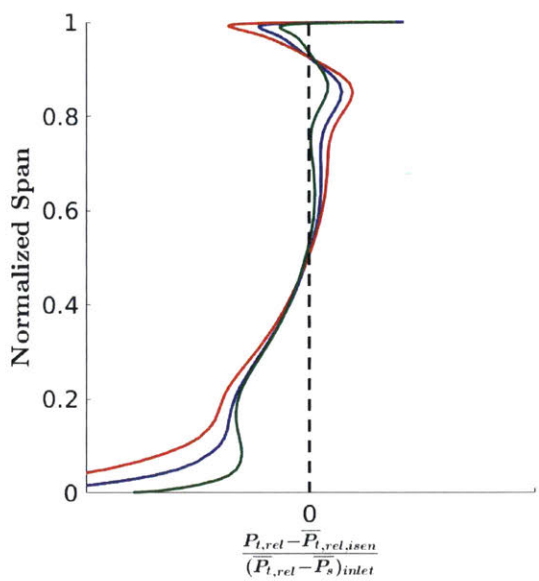

Figure 4-5: Trends in relative total pressure loss correspond to trends in mass flow. Rotor outlet profiles shown.

Near the hub, the flow mechanism governing changes in performance with changes in inlet flow non-uniformity is hub corner separation. As non-uniformity increases, the mass flow is decreased near the hub. This reduction in momentum degrades the ability

of the flow to navigate the adverse pressure gradient across the blade, increasing the severity of the hub corner separation relative to the baseline case. Figure 4-6 shows the progression of increasing separation with increasing non-uniformity. This increase in separation is the cause of the increased loss in the hub region, and the increase in blade row deviation. The rotor outlet radial relative flow angle profiles plotted in Figure 4-7 only show changes in the region corresponding to the hub corner separation. The hub corner separation is also the primary cause of the blockage increase, as shown in the outlet $\rho V_x r$ profiles in Figure 4-8. These trends near the hub are expected to apply to compressors of similar geometry to the test compressor, but they may not be generally applicable to other compressors which may not develop hub corner separation. The characterization of compressors of widely different geometries would require additional sensitivity studies.

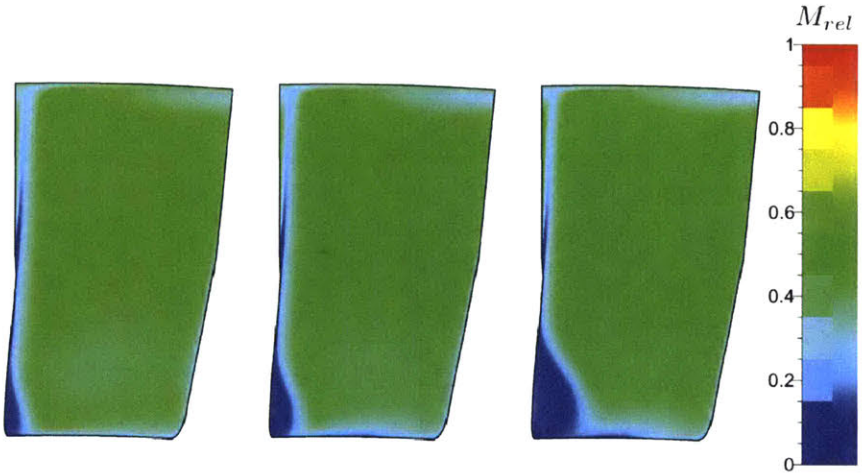

Figure 4-6: Increase in non-uniformity exacerbates hub corner separation, increasing loss near hub. Rotor trailing edge shown, non-uniformity increasing from left to right.

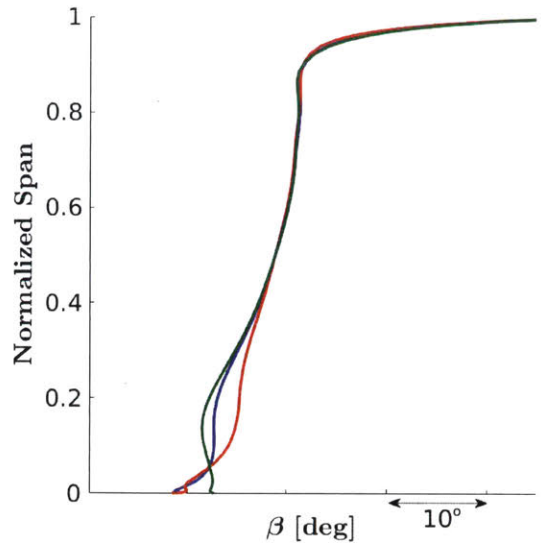

Figure 4-7: Increase in deviation caused by increase in hub corner separation. Rotor outlet profiles shown.

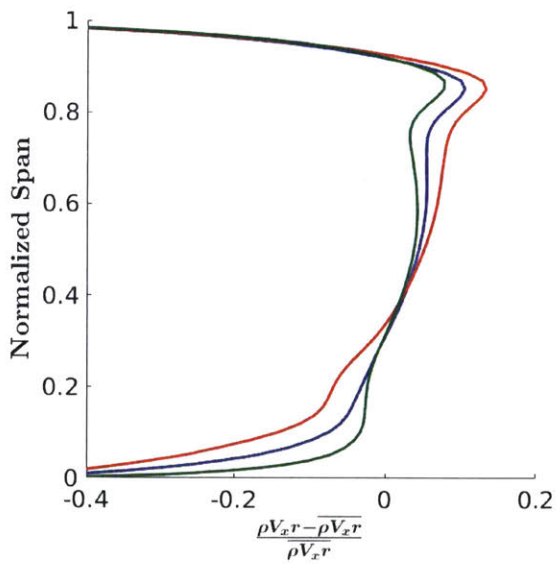

Figure 4-8: Increase in blockage primarily caused by increase in hub corner separation. Rotor outlet profiles shown.

Near the shroud, the tip leakage flow is the governing mechanism. Increased non-uniformity corresponds to decreased mass flow rate per unit span in this region, and the reduced incoming momentum leads to a stronger tip vortex, as shown in Figure

4-9. The exacerbation in tip leakage effects increases the loss in the tip region.

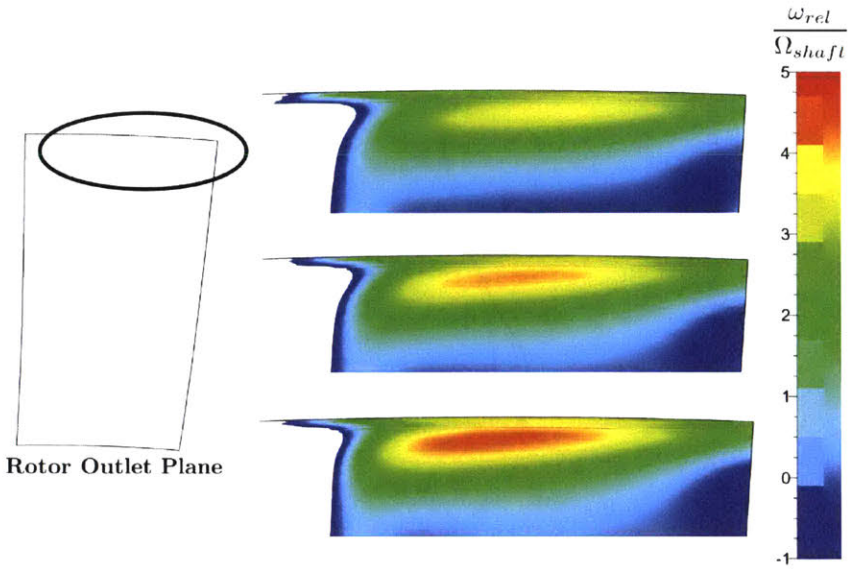

Figure 4-9: Vorticity contours show increase in non-uniformity exacerbates tip leakage effects. Non-uniformity increasing from top to bottom.

In the 49-96% span region the increase in non-uniformity corresponds to an increase in mass flow per unit span. However, the inlet incidence is unchanged and aside from the change in deviation near the hub, the outlet flow angle is also unchanged, so the increase in flow with the same change in relative flow angle results in a reduction in the change in absolute flow angle across the stage, as shown in Figure 4-10. This corresponds to a reduction in the blade loading. The majority of the boundary layer growth on the airfoil surface occurs as a result of the diffusion which must take place on the aft portion of the blade after the flow has been accelerated [18]. This boundary layer is shed at the trailing edge to become the airfoil wake, and the mixing out of the wake is the source of the associated loss [7]. Lower loading leads to less diffusion and hence thinner boundary layers, thinner wakes, and less profile loss. This effect, in conjunction with the high mass flow per unit span in this radial region, is the cause of the overall reduction in mass-average rotor loss brought about by increased inlet flow non-uniformity. Figure 4-10 shows reduced flow turning near the hub as well, but this is a result of the increased deviation shown in Figure 4-7.

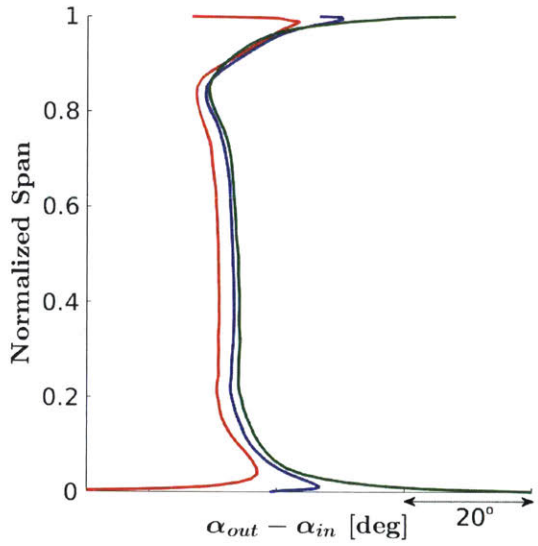

Figure 4-10: Increase in non-uniformity reduces blade loading.

In addition to the overall non-uniformity magnitude, the basis function representation method captures the shape of the radial flow profiles through the other shape parameters. Two perturbed cases were run for each shape parameter at each operating point, and Figures 4-11 - 4-13 show the results for variations in all inlet shape parameters of the $\rho V_x r$, incidence, and total temperature profiles at the design point and the 60% speed op line point. The results show that in addition to the overall non-uniformity, the shape of the profile has a significant impact on performance. This indicates that all shape parameters must be included in the NURM method to capture the full impact of radial non-uniformity on blade row performance. The changes in performance produced by changes in total temperature non-uniformity are consistently an order of magnitude or more smaller than those resulting from changes in $\rho V_x r$ and incidence non-uniformity.

The changes in blade row outlet blockage factor with $\rho V_x r$ non-uniformity are on the order of 10% in several cases. This large change in blockage will have a major impact on the stage matching as the variation in corrected flow is amplified across downstream stages. This characterization of those effects facilitates their inclusion in the NURM method.

The changes in performance resulting from changes in inlet flow non-uniformity differ between the two operating points, which confirms that the impact of inlet flow non-uniformity on blade row performance is a function of operating point.

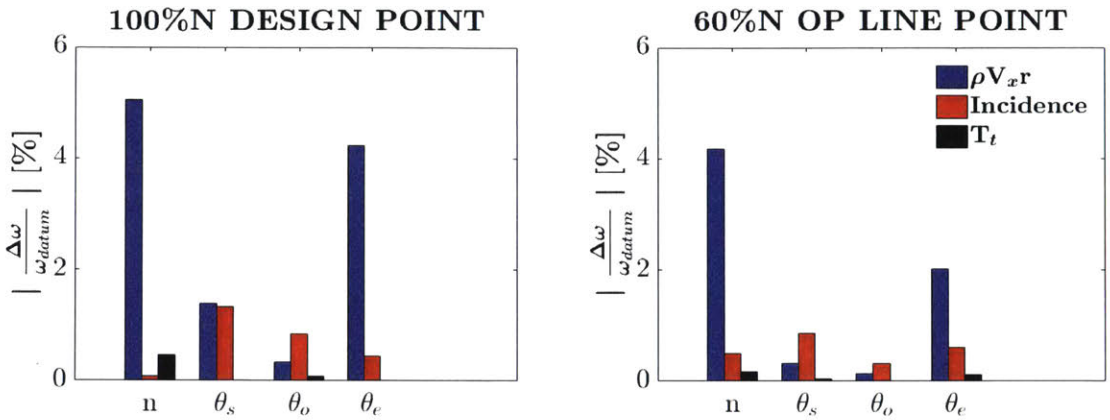

Figure 4-11: Impact of changes in total temperature non-uniformity on rotor loss coefficient are negligible, those of changes in $\rho V_x r$ and incidence non-uniformity are appreciable.

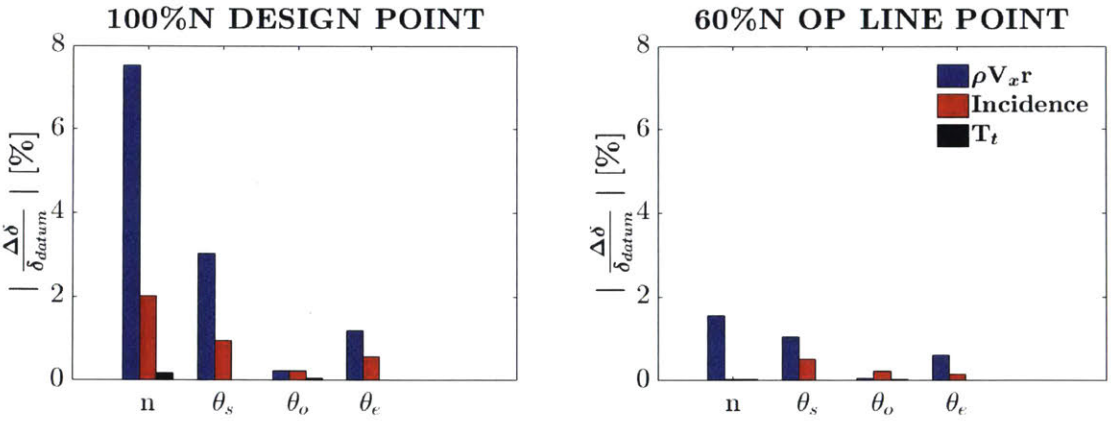

Figure 4-12: Impact of changes in total temperature non-uniformity on rotor deviation are negligible, those of changes in $\rho V_x r$ and incidence non-uniformity are appreciable.

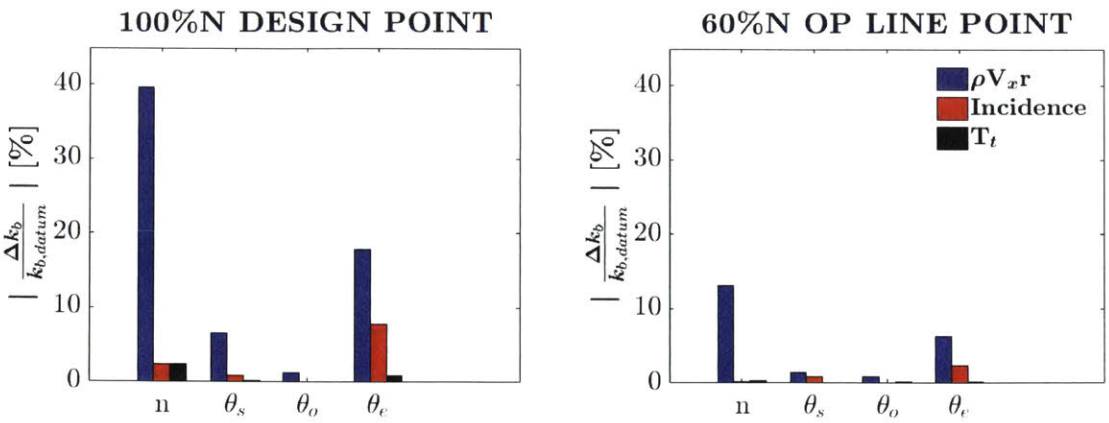

Figure 4-13: Changes in blade row inlet non-uniformity impact blade row outlet blockage materially, by up to 40%. As above, effects of changes in total temperature non-uniformity are negligible, those of changes in $\rho V_x r$ and incidence non-uniformity are appreciable.

Table 4.1 concatenates the average performance changes in terms of percentages of the datum performance at each respective operating point. The average changes in performance resulting from changes to mass flow and incidence non-uniformity are on the order of 1%. This confirms the conclusion that changes to $\rho V_x r$ and incidence non-uniformity elicit appreciable changes in performance. Changes in total temperature non-uniformity have a negligible impact on performance relative to the other parameters.

Average Performance Change	$\rho V_x r$	Incidence	Total Temperature
$\lvert\Delta\omega\rvert$[%]	2.71	1.25	0.143
$\lvert\Delta\delta\rvert$ [%]	2.91	1.15	0.137
$\lvert\Delta k_b\rvert$ [%]	12.7	2.62	0.723

Table 4.1: Performance changes induced by changes in T_t non-uniformity negligible relative to changes induced by $\rho V_x r$ and incidence non-uniformity.

Finally, as expected the impact of non-uniformity on performance varies across the compressor operating map, and the data from these six operating points permits

the incorporation of this variation into the NURM method. Figures 4-14 - 4-16 show contours across the operating map of the sensitivity of loss, deviation, and blockage to radial inlet flow non-uniformity. The sensitivity of stagnation pressure loss coefficient is found to be highest near stall and lowest along the operating line. This is consistent with the steeper slope of the loss bucket away from the design point, which means that the blade is more sensitive to changes at operating points away from the design point. The sensitivity of deviation angle is found to be highest near stall and lowest near choke. This is consistent with the above finding that deviation is primarily influenced by hub corner separation, which is more sensitive to changes in inlet flow in the presence of stronger adverse pressure gradients. In addition, the trend in deviation is consistent with the higher blade loading near stall and lower loading near choke. In general, apart from effects such as hub-corner separation, deviation is largely an inviscid effect brought about by the necessity to unload the flow at the trailing edge. In a more highly loaded state the blade must unload more over the same chord length, and this can result in higher deviation. The more highly loaded conditions near stall should result in greater sensitivity of deviation to non-uniformity. The sensitivity of blockage is highest near stall and lowest near choke. This is consistent with the stronger adverse pressure gradients near stall which result in thicker endwall boundary layers.

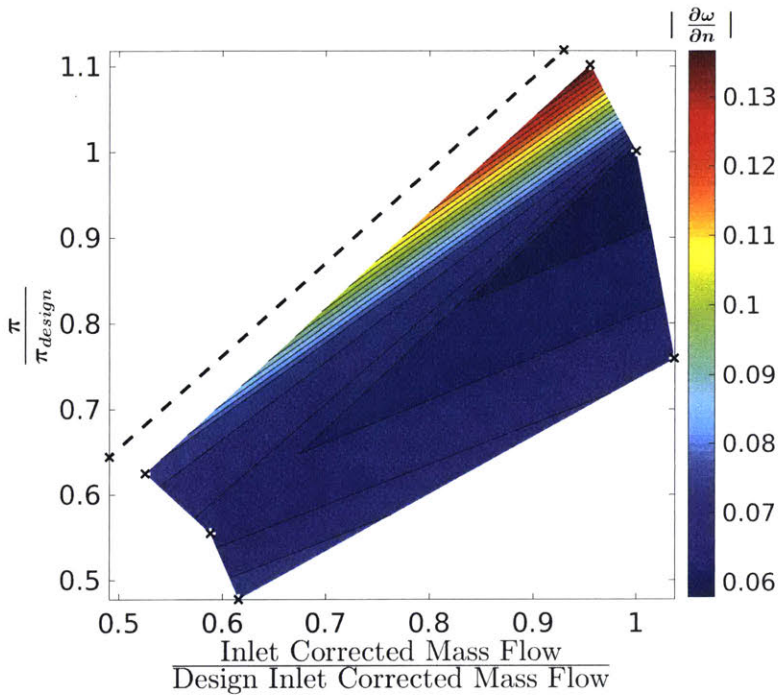

Figure 4-14: Sensitivity of loss coefficient to changes in $\rho V_x r$ non-uniformity varies across operating map.

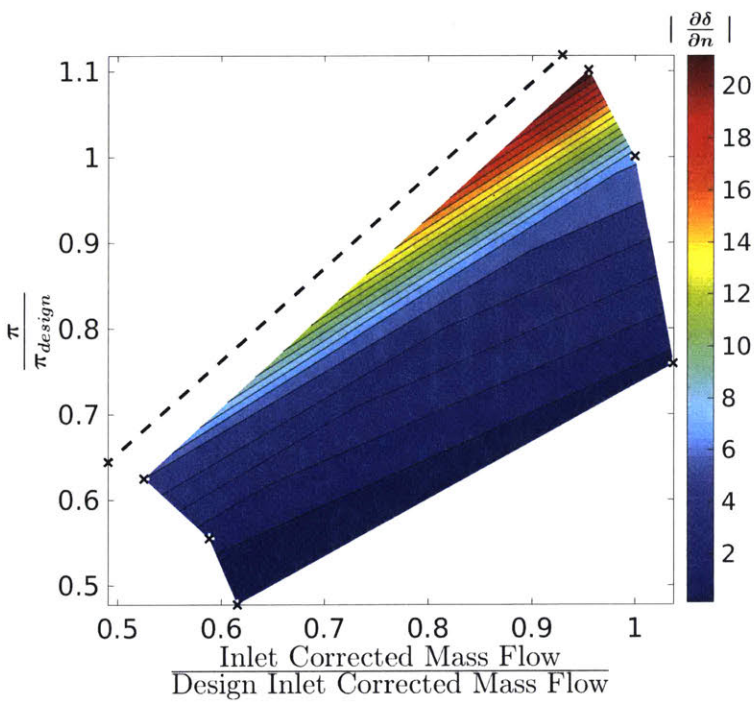

Figure 4-15: Sensitivity of deviation angle to changes in $\rho V_x r$ non-uniformity varies across operating map.

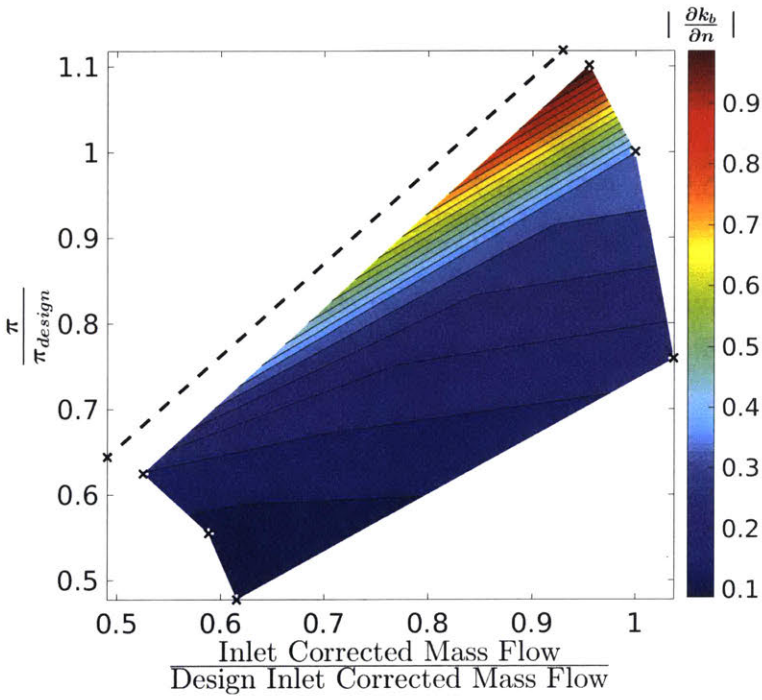

Figure 4-16: Sensitivity of blade row outlet blockage to changes in blade row inlet $\rho V_x r$ non-uniformity varies across operating map.

4.3 Non-Uniformity Transfer

In order to track the non-uniformity through the compressor in the NURM method, the transfer of non-uniformity across each blade row is characterized using transfer functions. Transfer functions are defined for each shape parameter of the radial $\rho V_x r$ and incidence profiles as

$$k_a = \frac{\Delta(SH)_{outlet}}{\Delta(SH)_{inlet}}, \tag{4.1}$$

where SH denotes the shape parameter. The shape parameter corresponding to the profile from the reference database is denoted the datum shape parameter, and $\Delta(SH) = (SH) - (SH)_{datum}$. The overall non-uniformity at the blade row outlet can be calculated using the known outlet datum shape parameter as:

$$(SH)_{outlet} = (SH)_{datum,outlet} + k_a \Delta(SH)_{inlet} \tag{4.2}$$

The data from the performance sensitivity study was used to calculate the transfer function for each shape parameter at each of the six operating points. As expected the non-uniformity transfer varies with operating point and with blade row inlet non-uniformity. In the NURM method each transfer function is characterized as a function of incidence, relative Mach number, and the departure from datum inlet non-uniformity: $k_a = k_a(\bar{i}, \overline{M}_{rel}, \Delta(SH)_{inlet})$. Contours of the transfer functions across the operating map are shown in Figures 4-17 and 4-18. The data reveals that blade rows tend to attenuate non-uniformity, resulting in transfer function values less than one. This suggests that the non-uniformity of the flow in embedded stages of multistage axial compressors has a datum condition at each operating point, corresponding to the datum computation database, and departures from the datum non-uniformity at stage inlet will be reduced across the stage. This is a first attempt at characterizing the transfer of non-uniformity through a compressor, and time constraints prevented an investigation into the mechanisms behind these trends. It would be useful to gain a deeper understanding of this process to aid in the development of future iterations

of the NURM method.

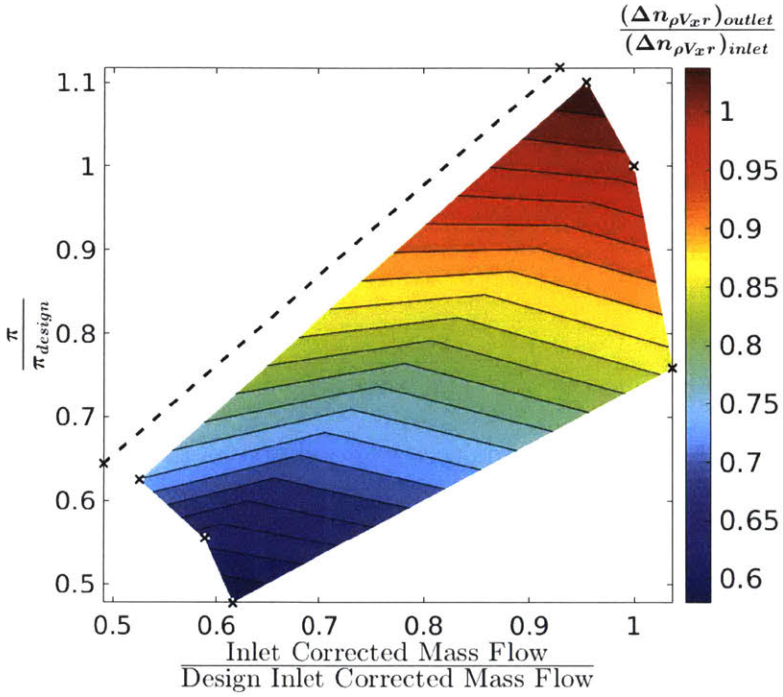

Figure 4-17: Transfer of non-uniformity across blade row varies with operating point. $n_{\rho V_x r}$ shown.

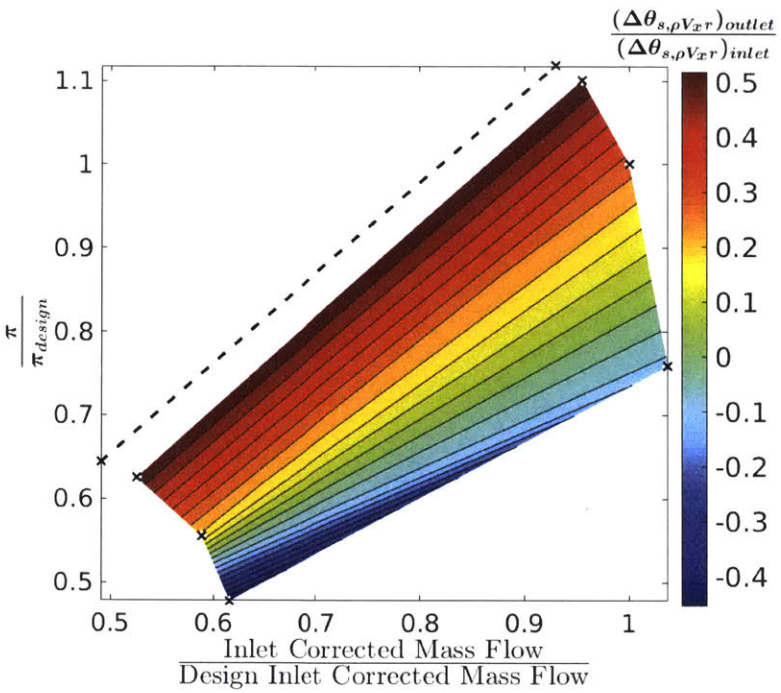

Figure 4-18: Departures from datum attenuated across blade row for most shape parameters and operating points. $\theta_{s,\rho V_x r}$ shown.

4.4 Conclusions

The key outcomes of the characterization of the link between non-uniformity and performance are:

- Impact of non-uniformity on performance is characterized quantitatively in a manner suitable for incorporation into the NURM method
- Changes in $\rho V_x r$ and incidence non-uniformity cause changes on order of 1% in blade row performance, are important to be captured in NURM method
- Changes in total temperature non-uniformity cause changes on order of 0.1% in blade row performance, are negligible compared to effects of changes in $\rho V_x r$ and incidence non-uniformity
- Dependence on operating point of impact of non-uniformity on performance captured in NURM method using sensitivity study data from multiple operating points

Chapter 5

Performance Estimation Method

The basis function representation of radial flow profiles, characterization of the link between non-uniformity and performance, and characterization of the transfer of non-uniformity through the compressor provide the necessary elements for the incorporation of radial flow non-uniformity and its impact on blade row performance into a 1D method for off-design compressor performance estimation. This chapter describes a first implementation of this conceptual approach.

The implementation is based on Joerger's meanline method [16]. In this meanline calculation, the blade row outlet meanline conditions are determined from the blade row inlet meanline conditions, the stagnation pressure loss coefficient, the deviation angle, and the blockage factor using conservation of rothalpy, continuity, and velocity triangle geometry. The calculation across a single blade row is described here, and this process is repeated across each blade in the compressor. The calculation across an entire stage is given in full detail in Appendix A. Station definitions and velocity triangle conventions are shown in Figures 5-1 and 5-2.

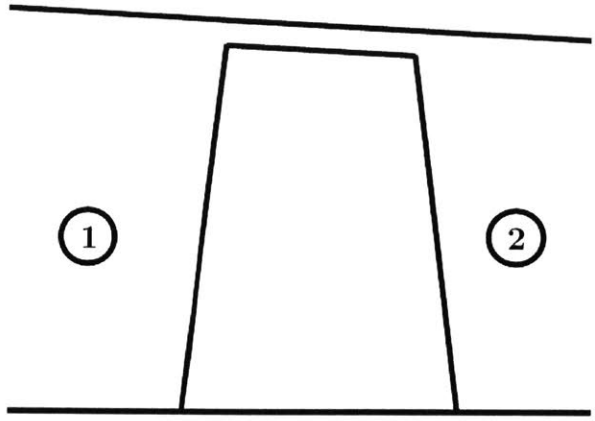

Figure 5-1: Blade row inlet and outlet stations denoted 1 and 2, respectively.

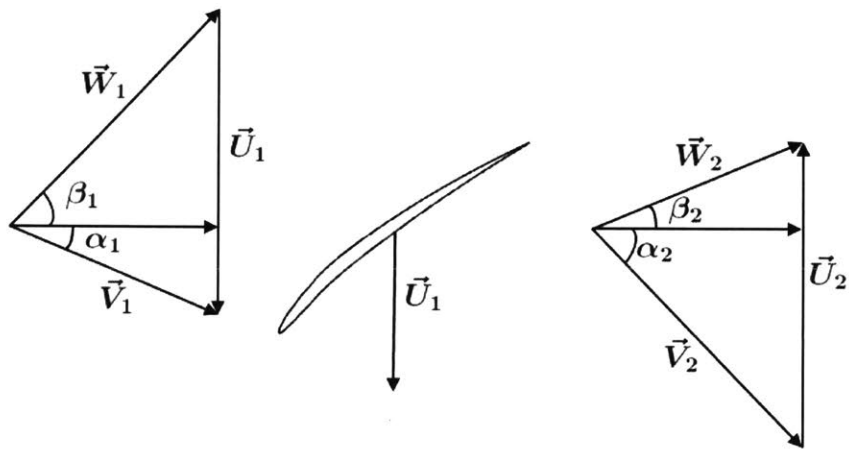

Figure 5-2: Velocity and angle conventions.

5.1 1D Meanline Calculation

At the inlet to any blade, $P_{t,1}$, $T_{t,1}$, $M_{abs,1}$, α_1, and the shape parameters $n_{\rho V_x r,1}$, $\theta_{s,\rho V_x r,1}$, $\theta_{o,\rho V_x r,1}$, $\theta_{e,\rho V_x r,1}$, $n_{inc,1}$, $\theta_{s,inc,1}$, $\theta_{o,inc,1}$, and $\theta_{e,inc,1}$ are known. From $P_{t,1}$, $T_{t,1}$, $M_{abs,1}$, α_1 and the blade speed $U_1 = \Omega r_{mean,1}$ the relative conditions at station 1 are determined using isentropic relations and velocity triangle geometry. For a set of known stagnation pressure loss coefficient, deviation angle, and blockage factor are determined, the blade row outlet conditions are computed using those performance parameters as follows:

From conservation of rothalpy the blade row outlet relative stagnation temperature can be determined from the blade row inlet relative stagnation temperature and the blade speeds at inlet and outlet using Equations 5.1 - 5.3.

$$h_{t,rel,1} = \frac{R\gamma}{\gamma - 1} T_{t,rel,1} \tag{5.1}$$

$$h_{t,rel,2} = h_{t,rel,1} + \frac{U_2^2 - U_1^2}{2} \tag{5.2}$$

$$T_{t,rel,2} = \frac{h_{t,rel,2}}{\frac{R\gamma}{\gamma-1}} \tag{5.3}$$

With $T_{t,rel,2}$, the blade row outlet relative stagnation pressure can be calculated from the loss coefficient as:

$$P_{t,rel,2,isen} = P_{t,rel,1} \left(\frac{T_{t,rel,2}}{T_{t,rel,1}} \right)^{(\frac{\gamma}{\gamma-1})} \tag{5.4}$$

$$P_{t,rel,2} = P_{t,rel,2} - \overline{\omega}(P_{t,rel,1} - P_1) \tag{5.5}$$

The blade row outlet relative flow angle is simply the sum of the blade row outlet blade metal angle and the deviation angle, $\beta_2 = \chi_2 + \overline{\delta}$. With the relative stagnation conditions and relative flow angle at station 2 known, the static conditions must be determined and with them the absolute stagnation conditions. A new equation was derived using conservation of rothalpy, isentropic relations, velocity triangles, continuity, and the definition of Mach number to give an implicit expression for $V_{x,2}$ in terms of known quantities and the meanline $\rho V_x r$, $(\overline{\rho V_x r})$:

$$V_{x,2} = \frac{(\overline{\rho V_x r})_2 R T_{t,rel,2} \left(1 + \frac{\gamma-1}{2} \left(\frac{1}{\frac{\gamma R T_{t,rel,2}}{V_{x,2}^2 (1+tan^2(\beta_2))} - \frac{\gamma-1}{2}} \right) \right)^{\frac{1}{\gamma-1}}}{P_{t,rel,2} r_{mean,2}} \tag{5.6}$$

This equation enables the use of a mass-average $\rho V_x r$ which could be directly determined from a radial $\rho V_x r$ profile. For this implementation the non-uniformity is

expressed as non-dimensional profiles fully decoupled from the 1D meanline values, so the meanline $\rho V_x r$ is instead determined from the blockage factor as:

$$\overline{\rho V_x r} = \frac{\dot{m}}{2\pi(1-k_b)(r_{max}-r_{min})} \tag{5.7}$$

Where $\overline{r}$ is taken to be $\frac{r_{max}+r_{min}}{2}$. With the axial velocity known, the downstream relative Mach number, static conditions and absolute stagnation conditions can all be computed using velocity triangle geometry and isentropic relations. This completes the meanline blade row calculation. All conditions are known at the blade row exit for use as the inlet conditions to the downstream blade row. This process is repeated across each blade row of the compressor, with the only change being that for stators U_1 is zero.

5.1.1 Database Approach to Blade Row Performance Characterization

The blade row performance parameters $\overline{\omega}$, $\overline{\delta}$, and k_b are characterized as functions of operating point using 3D multistage CFD computations. This approach was developed by Kulkarni for his stage-stacking method [15], and it brings high-fidelity 3D CFD results directly into a 1D performance estimation method. A database of CFD results from across the operating map is used to determine the functional dependence of performance on operating point. Kulkarni implemented this by fitting the performance parameters as functions of flow coefficient, and Joerger expanded on this by fitting them as 2D functions of relative Mach number and incidence [16]. Joerger's approach is used in this implementation of the NURM method. All three parameters were adequately captured by the same polynomial form, given in Equation 5.8. Example databases are shown in Figure 5-3.

$$f(\overline{i}, \overline{M}_{rel}) = c_1 + c_2\overline{i} + c_3\overline{M}_{rel} + c_4\overline{M}_{rel}\overline{i} + c_5\overline{M}_{rel}^2\overline{i} + c_6\overline{M}_{rel}\overline{i}^2 + c_7\overline{i}^3 + c_8\overline{M}_{rel}^3 \tag{5.8}$$

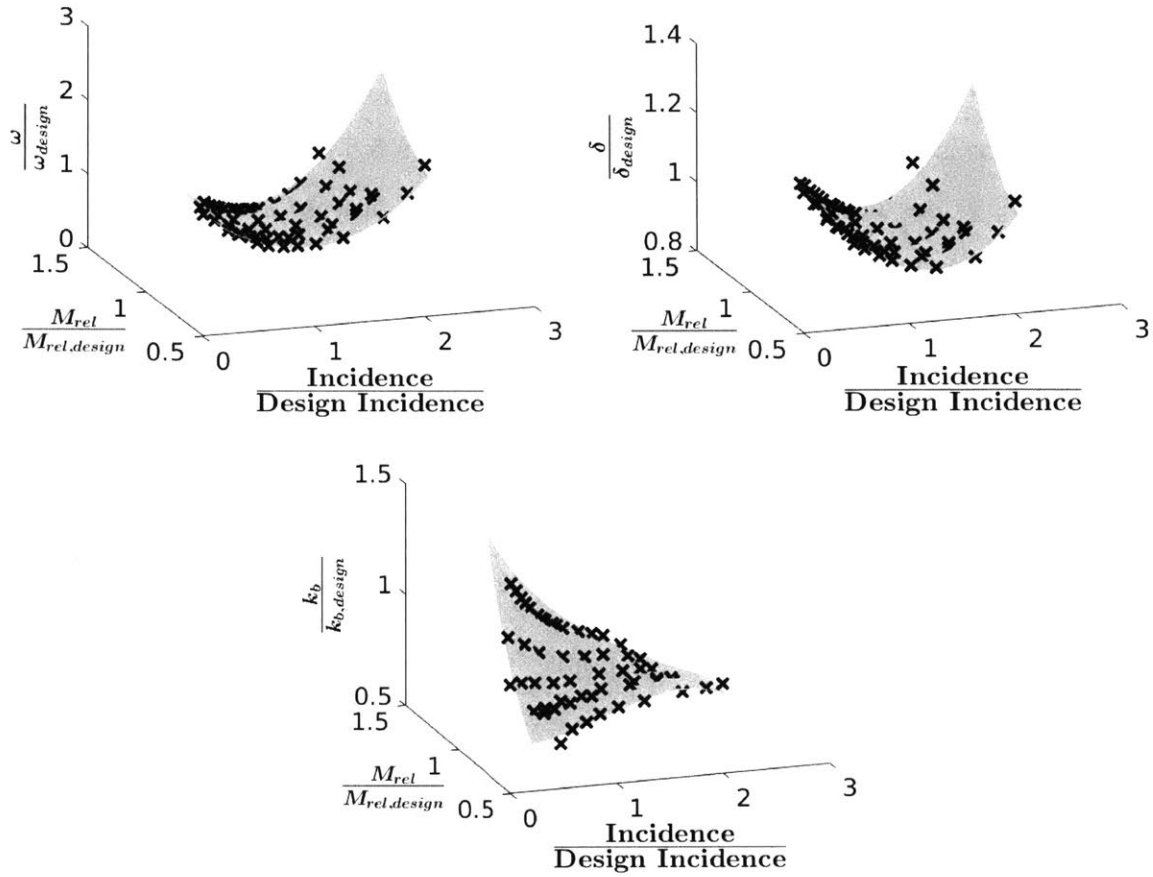

Figure 5-3: Polynomial representations of performance parameter databases provide continuous surfaces and allow for extrapolation beyond range covered by data. Rotor 3 of test compressor shown.

5.1.2 Enhanced Blockage Estimation Method

A new aspect of the NURM method meanline calculation is the characterization of the blockage at each station as a function of the incidence and Mach number at that station. The methods of Kulkarni and Joerger set blade row outlet blockage as a function of blade row inlet conditions, which provides for simpler implementation but is not as representative of compressor behavior. The incorporation of this dependence into the NURM method required the addition of an iteration loop because the blade row outlet conditions themselves depend on the blade row outlet blockage. In the NURM method, after the downstream relative stagnation conditions have been determined from Equations 5.2 - 5.5, an initial estimate is made of the blade row

outlet axial velocity $V_{x,2}$. The blade row outlet conditions are calculated using this estimated, and $k_{b,2}$ is determined from the station 2 blockage database using the blade row outlet Mach number and the incidence of the downstream blade row. This blockage factor is used to compute $(\overline{\rho V_x r})$, and Equation 5.6 is solved for $V_{x,2}$. If this calculated $V_{x,2}$ does not match the initial estimate, the process is repeated with an updated estimate until the values converge.

5.2 Non-Uniformity Transfer

In parallel with the meanline calculation, non-uniformity is transferred through the compressor. At each station the datum non-uniformity, meaning the non-uniformity in the datum computations used to establish the performance parameter databases, is characterized as a function of operating point. The same database approach used for the performance parameters is used to characterize the functional dependence of the datum non-uniformity, represented using shape parameters, on incidence and relative Mach number. Databases are established for each shape parameter of the $\rho V_x r$ and incidence profiles ($n_{\rho V_x r}$, $\theta_{s,\rho V_x r}$, $\theta_{o,\rho V_x r}$, $\theta_{e,\rho V_x r}$, n_{inc}, $\theta_{s,inc}$, $\theta_{o,inc}$, and $\theta_{e,inc}$), as shown conceptually in Figure 5-4.

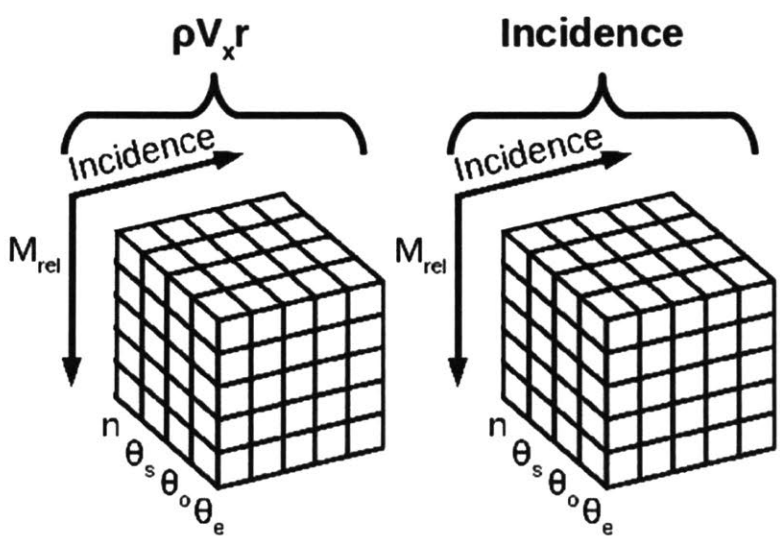

Figure 5-4: Databases established for each shape parameter of $\rho V_x r$ and incidence profiles.

Departures from the datum blade row inlet non-uniformity are transferred across the blade row using the transfer function k_a. It is shown in Section 4.3 that the transfer of departures from datum non-uniformity across a blade row depends on incidence and Mach number, and also on the blade row inlet departure from datum non-uniformity. To capture this 3-dimensional functional dependence, linear interpolation is used rather than a polynomial. Extrapolation is not used beyond the range of the study data. The nearest value within the data range is used instead. This is necessary because of the limited range of data in terms of inlet non-uniformity, which could lead to extreme extrapolation errors. A transfer function is determined for each shape parameter of the $\rho V_x r$ and incidence profiles using this method, e.g. $k_{a,n,\rho V_x r} = k_{a,n,\rho V_x r}(\bar{i}, \overline{M}_{rel}, (\Delta n_{\rho V_x r})_1)$. The blade row outlet departure from datum non-uniformity can be calculated from the blade row inlet departure and the transfer function as:

$$(\Delta n_{\rho V_x r})_2 = k_{a,n,\rho V_x r}(\Delta n_{\rho V_x r})_1 \tag{5.9}$$

And once the meanline conditions at station 2 are known, the datum shape parameters can be determined using their respective databases and the station 2 non-uniformity is given by:

$$n_{\rho V_x r,2} = n_{\rho V_x r,2,datum} + (\Delta n_{\rho V_x r})_2 \tag{5.10}$$

5.3 Effect of Flow Non-Uniformity on Blade Row Performance

This knowledge of the non-uniformity at every station allows for characterization of the impact of inlet flow non-uniformity on blade row performance. From the sensitivity study described in Chapter 4 this is quantified in terms of partial derivatives of stagnation pressure loss coefficient, deviation angle, and blockage factor with respect to each shape parameter. The difference in performance from the datum performance

can be captured using the departure from the datum inlet shape parameters and the partial derivatives of performance with respect to shape parameter. The functional dependence of the performance corrections on operating point is captured using the polynomial form in incidence and Mach number shown in Equation 5.11.

$$f(\bar{i}, \overline{M}_{rel}) = c_1 + c_2\bar{i} + c_3\overline{M}_{rel} + c_4\overline{M}_{rel}\bar{i} \tag{5.11}$$

The loss coefficient, deviation angle, and blockage factor are altered for departures in each shape parameter of the $\rho V_x r$ and incidence profiles. For example, the altered loss coefficient is calculated as:

$$\begin{aligned}\overline{\omega}_{altered} = \overline{\omega} + & \frac{\partial\overline{\omega}}{\partial n_{\rho V_x r,1}}(\Delta n_{\rho V_x r})_1 + \frac{\partial\overline{\omega}}{\partial\theta_{s,\rho V_x r,1}}(\Delta\theta_{s,\rho V_x r})_1 + \\ & \frac{\partial\overline{\omega}}{\partial\theta_{o,\rho V_x r,1}}(\Delta\theta_{o,\rho V_x r})_1 + \frac{\partial\overline{\omega}}{\partial\theta_{e,\rho V_x r,1}}(\Delta\theta_{e,\rho V_x r})_1 + \\ & \frac{\partial\overline{\omega}}{\partial n_{inc,1}}(\Delta n_{inc})_1 + \frac{\partial\overline{\omega}}{\partial\theta_{s,inc,1}}(\Delta\theta_{s,inc})_1 + \\ & \frac{\partial\overline{\omega}}{\partial\theta_{o,inc,1}}(\Delta\theta_{o,inc})_1 + \frac{\partial\overline{\omega}}{\partial\theta_{e,inc,1}}(\Delta\theta_{e,inc})_1\end{aligned} \tag{5.12}$$

These altered performance parameters are used in the 1D performance calculations. The entire blade row calculation process with all elements included is diagrammed in Figure 5-5.

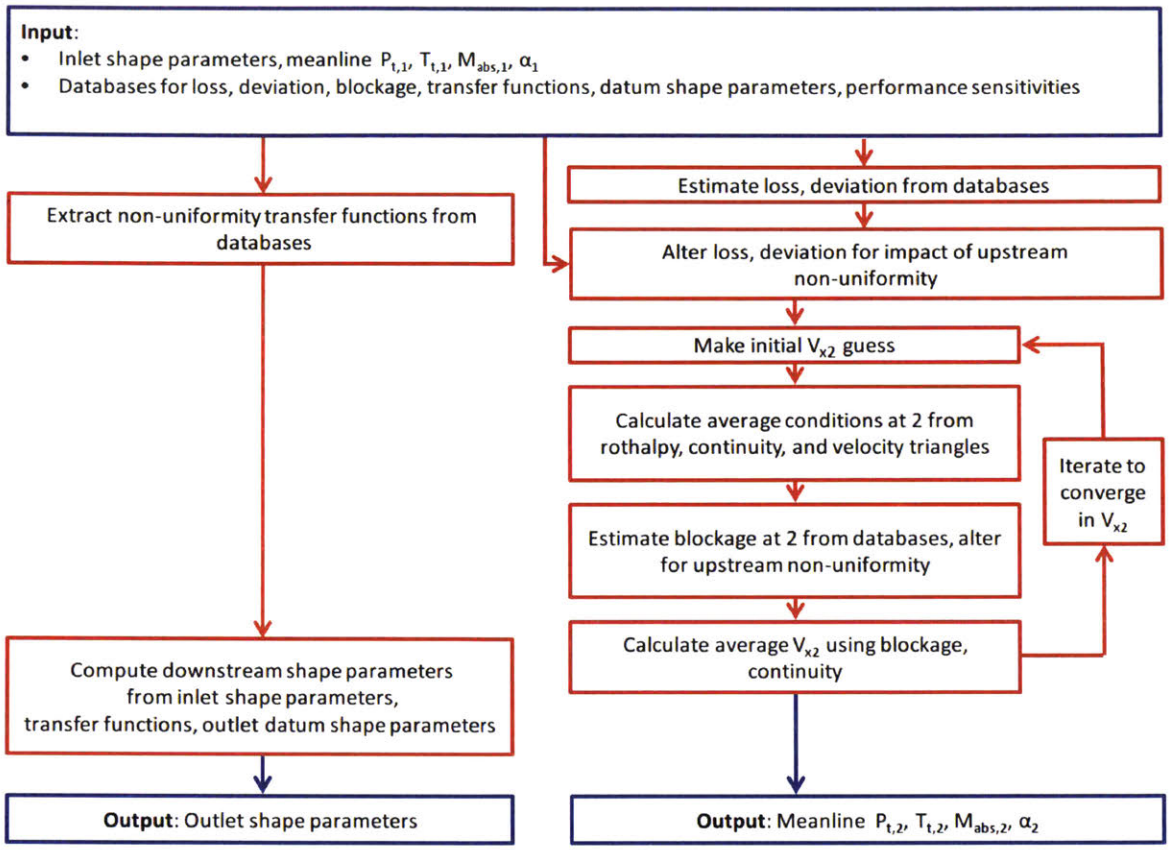

Figure 5-5: Non-uniformity transfer across blade rows enables correction of performance for impact of inlet flow non-uniformity.

5.4 Conclusions

This preliminary implementation of the NURM method revealed several areas for improvement. The radial profiles at each station enable the direct computation of mass-averages. This could be used to determine the blade row outlet conditions in terms of radial profiles and their mass-averages without requiring loss coefficients, deviation angles, or blockage factors. The information could instead be captured in the transfer of non-uniformity across the blade row. This would also provide a means of incorporating the impact of changes in blade geometry by capturing their impact on non-uniformity transfer.

Chapter 6

Capability Demonstration

Three test cases were run to demonstrate the capabilities of the NURM method. To demonstrate the capability of the method to capture both the meanline performance and the radial flow non-uniformity at each station in the case of datum rotor one inlet flow non-uniformity, the method was run across the datum operating map of the test compressor. To demonstrate the capability of the method to estimate meanline performance and radial non-uniformity for speeds at which no CFD data is available, the method was run across the 85% speed line, again with datum rotor one inlet flow non-uniformity. Finally, to demonstrate the capability of the method to transfer off-design radial flow non-uniformity through the compressor a test case was run with off-design rotor one inlet flow non-uniformity. For these demonstrations the meanline computations were begun at the rotor 1 inlet of the test compressor. The demonstrations and their results are detailed in the following sections.

This implementation of the NURM method was found to adequately capture compressor performance and non-uniformity transfer for datum compressor inlet non-uniformity and to capture the transfer of off-design inlet non-uniformity through the compressor. This indicates that the methods developed for representation and transfer of non-uniformity are suitable for use in an off-design compressor performance method.

6.1 Datum Compressor Assessment

The NURM methodology was demonstrated across the test compressor operating map with datum radial inlet profiles, as shown in Figure 6-1. In addition to the meanline performance estimation, NURM has the capability to track radial flow non-uniformity at each station through the compressor. The departure from the datum non-uniformity is transferred across each blade row, and in this case that departure is zero. The NURM profiles are compared with the CFD profiles at design, near stall, and near choke operating points on the 100% speed line in Figures 6-2 - 6-4. The NURM profiles capture the elements and attributes of non-uniformity described in Chapter 2. The endwall blockage and radial skew are both captured. The NURM method also effectively captures the exacerbation of non-uniformity across rotors and attenuation across stators resulting from the presence of rotor tip leakage in a repeating stage environment as described by Horlock [10].

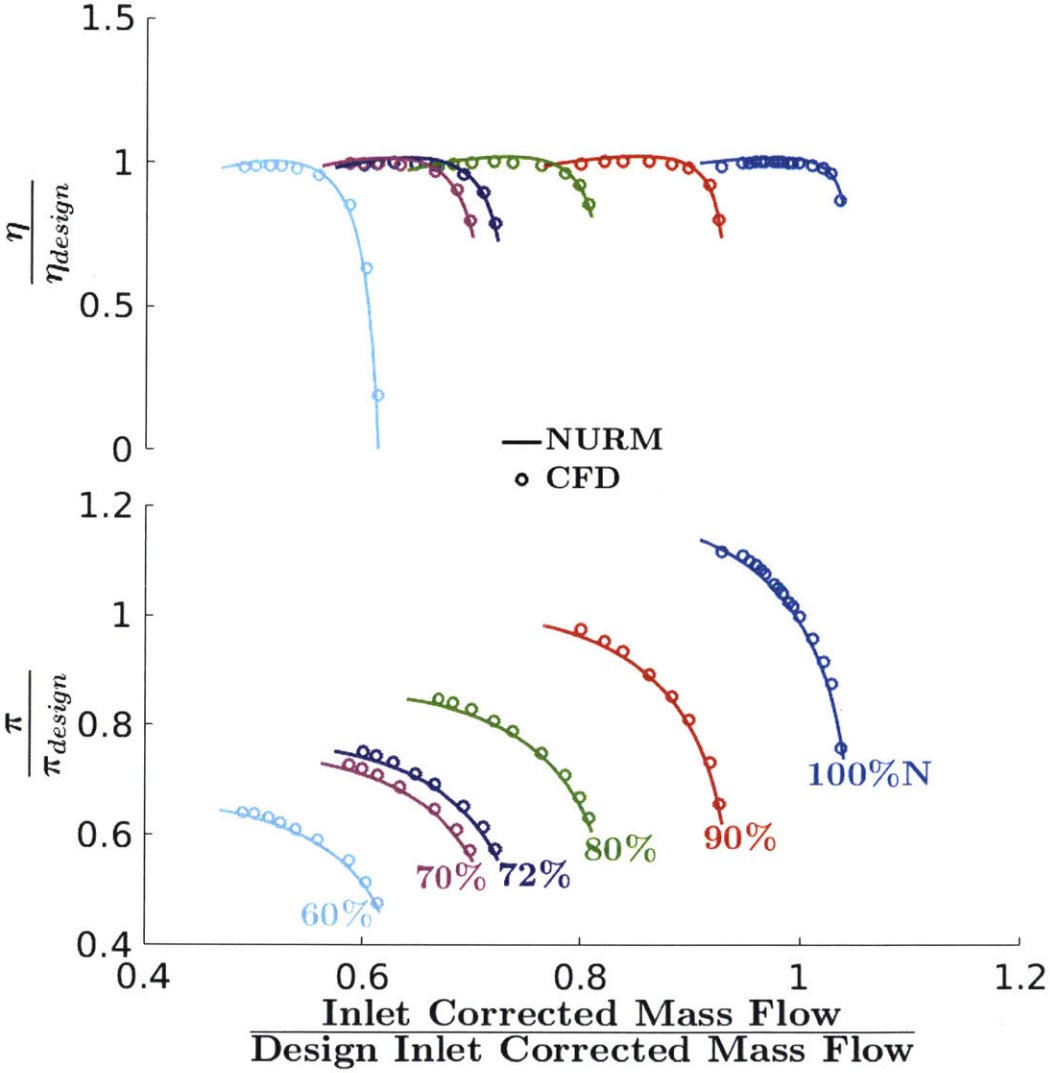

Figure 6-1: NURM methodology meanline performance matches CFD trends across datum compressor operating map.

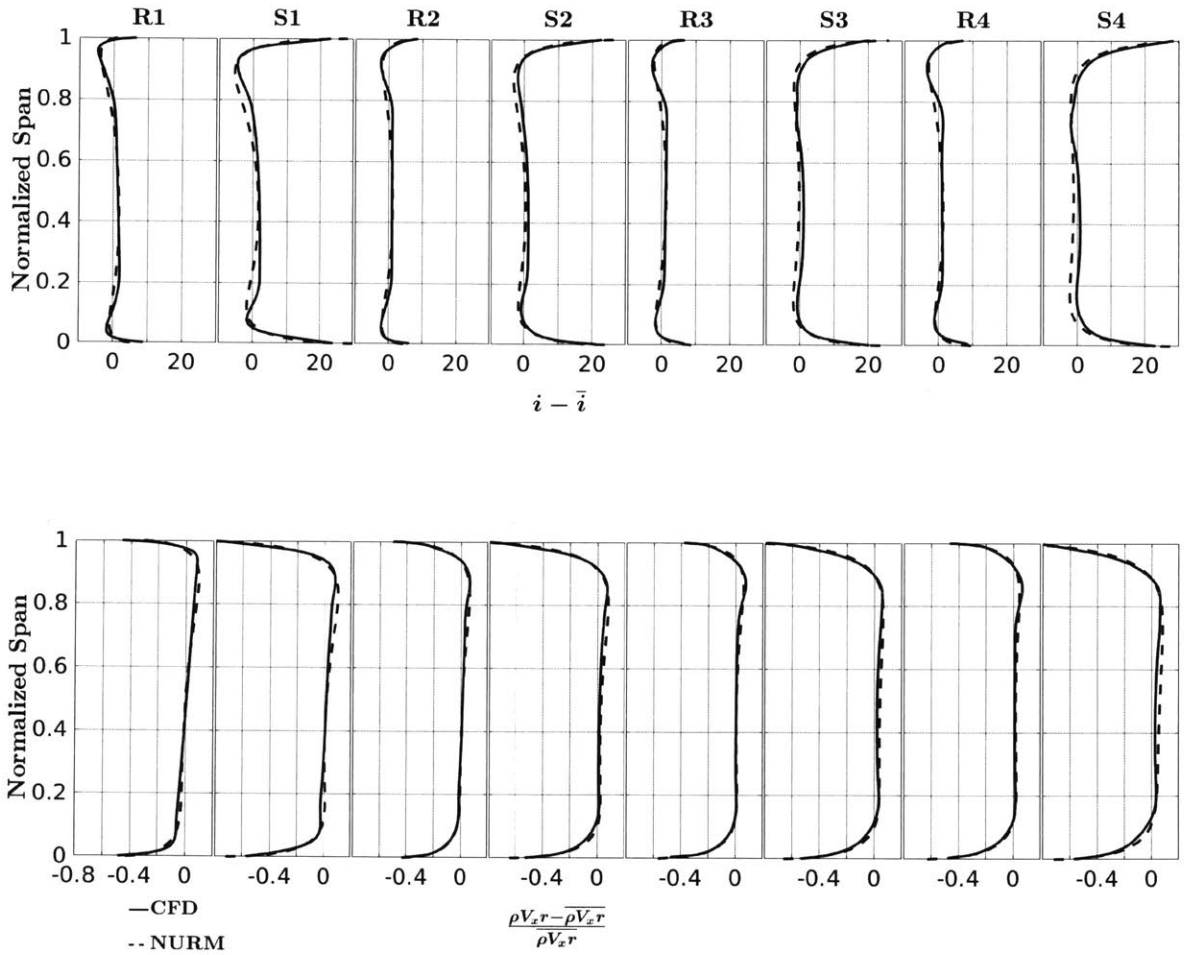

Figure 6-2: Radial flow profiles estimated at every station by transferring departures from datum non-uniformity across each blade row. 100%N design point shown. Dashed profiles are NURM estimations, solid profiles are CFD results.

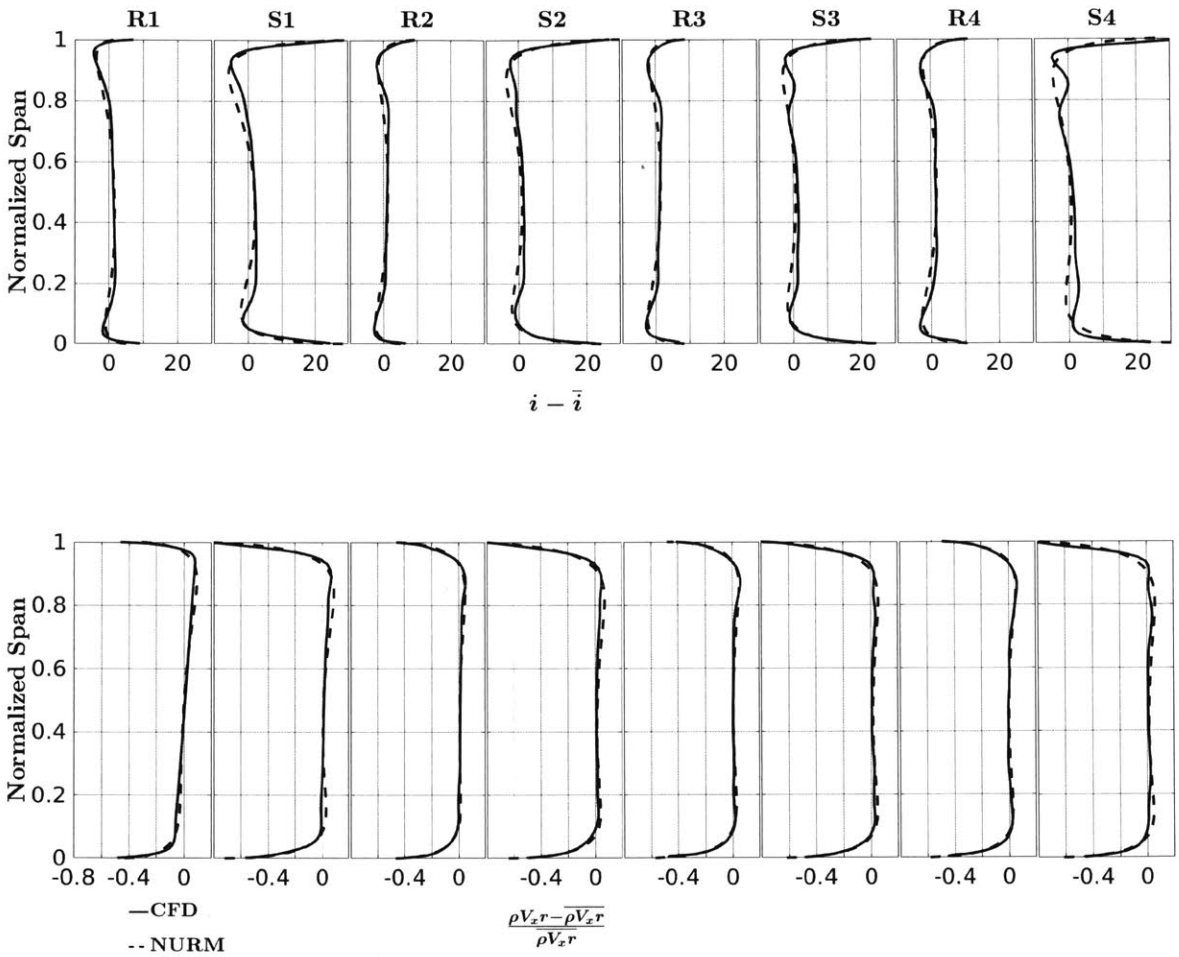

Figure 6-3: Radial flow profiles estimated at every station by transferring departures from datum non-uniformity across each blade row. 100%N near choke shown. Dashed profiles are NURM estimations, solid profiles are CFD results.

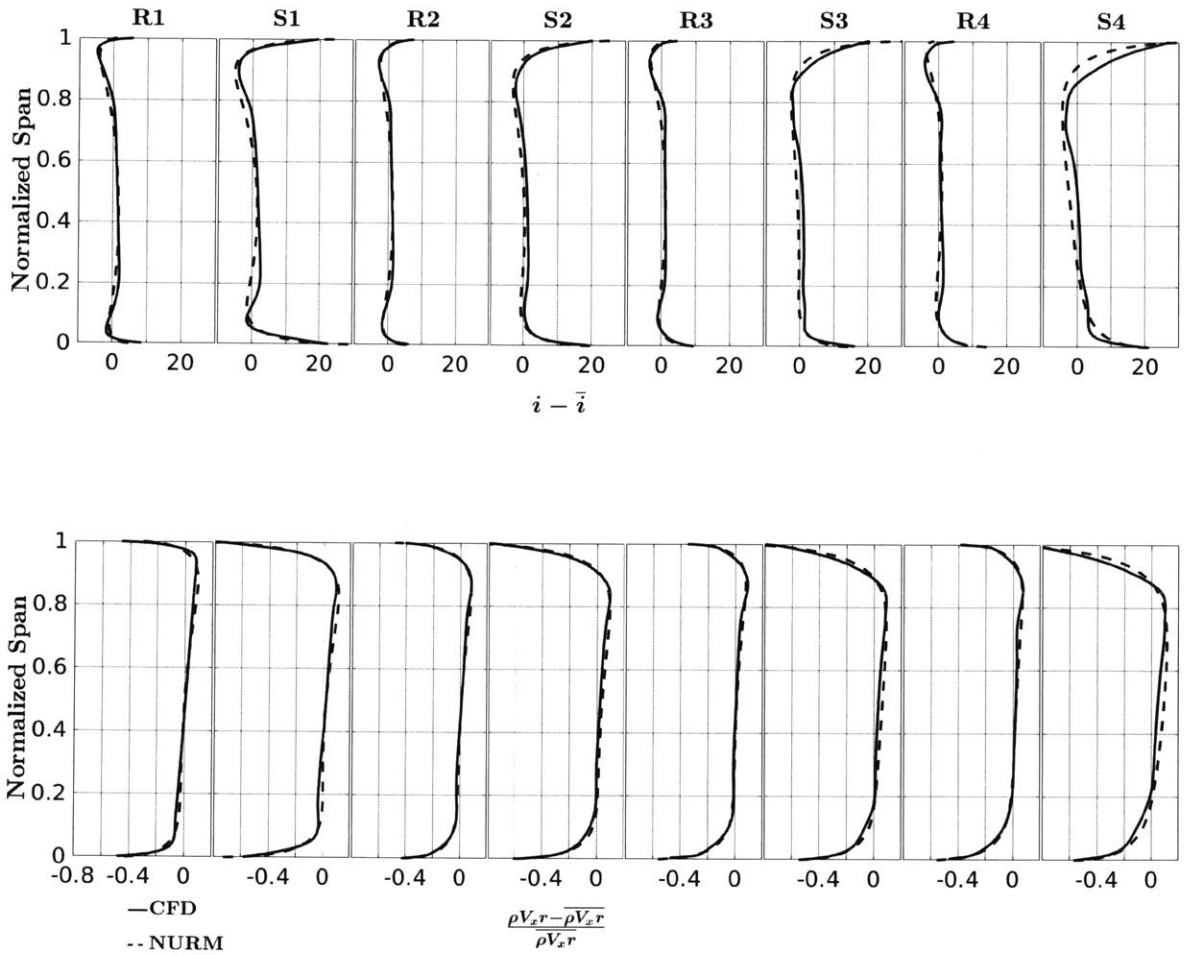

Figure 6-4: Radial flow profiles estimated at every station by transferring departures from datum non-uniformity across each blade row. 100%N near stall shown. Dashed profiles are NURM estimations, solid profiles are CFD results.

6.2 Estimated Compressor Performance at 85% Speed

To demonstrate the capability of the NURM method to capture the non-uniformity transfer and performance at speeds for which CFD results are not available, the method was run across the 85% speed line. Figure 6-5 shows the meanline performance estimation. The performance trends across the speed line match those of the surrounding speed lines. As above, in addition to the performance estimation, the radial flow profiles are estimated at each station. The near peak efficiency, near choke, and near stall points are marked, and the estimated radial profiles at those points are shown in Figures 6-6 - 6-8. The evolution of non-uniformity through the compressor is as expected. The endwall blockage and radial skew in mass flow resemble those at the design speed, and the alternating exacerbation and attenuation of non-uniformity across rotors and stators is captured. This capture of the trends shows the effectiveness of the database representations in interpolating the datum shape parameters and non-uniformity transfer functions between known data points.

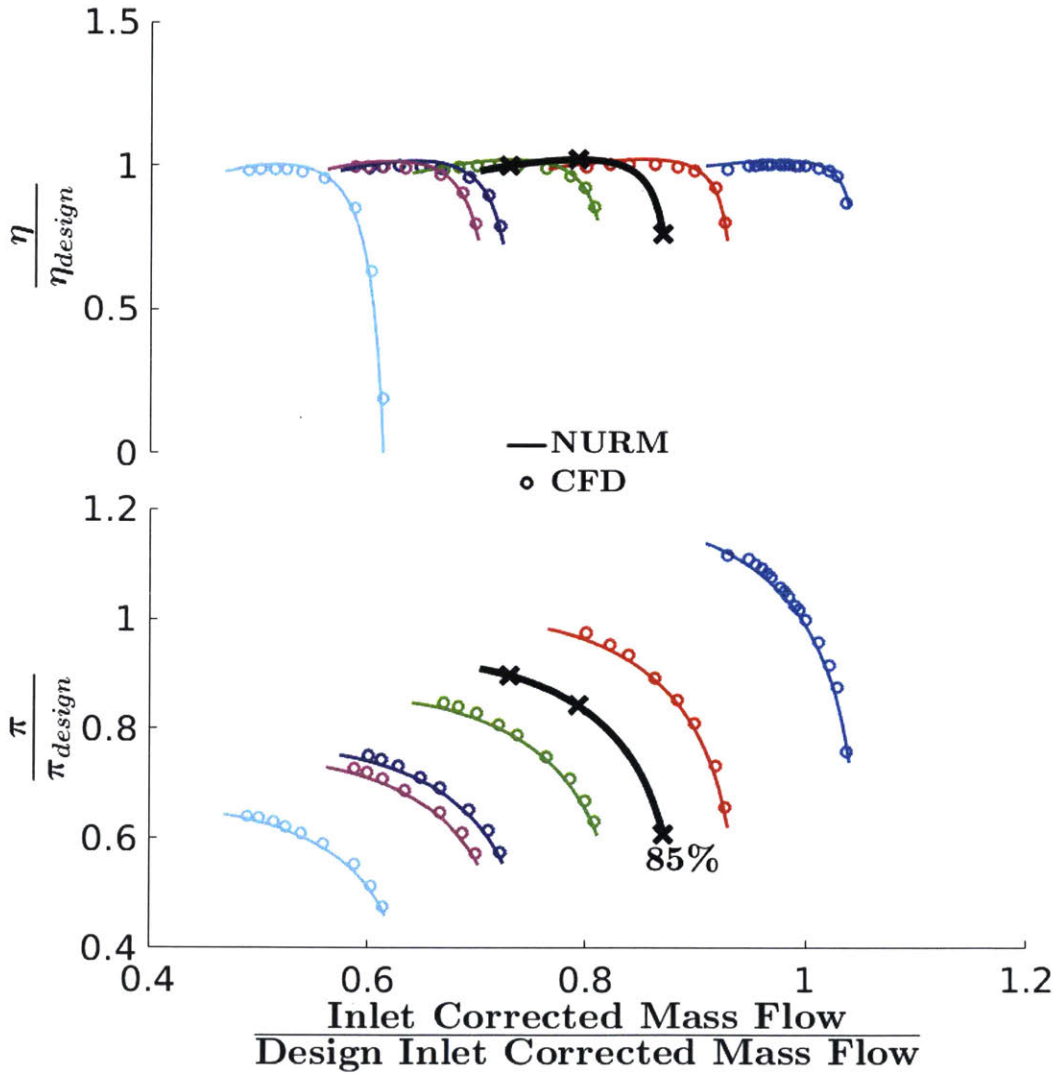

Figure 6-5: NURM methodology meanline performance estimations for speed for without CFD data matches trends of surrcounding speeds.

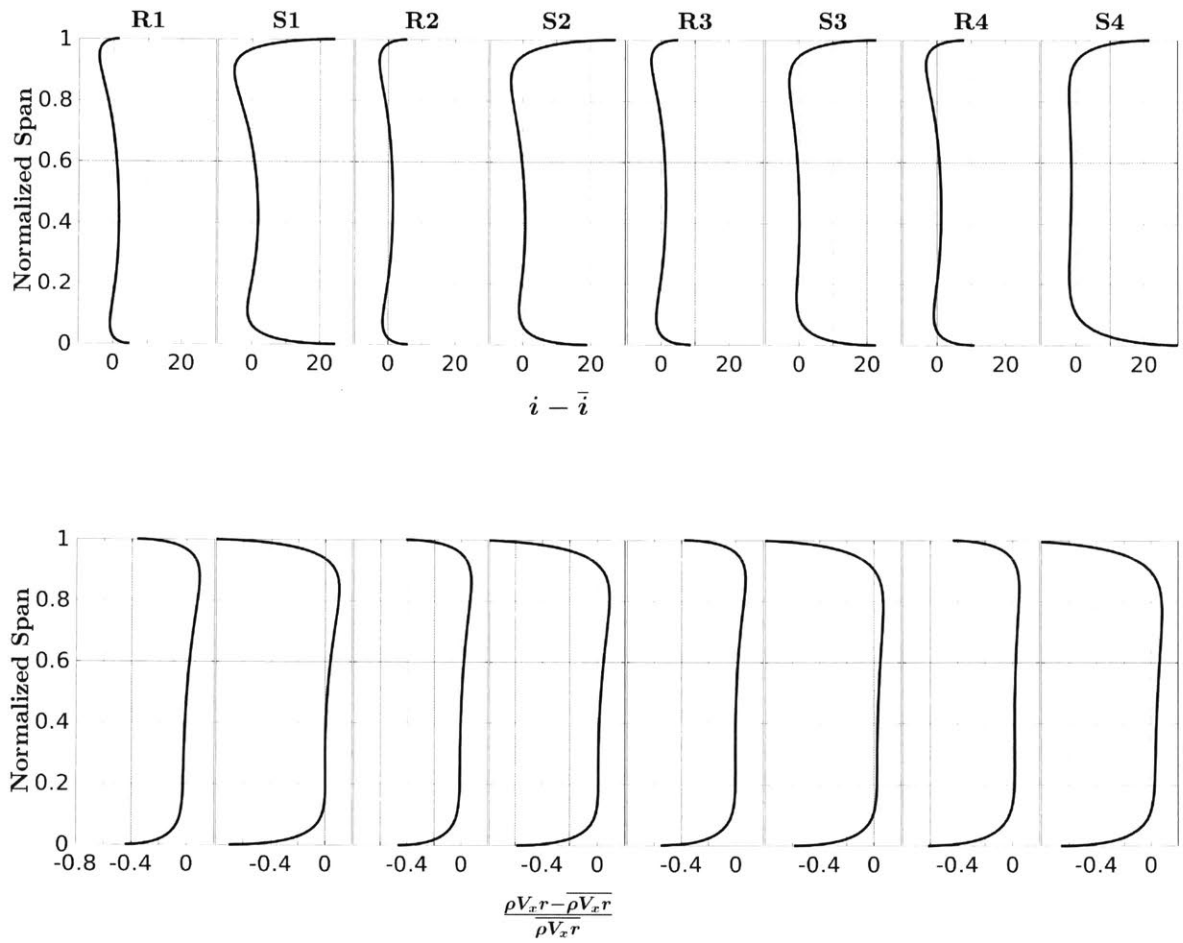

Figure 6-6: Trends in radial flow non-uniformity for point on speed line without CFD data match those at design speed. 85%N near peak efficiency shown.

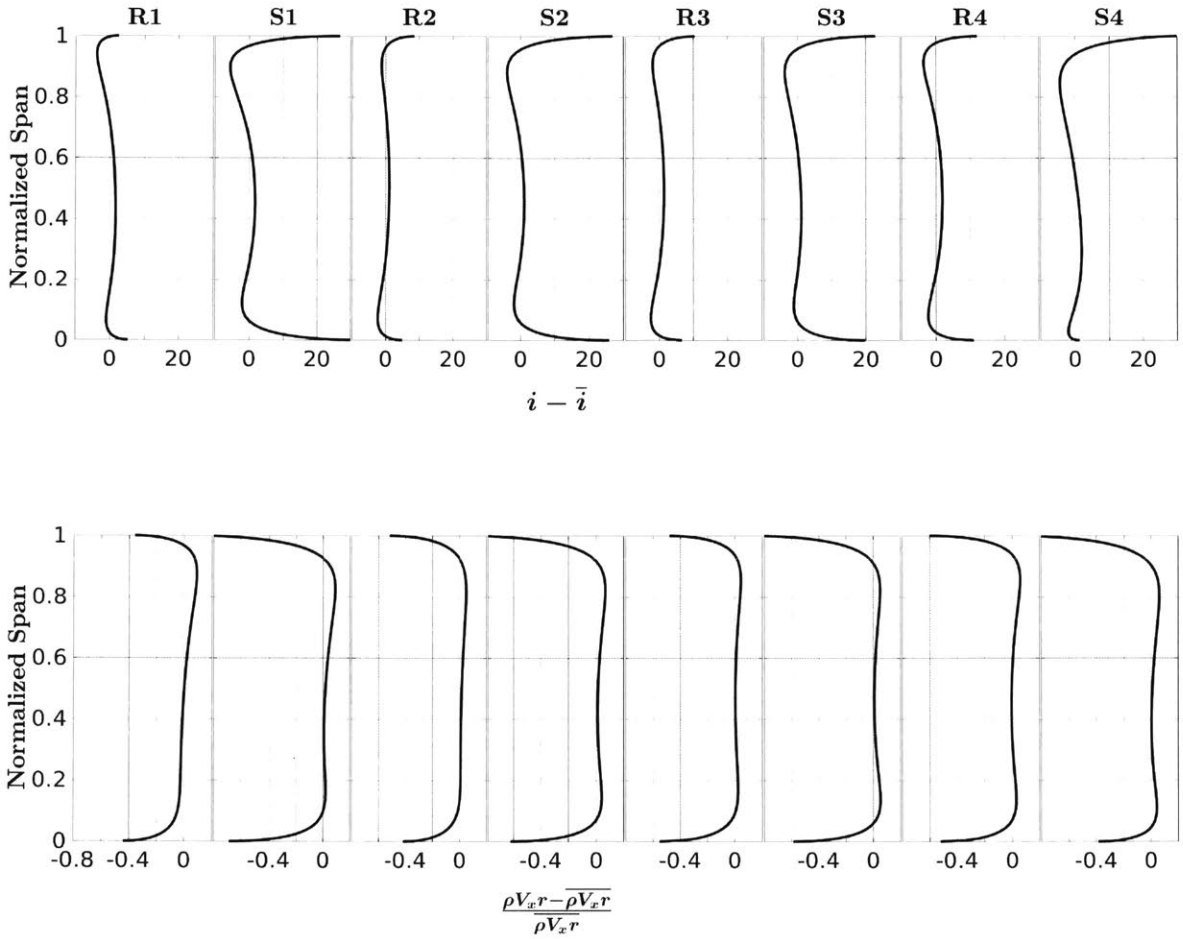

Figure 6-7: At 85%N near choke trends in radial flow non-uniformity for point on speed line without CFD data again match those at design speed.

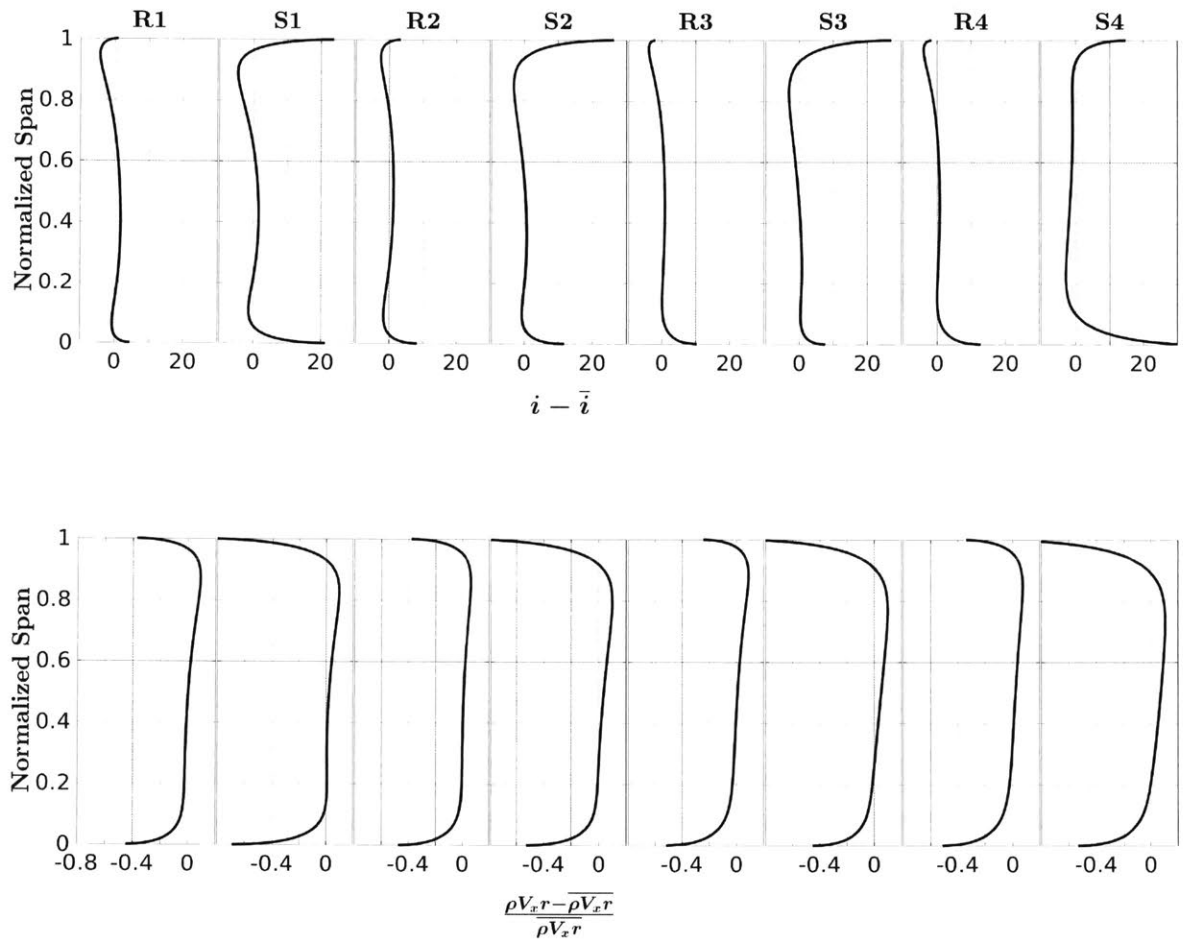

Figure 6-8: Once again at 85%N near stall trends in radial flow non-uniformity for point on speed line without CFD data match those at design speed.

6.3 Off-Design Inlet Non-Uniformity Assessment

To demonstrate the capability of the NURM method to transfer off-design radial inlet flow non-uniformity through the compressor a test case was run using rotor one inlet profiles with radial mass flow and incidence skew. The inlet profiles for this test case are shown in Figure 6-9. The mass flow rate per unit span profile is skewed with a variation of 32% between 5% and 95% span. The actual non-uniformity transfer determined using three-dimensional CFD computations at design and off-design conditions is shown in Figure 6-10. The non-uniformity is attenuated across the first stage. This attenuation is consistent with the sensitivity study results from Section 4.3 which showed that departures from datum non-uniformity tend to be attenuated across a blade row. Figure 6-11 shows the NURM estimation compared to the off-design CFD. The NURM method captures the attenuation of non-uniformity across the first stage. At the rotor two inlet the shape of the NURM profile matches that of the CFD profile. To confirm that NURM captures the trends in non-uniformity transfer for off-design inlet profiles, the NURM estimations for off-design and design profiles are compared in Figure 6-12. Comparison to Figure 6-10 confirms that the NURM method captures the trends in the transfer of non-uniformity through the compressor, including the attenuation of the non-uniformity across the first stage.

The NURM computation overestimates the impact of the change in compressor inlet non-uniformity on performance. Table 6.1 presents the changes in compressor performance resulting from the change in inlet flow non-uniformity for both CFD and NURM relative to the respective datum computations of each. In spite of the performance estimation errors, the effective transfer of non-uniformity through the compressor indicates that the foundation of the method is firm. The performance estimation accuracy may be improved through the acquisition of additional data and improvement upon this first implementation.

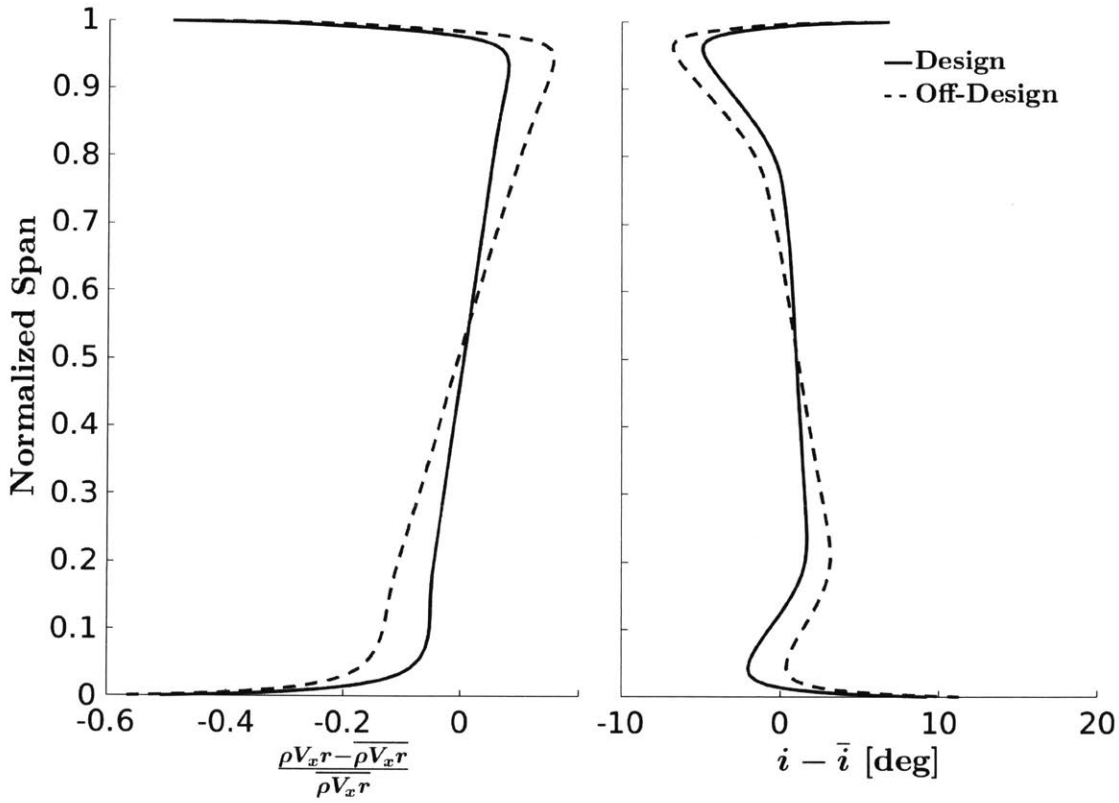

Figure 6-9: Radially skewed inlet profiles used to test capability of NURM to transfer off-design non-uniformity through compressor. 32% variation in mass flow rate per unit span from 5% to 95% span.

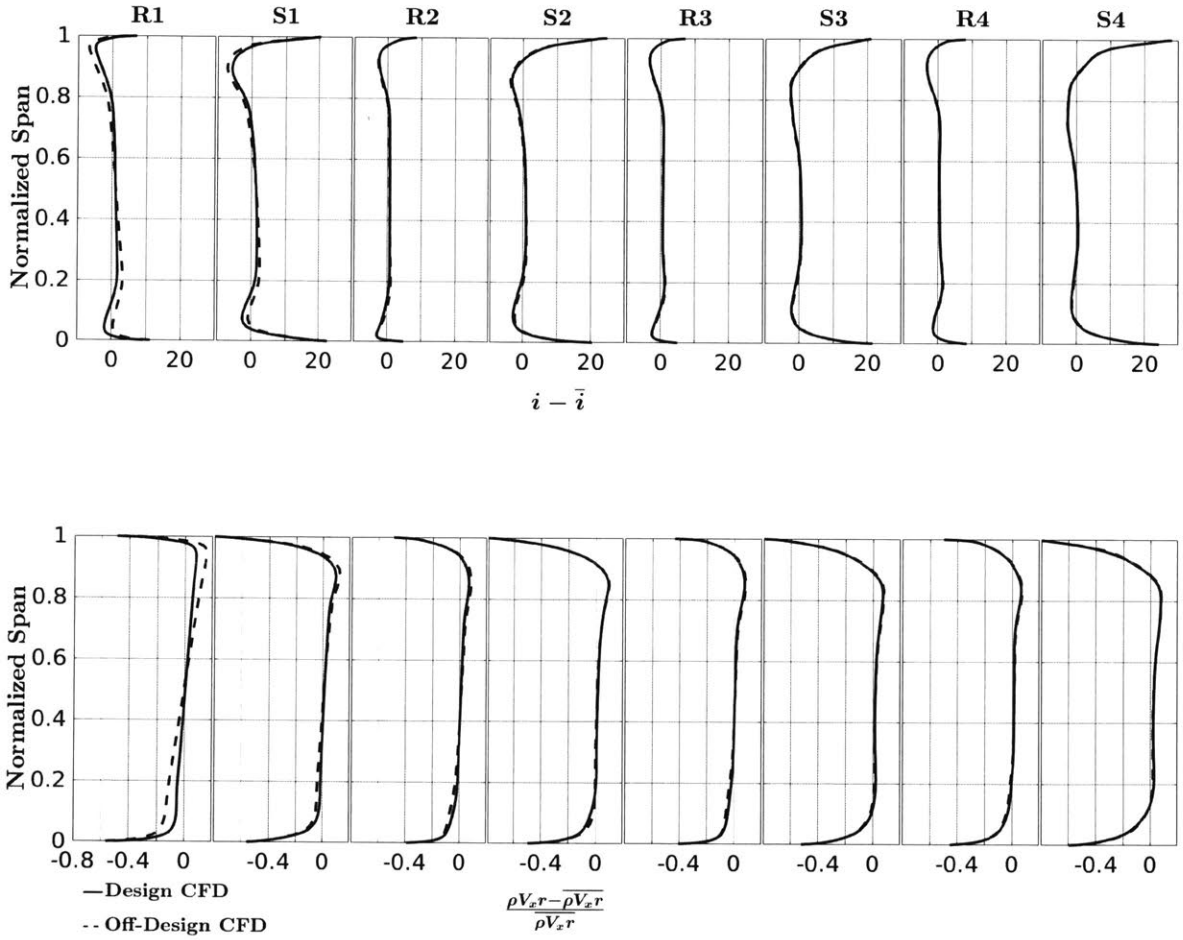

Figure 6-10: Inlet flow non-uniformity largely attenuated across first stage. Dashed profiles are off-design CFD results, solid profiles are design CFD results.

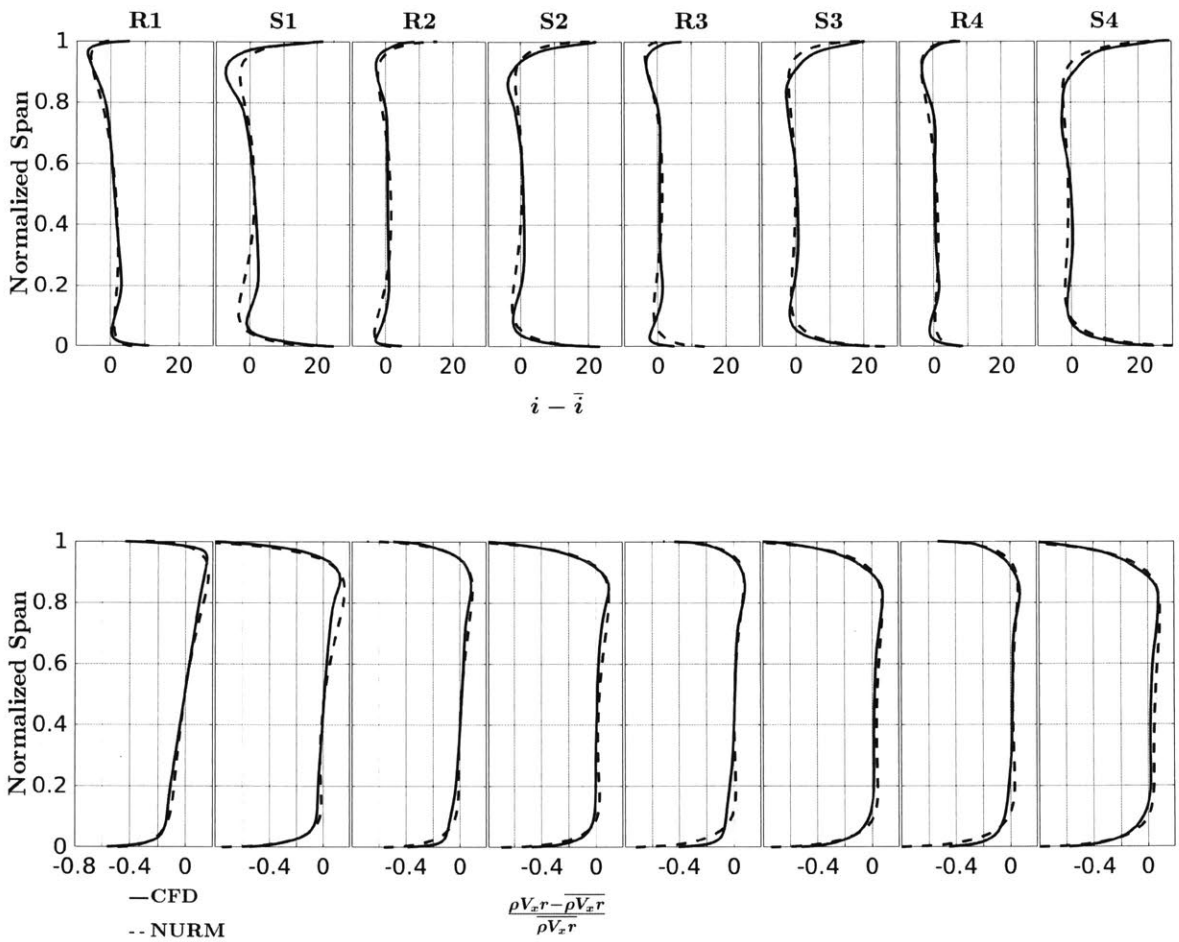

Figure 6-11: NURM captures non-uniformity attenuation. Dashed profiles are NURM estimations, solid profiles are CFD results.

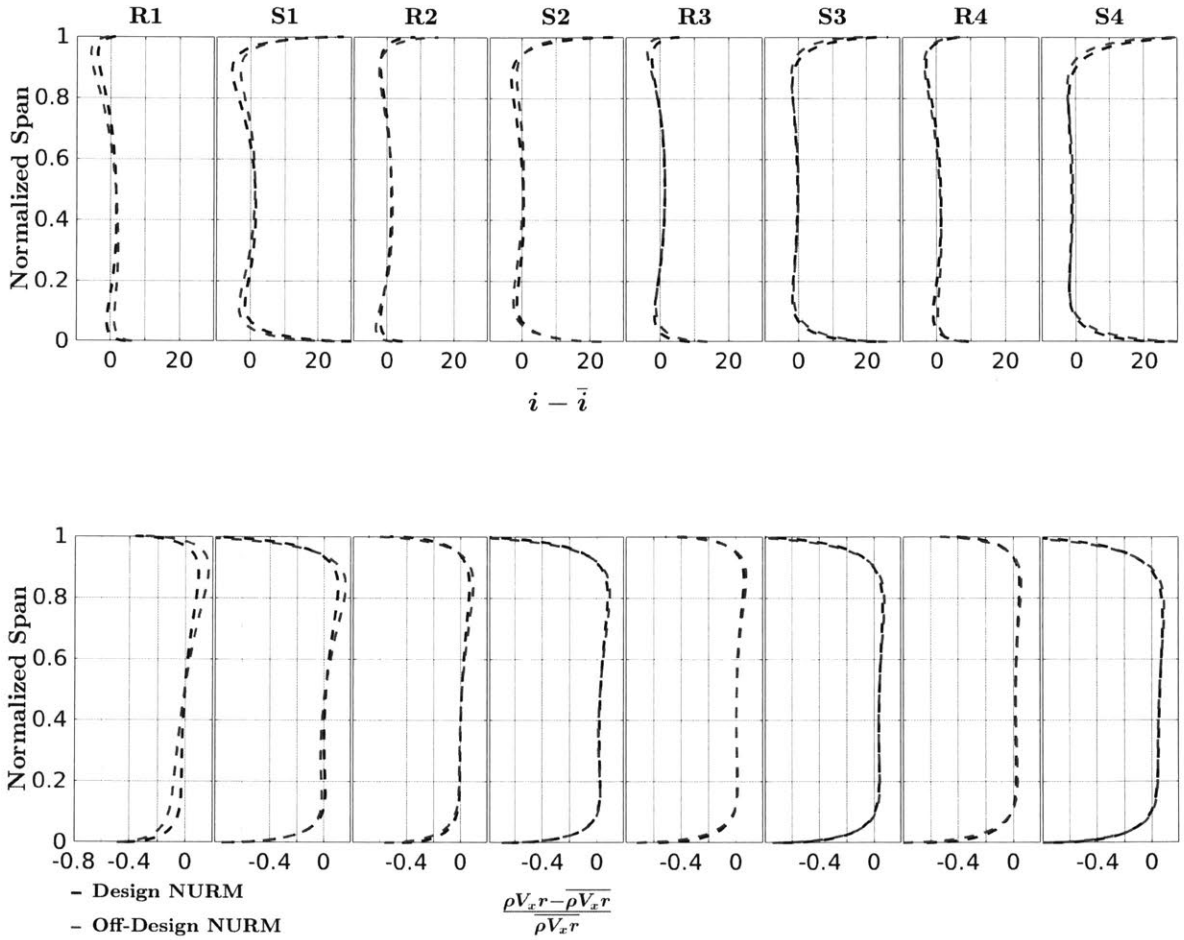

Figure 6-12: NURM captures trends in transfer of non-uniformity through compressor.

	$\pi - \pi_{datum}$	$\eta - \eta_{datum}$ [%]
CFD	-0.006	-0.07
NURM	-0.075	-0.2

Table 6.1: NURM method overestimates performance changes due to change in inlet flow non-uniformity.

6.4 Conclusions

The capabilities of the NURM method were demonstrated using three test cases. The capability of the method to capture the trends in both meanline compressor performance and non-uniformity through the compressor under datum conditions was confirmed by running the method across the test compressor operating map with datum rotor one inlet profiles. The capability of the method to estimate performance and non-uniformity for speeds at which CFD data is not available was confirmed by running the method across the 85% speed line. Finally, the capability of the method to capture the transfer of off-design rotor one inlet flow non-uniformity through the compressor was confirmed by running a test case with skewed rotor one inlet profiles.

These demonstrations show the basis function representation method and non-uniformity transfer functions effectively transfer non-uniformity through a compressor. Although the initial incorporation of these new capabilities into a meanline framework revealed several areas for improvement in implementation, the results show these non-uniformity representation and transfer methods are a suitable means of including radial flow non-uniformity in a 1D off-design performance estimation method for multistage axial compressors.

Chapter 7

Conclusions and Future Work

This thesis presented the incorporation of radial inlet flow non-uniformity and its impact on performance into a 1D off-design performance estimation method for multistage axial compressors. A new method for the representation of non-uniform radial flow profiles using a compact set of basis functions. Embedded stage CFD computations showed this representation method to be effective in reproducing the stage performance associated with the true profiles. Combinations of the basis functions were used to represent physical aspects of the profile. The link between non-uniformity and blade row performance was characterized using a sensitivity study performed on an embedded stage. The departure from datum non-uniformity was transferred across each blade row using transfer functions.

These new elements were incorporated into a legacy meanline framework to demonstrate the new capabilities. The demonstration showed the basis function representation and transfer function methods are effective means for incorporating radial flow non-uniformity into a 1D performance estimation method. The use of 3D CFD computations to characterize datum blade row performance, the transfer of non-uniformity, and its impact on performance brings high-fidelity 3D information into a 1D performance estimation method. The preliminary implementation also showed that these new methods for non-uniformity representation and transfer could be more effectively employed in a purpose-built performance estimation method than is possible in a traditional meanline framework.

The incorporation of radial flow non-uniformity and its impact on performance into a 1D performance estimation method, along with the use of 3D CFD results information could facilitate the high-fidelity estimation of off-design performance and stage matching earlier in the design process than is currently possible. This could enable designers to more effectively trade off-design and design point performance to improve overall performance depending on the operating environment. The radial flow profile data at each station also provides the possibility for future capabilities previously unavailable in 1D methods including stall point assessment on a blade row basis.

7.1 Future Work

The development and implementation of this method revealed several possible areas for improvement. A possible roadmap for the improvement and expansion of the NURM method is as follows:

The capabilities of the NURM method can be expanded to include the ability to estimate the performance of compressors of different geometries. This can be accomplished by incorporating the impact of changes in geometry on non-uniformity transfer. An embedded stage sensitivity study should be used to perform the characterization.

A new implementation should be developed for the calculation of blade row exit conditions, using the transfer of non-uniformity as an integral part of the calculation. This approach would eliminate the decoupling of non-uniformity from meanline conditions. The updated approach could use a different set of flow quantities to characterize the radial non-uniformity including total pressure to eliminate the need for a meanline loss coefficient. The use of different flow quantities would require additional sensitivity study computations to characterize the impact of total pressure non-uniformity on blade row performance. The set of flow quantities should be chosen such that all can be concurrently specified as inlet boundary conditions if the impact of variations in each is to be characterized independent of the others. The development of a new

method would also provide the opportunity to iterate in a non-dimensional quantity such as a Mach number rather than the current axial velocity.

Finally, the fidelity of the NURM method could be improved by running sensitivity studies for additional stages to incorporate the sensitivities for each blade row into the NURM method. This would also reveal any correlations in the sensitivities between blade rows. It is possible that correlations for the performance sensitivities of the different blade rows could eliminate the need for data from every blade row, simplifying the method.

Bibliography

[1] M.A. Gonzalez-Salazar, T. Kirsten, and L. Prchlik. Review of the operational flexibility and emissions of gas- and coal-fired power plants in a future with growing renewables. *Renewable and Sustainable Energy Reviews*, 82:1497–1512, February 2018.

[2] S. Venkataraman, G. Jordan, M. O'Connor, N. Kumar, S. Lefton, D. Lew, G. Brinkman, D. Palchak, and J. Cochran. Cost-benefit analysis of flexibility retrofits for coal and gas-fueled power plants. National renewable energy laboratory subcontract report, GE Energy, Intertek AIM, National Renewable Energy Laboratory, December 2013.

[3] B. Glensk, C. Rosen, R. Schiavo, S. Rabiee, R. Madlener, and R. De Doncker. Economic and technical evaluation of enhancing the flexibility of conventional power plants. E.on energy research center series, RWTH Aachen University, November 2015.

[4] H. Kiesow and G. McQuiggan. The challenges facing the utility gas turbine. In *Proceedings of GT2007, ASME Turbo Expo*. ASME, May 2007.

[5] S.J. Gallimore. Axial flow compressor design. In *Proc. Instn Mech Engrs Vol 213 Part C*, Special Issue on Turbomachinery Design, pages 437–449, 1999.

[6] W.H. Robbins and J.F. Dugan Jr. Prediction of off-design performance of multistage compressors. In *Aerodynamic Design of Axial-Flow Compressors*, pages 297–310. National Aeronautics and Space Administration, 1965.

[7] N.A. Cumpsty. *Compressor Aerodynamics*. Krieger, second edition, 2004.

[8] J. Bert. Application of a design optimization strategy to multi-stage compressor matching. Master's thesis, Massachusetts Institute of Technology, 2006.

[9] L.H. Smith. Casing boundary layers in multistage axial-flow compressors. In L.S. Dzung, editor, *Flow Research on Blading*, pages 275–304, Amsterdam, 1970. Elsevier.

[10] J.H. Horlock. The determination of end-wall blockage in axial compressors: A comparison between various approaches. *ASME J. Turbomachinery*, 122:218–224, April 2000.

[11] J. Dunham. A new endwall model for axial compressor throughflow calculations. *ASME J. Turbomachinery*, 117:533–540, October 1995.

[12] S.J. Gallimore. Viscous throughflow modeling of axial compressor bladerows using a tangential blade force hypothesis. *ASME J. Turbomachinery*, 120:662–670, October 1998.

[13] M.A. Howard and S.J Gallimore. Viscous throughflow modeling for multistage compressor design. *ASME J. Turbomachinery*, 115:296–304, April 1993.

[14] S.A. Khalid, A.S. Khalsa, I.A. Waitz, C.S. Tan, E.M. Greitzer, N.A. Cumpsty, J.J Adamczyk, and F.E. Marble. Endwall blockage in axial compressors. *ASME J. Turbomachinery*, 121:499–509, April 1999.

[15] S. Kulkarni. Development of a methodology to estimate aero-performance and aero-operability limits of a multistage axial flow compressor for use in preliminary design. Master's thesis, Case Western Reserve University, 2012.

[16] A. Joerger. Investigation of compressibility and flow non-uniformity effects on 1-d stage stacking. Master's thesis, Technical University of Munich, 2016.

[17] R. LaFleche. Personal Communication, Gas Turbine Lab, 2017.

[18] J.L. Kerrebrock. *Aircraft Engines and Gas Turbines.* MIT Press, second edition, 1992.

Appendix A

Stage Calculation

The calculations used in the NURM method to cross a blade row are detailed below for both rotors and stators. The meanline elements are adapted from Joerger [16]. The transfer of radial flow non-uniformity across each blade row and the inclusion of its impact on blade row performance are new additions. This was a first attempt at incorporating non-uniformity into a meanline method and the result is unnecessarily complicated and has many opportunities for improvement. For completeness and documentation of the results obtained thus far, this first attempt is described in detail below. The station definitions are shown in Figure A-1, and the velocity and angle conventions are shown in Figure A-2.

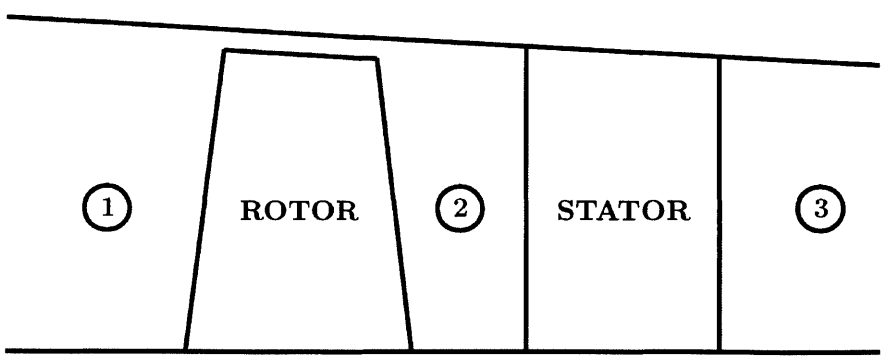

Figure A-1: Stations through stage denoted 1, 2, and 3.

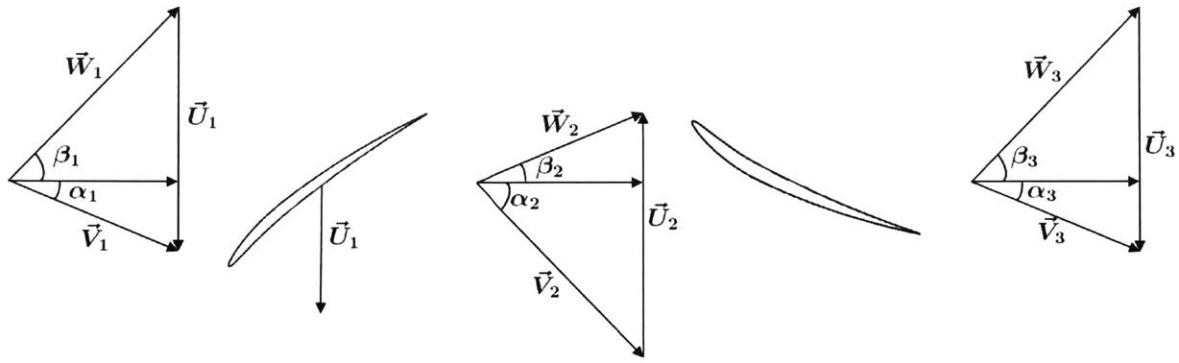

Figure A-2: Velocity and angle conventions.

A.1 Rotor Calculation

The required inputs to the method are the meanline values of stagnation pressure $P_{t,1}$, stagnation temperature $T_{t,1}$, absolute Mach number $M_{abs,1}$, and absolute flow angle α_1, the mass flow rate $\dot{m}$, and the shape parameters $n_{\rho V_x r,1}$, $\theta_{s,\rho V_x r,1}$, $\theta_{o,\rho V_x r,1}$, $\theta_{e,\rho V_x r,1}$, $n_{inc,1}$, $\theta_{s,inc,1}$, $\theta_{o,inc,1}$, and $\theta_{e,inc,1}$.

A.1.1 Upstream Meanline Conditions

First, the rotor inlet relative Mach number and incidence are computed so that the database representations can be used to determine the rotor performance, including the effects of inlet flow non-uniformity, and the non-uniformity transfer across the rotor. The static temperature T_1 is calculated from the stagnation temperature and Mach number using the isentropic relations:

$$T_1 = \frac{T_{t,1}}{1 + \frac{\gamma-1}{2} M_{abs,1}^2} \tag{A.1}$$

The static pressure can then be calculated from the stagnation-to-static temperature ratio and the stagnation pressure using isentropic relations.

$$P_1 = \frac{P_{t,1}}{\left(\frac{T_{t,1}}{T_1}\right)^{\frac{\gamma}{\gamma-1}}} \tag{A.2}$$

With the static temperature known, the sonic velocity and Mach number together

give the absolute velocity as $V_1 = M_{abs,1}\sqrt{\gamma RT_1}$, and with the absolute flow angle the axial velocity is given by $V_{x,1} = V_1 cos(\alpha_1)$. The flow coefficient is given by $\phi_1 = \frac{V_{x,1}}{U_1}$, where U_1 is the rotor blade speed, $\Omega r_{mean,1}$. Using the flow coefficient and absolute flow angle, the relative flow angle can be calculated as:

$$\beta_1 = atan\left(\frac{1 - \phi_1 tan(\alpha_1)}{\phi_1}\right) \tag{A.3}$$

The rotor incidence is then equal to the difference of the relative flow angle and the rotor inlet metal angle: $\bar{i}_{rotor} = \beta_1 - \chi_{inlet,rotor}$. The relative velocity magnitude can be calculated from the axial velocity, which is the same in both the absolute and relative reference frames, and the relative flow angle as $W_1 = \frac{V_{x,1}}{cos(\beta_1)}$, and finally the relative Mach number at the rotor inlet can be calculated from the relative velocity magnitude:

$$\overline{M}_{rel,1} = \frac{W_1}{\sqrt{\gamma RT_1}} \tag{A.4}$$

A.1.2 Datum Inlet Non-Uniformity and Non-Uniformity Transfer Across Rotor

With the incidence and relative Mach number known, the database representations can be used to determine the datum non-uniformity, non-uniformity transfer functions, datum blade row performance, and performance sensitivities. The datum shape parameters for the given operating point are:

$$
\begin{aligned}
n_{\rho V_x r,datum,1} &= n_{\rho V_x r,datum,1}(\bar{i}_{rotor}, \overline{M}_{rel,1}) \\
\theta_{s,\rho V_x r,datum,1} &= \theta_{s,\rho V_x r,datum,1}(\bar{i}_{rotor}, \overline{M}_{rel,1}) \\
\theta_{o,\rho V_x r,datum,1} &= \theta_{o,\rho V_x r,datum,1}(\bar{i}_{rotor}, \overline{M}_{rel,1}) \\
\theta_{e,\rho V_x r,datum,1} &= \theta_{e,\rho V_x r,datum,1}(\bar{i}_{rotor}, \overline{M}_{rel,1}) \\
n_{inc,datum,1} &= n_{inc,datum,1}(\bar{i}_{rotor}, \overline{M}_{rel,1}) \\
\theta_{s,inc,datum,1} &= \theta_{s,inc,datum,1}(\bar{i}_{rotor}, \overline{M}_{rel,1}) \\
\theta_{o,inc,datum,1} &= \theta_{o,inc,datum,1}(\bar{i}_{rotor}, \overline{M}_{rel,1}) \\
\theta_{e,inc,datum,1} &= \theta_{e,inc,datum,1}(\bar{i}_{rotor}, \overline{M}_{rel,1})
\end{aligned}
\tag{A.5}
$$

The difference between the datum shape parameters and the given inlet shape parameters can then be computed as:

$$
\begin{aligned}
(\Delta n_{\rho V_x r})_1 &= n_{\rho V_x r,1} - n_{\rho V_x r,datum,1} \\
(\Delta \theta_{s,\rho V_x r})_1 &= \theta_{s,\rho V_x r,1} - \theta_{s,\rho V_x r,datum,1} \\
(\Delta \theta_{o,\rho V_x r})_1 &= \theta_{o,\rho V_x r,1} - \theta_{o,\rho V_x r,datum,1} \\
(\Delta \theta_{e,\rho V_x r})_1 &= \theta_{e,\rho V_x r,1} - \theta_{e,\rho V_x r,datum,1} \\
(\Delta n_{inc})_1 &= n_{inc,1} - n_{inc,datum,1} \\
(\Delta \theta_{s,inc})_1 &= \theta_{s,inc,1} - \theta_{s,inc,datum,1} \\
(\Delta \theta_{o,inc})_1 &= \theta_{o,inc,1} - \theta_{o,inc,datum,1} \\
(\Delta \theta_{e,inc})_1 &= \theta_{e,inc,1} - \theta_{e,inc,datum,1}
\end{aligned}
\tag{A.6}
$$

The non-uniformity transfer functions are functionally dependent on the incidence, the relative Mach number, and the inlet departure from datum shape parameter:

$$
\begin{aligned}
k_{a,n,\rho V_x r,rotor} &= k_{a,n,\rho V_x r,rotor}(\bar{i}_{rotor}, \overline{M}_{rel,1}, (\Delta n_{\rho V_x r})_1) \\
k_{a,\theta_s,\rho V_x r,rotor} &= k_{a,\theta_s,\rho V_x r,rotor}(\bar{i}_{rotor}, \overline{M}_{rel,1}, (\Delta \theta_{s,\rho V_x r})_1) \\
k_{a,\theta_o,\rho V_x r,rotor} &= k_{a,\theta_o,\rho V_x r,rotor}(\bar{i}_{rotor}, \overline{M}_{rel,1}, (\Delta \theta_{o,\rho V_x r})_1) \\
k_{a,\theta_e,\rho V_x r,rotor} &= k_{a,\theta_e,\rho V_x r,rotor}(\bar{i}_{rotor}, \overline{M}_{rel,1}, (\Delta \theta_{e,\rho V_x r})_1) \\
k_{a,n,inc,rotor} &= k_{a,n,inc,rotor}(\bar{i}_{rotor}, \overline{M}_{rel,1}, (\Delta n_{inc})_1) \\
k_{a,\theta_s,inc,rotor} &= k_{a,\theta_s,inc,rotor}(\bar{i}_{rotor}, \overline{M}_{rel,1}, (\Delta \theta_{s,inc})_1) \\
k_{a,\theta_o,inc,rotor} &= k_{a,\theta_o,inc,rotor}(\bar{i}_{rotor}, \overline{M}_{rel,1}, (\Delta \theta_{o,inc})_1) \\
k_{a,\theta_e,inc,rotor} &= k_{a,\theta_e,inc,rotor}(\bar{i}_{rotor}, \overline{M}_{rel,1}, (\Delta \theta_{e,inc})_1)
\end{aligned}
\tag{A.7}
$$

A.1.3 Rotor Performance with Impact of Inlet Flow Non-Uniformity

The datum stagnation pressure loss coefficient and deviation angle are determined as:

$$
\overline{\omega}_{rotor} = \overline{\omega}_{rotor}(\bar{i}_{rotor}, \overline{M}_{rel,1}), \quad \overline{\delta}_{rotor} = \overline{\delta}_{rotor}(\bar{i}_{rotor}, \overline{M}_{rel,1}) \tag{A.8}
$$

The relative Mach number and incidence are also used with the performance sensitivity databases to determine the partial derivatives which are then used to alter the blade row performance. Sensitivities are obtained for loss coefficient, deviation angle, and station 2 blockage factor with respect to each of the shape parameters of the station 1 $\rho V_x r$ and incidence profiles.

$$
\begin{aligned}
\frac{\partial \overline{\omega}_{rotor}}{\partial n_{\rho V_x r,1}} &= \frac{\partial \overline{\omega}_{rotor}}{\partial n_{\rho V_x r,1}}(\bar{i}_{rotor}, \overline{M}_{rel,1}) \\
\frac{\partial \overline{\omega}_{rotor}}{\partial \theta_{s,\rho V_x r,1}} &= \frac{\partial \overline{\omega}_{rotor}}{\partial \theta_{s,\rho V_x r,1}}(\bar{i}_{rotor}, \overline{M}_{rel,1}) \\
\frac{\partial \overline{\omega}_{rotor}}{\partial \theta_{o,\rho V_x r,1}} &= \frac{\partial \overline{\omega}_{rotor}}{\partial \theta_{o,\rho V_x r,1}}(\bar{i}_{rotor}, \overline{M}_{rel,1}) \\
\frac{\partial \overline{\omega}_{rotor}}{\partial \theta_{e,\rho V_x r,1}} &= \frac{\partial \overline{\omega}_{rotor}}{\partial \theta_{e,\rho V_x r,1}}(\bar{i}_{rotor}, \overline{M}_{rel,1})
\end{aligned}
\tag{A.9}
$$

$$
\begin{aligned}
\frac{\partial \overline{\omega}_{rotor}}{\partial n_{inc,1}} &= \frac{\partial \overline{\omega}_{rotor}}{\partial n_{inc,1}}(\bar{i}_{rotor}, \overline{M}_{rel,1}) \\
\frac{\partial \overline{\omega}_{rotor}}{\partial \theta_{s,inc,1}} &= \frac{\partial \overline{\omega}_{rotor}}{\partial \theta_{s,inc,1}}(\bar{i}_{rotor}, \overline{M}_{rel,1}) \\
\frac{\partial \overline{\omega}_{rotor}}{\partial \theta_{o,inc,1}} &= \frac{\partial \overline{\omega}_{rotor}}{\partial \theta_{o,inc,1}}(\bar{i}_{rotor}, \overline{M}_{rel,1}) \\
\frac{\partial \overline{\omega}_{rotor}}{\partial \theta_{e,inc,1}} &= \frac{\partial \overline{\omega}_{rotor}}{\partial \theta_{e,inc,1}}(\bar{i}_{rotor}, \overline{M}_{rel,1})
\end{aligned}
\tag{A.10}
$$

$$
\begin{aligned}
\frac{\partial \overline{\delta}_{rotor}}{\partial n_{\rho V_x r,1}} &= \frac{\partial \overline{\delta}_{rotor}}{\partial n_{\rho V_x r,1}}(\bar{i}_{rotor}, \overline{M}_{rel,1}) \\
\frac{\partial \overline{\delta}_{rotor}}{\partial \theta_{s,\rho V_x r,1}} &= \frac{\partial \overline{\delta}_{rotor}}{\partial \theta_{s,\rho V_x r,1}}(\bar{i}_{rotor}, \overline{M}_{rel,1}) \\
\frac{\partial \overline{\delta}_{rotor}}{\partial \theta_{o,\rho V_x r,1}} &= \frac{\partial \overline{\delta}_{rotor}}{\partial \theta_{o,\rho V_x r,1}}(\bar{i}_{rotor}, \overline{M}_{rel,1}) \\
\frac{\partial \overline{\delta}_{rotor}}{\partial \theta_{e,\rho V_x r,1}} &= \frac{\partial \overline{\delta}_{rotor}}{\partial \theta_{e,\rho V_x r,1}}(\bar{i}_{rotor}, \overline{M}_{rel,1})
\end{aligned}
\tag{A.11}
$$

$$
\begin{aligned}
\frac{\partial \overline{\delta}_{rotor}}{\partial n_{inc,1}} &= \frac{\partial \overline{\delta}_{rotor}}{\partial n_{inc,1}}(\bar{i}_{rotor}, \overline{M}_{rel,1}) \\
\frac{\partial \overline{\delta}_{rotor}}{\partial \theta_{s,inc,1}} &= \frac{\partial \overline{\delta}_{rotor}}{\partial \theta_{s,inc,1}}(\bar{i}_{rotor}, \overline{M}_{rel,1}) \\
\frac{\partial \overline{\delta}_{rotor}}{\partial \theta_{o,inc,1}} &= \frac{\partial \overline{\delta}_{rotor}}{\partial \theta_{o,inc,1}}(\bar{i}_{rotor}, \overline{M}_{rel,1}) \\
\frac{\partial \overline{\delta}_{rotor}}{\partial \theta_{e,inc,1}} &= \frac{\partial \overline{\delta}_{rotor}}{\partial \theta_{e,inc,1}}(\bar{i}_{rotor}, \overline{M}_{rel,1})
\end{aligned}
\tag{A.12}
$$

$$
\begin{aligned}
\frac{\partial k_{b,2}}{\partial n_{\rho V_x r,1}} &= \frac{\partial k_{b,2}}{\partial n_{\rho V_x r,1}}(\bar{i}_{rotor}, \overline{M}_{rel,1}) \\
\frac{\partial k_{b,2}}{\partial \theta_{s,\rho V_x r,1}} &= \frac{\partial k_{b,2}}{\partial \theta_{s,\rho V_x r,1}}(\bar{i}_{rotor}, \overline{M}_{rel,1}) \\
\frac{\partial k_{b,2}}{\partial \theta_{o,\rho V_x r,1}} &= \frac{\partial k_{b,2}}{\partial \theta_{o,\rho V_x r,1}}(\bar{i}_{rotor}, \overline{M}_{rel,1}) \\
\frac{\partial k_{b,2}}{\partial \theta_{e,\rho V_x r,1}} &= \frac{\partial k_{b,2}}{\partial \theta_{e,\rho V_x r,1}}(\bar{i}_{rotor}, \overline{M}_{rel,1})
\end{aligned}
\tag{A.13}
$$

$$
\begin{aligned}
\frac{\partial k_{b,2}}{\partial n_{inc,1}} &= \frac{\partial k_{b,2}}{\partial n_{inc,1}}(\bar{i}_{rotor}, \overline{M}_{rel,1}) \\
\frac{\partial k_{b,2}}{\partial \theta_{s,inc,1}} &= \frac{\partial k_{b,2}}{\partial \theta_{s,inc,1}}(\bar{i}_{rotor}, \overline{M}_{rel,1}) \\
\frac{\partial k_{b,2}}{\partial \theta_{o,inc,1}} &= \frac{\partial k_{b,2}}{\partial \theta_{o,inc,1}}(\bar{i}_{rotor}, \overline{M}_{rel,1}) \\
\frac{\partial k_{b,2}}{\partial \theta_{e,inc,1}} &= \frac{\partial k_{b,2}}{\partial \theta_{e,inc,1}}(\bar{i}_{rotor}, \overline{M}_{rel,1})
\end{aligned}
\tag{A.14}
$$

The rotor loss coefficient and deviation angle are then altered as:

$$
\begin{aligned}
\overline{\omega}_{rotor,altered} = \overline{\omega}_{rotor} + & \frac{\partial \overline{\omega}_{rotor}}{\partial n_{\rho V_x r,1}}(\Delta n_{\rho V_x r})_1 + \frac{\partial \overline{\omega}_{rotor}}{\partial \theta_{s,\rho V_x r,1}}(\Delta \theta_{s,\rho V_x r})_1 + \\
& \frac{\partial \overline{\omega}_{rotor}}{\partial \theta_{o,\rho V_x r,1}}(\Delta \theta_{o,\rho V_x r})_1 + \frac{\partial \overline{\omega}_{rotor}}{\partial \theta_{e,\rho V_x r,1}}(\Delta \theta_{e,\rho V_x r})_1 + \\
& \frac{\partial \overline{\omega}_{rotor}}{\partial n_{inc,1}}(\Delta n_{inc})_1 + \frac{\partial \overline{\omega}_{rotor}}{\partial \theta_{s,inc,1}}(\Delta \theta_{s,inc})_1 + \\
& \frac{\partial \overline{\omega}_{rotor}}{\partial \theta_{o,inc,1}}(\Delta \theta_{o,inc})_1 + \frac{\partial \overline{\omega}_{rotor}}{\partial \theta_{e,inc,1}}(\Delta \theta_{e,inc})_1
\end{aligned}
\tag{A.15}
$$

$$
\begin{aligned}
\overline{\delta}_{rotor,altered} = \overline{\delta}_{rotor} + & \frac{\partial \overline{\delta}_{rotor}}{\partial n_{\rho V_x r,1}}(\Delta n_{\rho V_x r})_1 + \frac{\partial \overline{\delta}_{rotor}}{\partial \theta_{s,\rho V_x r,1}}(\Delta \theta_{s,\rho V_x r})_1 + \\
& \frac{\partial \overline{\delta}_{rotor}}{\partial \theta_{o,\rho V_x r,1}}(\Delta \theta_{o,\rho V_x r})_1 + \frac{\partial \overline{\delta}_{rotor}}{\partial \theta_{e,\rho V_x r,1}}(\Delta \theta_{e,\rho V_x r})_1 + \\
& \frac{\partial \overline{\delta}_{rotor}}{\partial n_{inc,1}}(\Delta n_{inc})_1 + \frac{\partial \overline{\delta}_{rotor}}{\partial \theta_{s,inc,1}}(\Delta \theta_{s,inc})_1 + \\
& \frac{\partial \overline{\delta}_{rotor}}{\partial \theta_{o,inc,1}}(\Delta \theta_{o,inc})_1 + \frac{\partial \overline{\delta}_{rotor}}{\partial \theta_{e,inc,1}}(\Delta \theta_{e,inc})_1
\end{aligned}
\tag{A.16}
$$

The blockage is not yet known because the rotor outlet blockage is set by the rotor outlet conditions which are not yet known. The blockage will be altered for the impact of rotor inlet radial flow non-uniformity inside the iteration loop used to determine the rotor outlet conditions.

A.1.4 Station 2 Relative Stagnation Conditions and Relative Flow Angle

With the altered rotor loss and deviation the rotor outlet relative stagnation pressure and temperature can be calculated. By conservation of rothalpy, given in Equation A.17, the relative stagnation enthalpy across the blade row will only change if there are changes in streamtube radius, here approximated using meanline radius.

$$h_{t,rel,1} - \frac{U_1^2}{2} = h_{t,rel,2} - \frac{U_2^2}{2} \tag{A.17}$$

This allows for the calculation of the relative stagnation enthalpy at station 2, and thus the relative stagnation temperature at station 2, using the known geometry and inlet conditions:

$$h_{t,rel,1} = \frac{\gamma R}{\gamma - 1} T_{t,1} - \frac{V_1^2}{2} + \frac{W_1^2}{2} \tag{A.18}$$

$$U_2 = \Omega r_{mean,2} \tag{A.19}$$

$$h_{t,rel,2} = h_{t,rel,1} + \frac{U_2^2 - U_1^2}{2} \tag{A.20}$$

$$T_{t,rel,2} = \frac{h_{t,rel,2}}{\frac{\gamma R}{\gamma - 1}} \tag{A.21}$$

The stagnation pressure loss coefficient in the relative reference frame is used to determine the relative stagnation pressure at station 2.

$$T_{t,rel,1} = \frac{h_{t,rel,1}}{\frac{\gamma R}{\gamma - 1}} \tag{A.22}$$

$$P_{t,rel,1} = P_1 \left(\frac{T_{t,rel,1}}{T_1} \right)^{\left(\frac{\gamma}{\gamma - 1}\right)} \tag{A.23}$$

$$P_{t,rel,2,isen} = P_{t,rel,1}\left(\frac{T_{t,rel,2}}{T_{t,rel,1}}\right)^{(\frac{\gamma}{\gamma-1})} \tag{A.24}$$

$$P_{t,rel,2} = P_{t,rel,2} - \overline{\omega}_{rotor,altered}(P_{t,rel,1} - P_1) \tag{A.25}$$

The relative flow angle at station 2 is set by the rotor deviation, altered for the impact of inlet flow non-uniformity, and the rotor outlet blade metal angle as $\beta_2 = \chi_{outlet,rotor} + \overline{\delta}_{rotor,altered}$.

A.1.5 Iteration Loop for Station 2 Blockage

The blockage at each station in the compressor is a function of the relative Mach number and incidence at that station. This means that the blockage at station 2 is determined by the station 2 relative Mach number and incidence. However, the relative Mach number and incidence at station 2 depend on the station 2 blockage, requiring an iteration loop. An initial guess of the axial velocity $V_{x,2}$ is made, and the calculation of the conditions at station 2 is carried out. The blockage is determined from the polynomial surface fit of the station 2 blockage database. Because station 2 is the stator inlet the relative and absolute frames are the same and the absolute and relative Mach numbers are equal. This blockage is used along with the computed station 2 stagnation pressure, stagnation temperature, and flow angle to calculate $V_{x,2}$. If the initial guess of $V_{x,2}$ is not equal to the calculated $V_{x,2}$, the process is repeated with an updated initial guess until the values converge. In addition to the station 2 incidence and Mach number, the absolute stagnation temperature and pressure must be determined to serve as inputs to the downstream stator.

First, the relative Mach number is calculated from the relative stagnation temperature, axial velocity guess, and relative flow angle:

$$M_{rel,2} = \sqrt{\frac{1}{\frac{\gamma R T_{t,rel,2}}{V_{x,2}^2(1+tan^2(\beta_2))} - \frac{\gamma-1}{2}}} \tag{A.26}$$

With the relative Mach number known the static temperature can be determined:

$$T_2 = \frac{T_{t,rel,2}}{1 + \frac{\gamma-1}{2} M_{rel,2}^2} \tag{A.27}$$

The magnitude of the relative velocity is given by the axial velocity and relative flow angle, and then the velocity triangles give the magnitude of the absolute velocity:

$$W_2 = \frac{V_{x,2}}{cos(\beta_2)} \tag{A.28}$$

$$V_2 = \sqrt{V_{x,2}^2 + (U_2 - W_2 sin(\beta_2))^2} \tag{A.29}$$

The absolute stagnation temperature at station 2 is calculated using the absolute stagnation enthalpy:

$$h_2 = \frac{\gamma R}{\gamma - 1} T_2 \tag{A.30}$$

$$h_{t,2} = h_2 + \frac{V_2^2}{2} \tag{A.31}$$

$$T_{t,2} = \frac{h_{t,2}}{\frac{\gamma R}{\gamma-1}} \tag{A.32}$$

The static pressure is determined using the relative stagnation pressure, relative stagnation temperature and static temperature through the isentropic relations:

$$P_2 = \frac{P_{t,rel,2}}{\left(\frac{T_{t,rel,2}}{T_2}\right)^{\frac{\gamma}{\gamma-1}}} \tag{A.33}$$

With static pressure known the absolute stagnation pressure is calculated using isentropic relations:

$$P_{t,2} = P_2 \left(\frac{T_{t,2}}{T_2}\right)^{\frac{\gamma}{\gamma-1}} \tag{A.34}$$

The absolute Mach number is determined from the absolute stagnation temperature and static temperature through the isentropic relations:

$$\overline{M_{abs,2}} = \sqrt{\frac{2}{\gamma - 1}\left(\frac{T_{t,2}}{T_2} - 1\right)} \tag{A.35}$$

The absolute flow angle is the inverse cosine of the axial velocity and velocity magnitude, $\alpha_2 = acos(\frac{V_{x,2}}{V_2})$, and with the absolute flow angle and the known stator inlet metal angle the stator meanline incidence is given by $\bar{i}_{stator} = \alpha_2 - \chi_{inlet,stator}$.

The station 2 blockage can now be extracted from the database as $k_{b,2} = k_{b,2}(\bar{i}_{stator}, \overline{M}_{rel,2})$, where because station 2 is a stator inlet, $\overline{M}_{rel,2} = \overline{M}_{abs,2}$. The impact of station 1 flow non-uniformity on station 2 blockage is accounted for using the partial derivatives:

$$\begin{aligned} k_{b,2,altered} = k_{b,2} + & \frac{\partial k_{b,2}}{\partial n_{\rho V_x r,1}}(\Delta n_{\rho V_x r})_1 + \frac{\partial k_{b,2}}{\partial \theta_{s,\rho V_x r,1}}(\Delta \theta_{s,\rho V_x r})_1 + \frac{\partial k_{b,2}}{\partial \theta_{o,\rho V_x r,1}}(\Delta \theta_{o,\rho V_x r})_1 + \\ & \frac{\partial k_{b,2}}{\partial \theta_{e,\rho V_x r,1}}(\Delta \theta_{e,\rho V_x r})_1 + \frac{\partial k_{b,2}}{\partial n_{inc,1}}(\Delta n_{inc})_1 + \frac{\partial k_{b,2}}{\partial \theta_{s,inc,1}}(\Delta \theta_{s,inc})_1 + \\ & \frac{\partial k_{b,2}}{\partial \theta_{o,inc,1}}(\Delta \theta_{o,inc})_1 + \frac{\partial k_{b,2}}{\partial \theta_{e,inc,1}}(\Delta \theta_{e,inc})_1 \end{aligned} \tag{A.36}$$

Through a combination of conservation of rothalpy, the ideal gas law, the definitions of loss coefficient, deviation, relative Mach number and mass flow rate per unit span, isentropic relations and velocity triangles, an implicit equation for $V_{x,2}$ can be obtained in terms of known quantities:

$$V_{x,2} = \frac{(\overline{\rho V_x r})_2 R T_{t,rel,2}\left(1 + \frac{\gamma-1}{2}\left(\frac{1}{\frac{\gamma R T_{t,rel,2}}{V_{x,2}^2(1+tan^2(\beta_2))} - \frac{\gamma-1}{2}}\right)\right)^{\frac{1}{\gamma-1}}}{P_{t,rel,2} r_{mean,2}} \tag{A.37}$$

The meanline mass flow rate per unit span, $\overline{\rho V_x r}$, is required to solve this equation. In this implementation of the NURM framework, this quantity was calculated from Kulkarni's blockage factor because the non-uniformity of the profiles and their meanline values were decoupled. However, it could improve the method to compute dimensional radial flow profiles and then take a mass average $\rho V_x r$ to use as $(\overline{\rho V_x r})$. The effective area represents the area that satisfies the corrected flow per unit area

equation on an average basis, and the corrected flow per unit area equation is equivalent to the definition of mass flow rate, $\dot{m} = \rho V_x A$. Thus the effective area can be expressed as:

$$A_{eff} = \frac{\dot{m}}{\overline{\rho V_x}} \tag{A.38}$$

So Kulkarni's blockage factor can be rewritten as:

$$k_b = 1 - \frac{A_{eff}}{A_{annulus}} = 1 - \frac{\frac{\dot{m}}{\overline{\rho V_x}}}{A_{annulus}} \tag{A.39}$$

And $A_{annulus} = \pi(r_{max}^2 - r_{min}^2) = \pi(r_{max} + r_{min})(r_{max} - r_{min})$ so:

$$k_b = 1 - \frac{\frac{\dot{m}}{\overline{\rho V_x}}}{\pi(r_{max} + r_{min})(r_{max} - r_{min})} \tag{A.40}$$

This is equivalent to:

$$\overline{\rho V_x} = \frac{\dot{m}}{(1 - k_b)\pi(r_{max} + r_{min})(r_{max} - r_{min})} \tag{A.41}$$

If $\overline{r}$ is taken to be $r_{mean} = \frac{r_{max}+r_{min}}{2}$, then:

$$\overline{\rho V_x r} = \frac{\dot{m}}{2\pi(1 - k_b)(r_{max} - r_{min})} \tag{A.42}$$

Equation A.37 is solved for $V_{x,2}$ using $(\overline{\rho V_x r})_2$ calculated from $k_{b,2,altered}$. If this $V_{x,2}$ value does not match the initial guess, the process is repeated using an updated initial guess until the values converge. Once the loop converges, all values necessary for the stator calculation are known.

A.2 Stator Calculation

A.2.1 Station 2 Non-Uniformity and Non-Uniformity Transfer Across Stator

The stator inlet datum shape parameters can be determined from their respective database representations using the stator incidence and stator inlet Mach number, where in the stator frame of reference the relative and absolute Mach numbers are equal:

$$\begin{aligned}
n_{\rho V_x r,datum,2} &= n_{\rho V_x r,datum,2}(\bar{i}_{stator}, \overline{M}_{abs,2}) \\
\theta_{s,\rho V_x r,datum,2} &= \theta_{s,\rho V_x r,datum,2}(\bar{i}_{stator}, \overline{M}_{abs,2}) \\
\theta_{o,\rho V_x r,datum,2} &= \theta_{o,\rho V_x r,datum,2}(\bar{i}_{stator}, \overline{M}_{abs,2}) \\
\theta_{e,\rho V_x r,datum,2} &= \theta_{e,\rho V_x r,datum,2}(\bar{i}_{stator}, \overline{M}_{abs,2}) \\
n_{inc,datum,2} &= n_{inc,datum,2}(\bar{i}_{stator}, \overline{M}_{abs,2}) \\
\theta_{s,inc,datum,2} &= \theta_{s,inc,datum,2}(\bar{i}_{stator}, \overline{M}_{abs,2}) \\
\theta_{o,inc,datum,2} &= \theta_{o,inc,datum,2}(\bar{i}_{stator}, \overline{M}_{abs,2}) \\
\theta_{e,inc,datum,2} &= \theta_{e,inc,datum,2}(\bar{i}_{stator}, \overline{M}_{abs,2})
\end{aligned} \tag{A.43}$$

The stator inlet shape parameters are then the sum of the datum shape parameters and the departures from datum known from above:

$$\begin{aligned}
n_{\rho V_x r,2} &= n_{\rho V_x r,datum,2} + (\Delta n_{\rho V_x r})_2 \\
\theta_{s,\rho V_x r,2} &= \theta_{s,\rho V_x r,datum,2} + (\Delta \theta_{s,\rho V_x r})_2 \\
\theta_{o,\rho V_x r,2} &= \theta_{o,\rho V_x r,datum,2} + (\Delta \theta_{o,\rho V_x r})_2 \\
\theta_{e,\rho V_x r,2} &= \theta_{e,\rho V_x r,datum,2} + (\Delta \theta_{e,\rho V_x r})_2 \\
n_{inc,2} &= n_{inc,datum,2} + (\Delta n_{inc})_2 \\
\theta_{s,inc,2} &= \theta_{s,inc,datum,2} + (\Delta \theta_{s,inc})_2 \\
\theta_{o,inc,2} &= \theta_{o,inc,datum,2} + (\Delta \theta_{o,inc})_2 \\
\theta_{e,inc,2} &= \theta_{e,inc,datum,2} + (\Delta \theta_{e,inc})_2
\end{aligned} \tag{A.44}$$

The stator non-uniformity transfer functions are determined from database representations using the stator incidence and $M_{abs,2}$:

$$
\begin{aligned}
k_{a,n,\rho V_x r,stator} &= k_{a,n,\rho V_x r,stator}(\bar{i}_{stator}, \overline{M}_{abs,2}, (\Delta n_{\rho V_x r})_2) \\
k_{a,\theta_s,\rho V_x r,stator} &= k_{a,\theta_s,\rho V_x r,stator}(\bar{i}_{stator}, \overline{M}_{abs,2}, (\Delta \theta_{s,\rho V_x r})_2) \\
k_{a,\theta_o,\rho V_x r,stator} &= k_{a,\theta_o,\rho V_x r,stator}(\bar{i}_{stator}, \overline{M}_{abs,2}, (\Delta \theta_{o,\rho V_x r})_2) \\
k_{a,\theta_e,\rho V_x r,stator} &= k_{a,\theta_e,\rho V_x r,stator}(\bar{i}_{stator}, \overline{M}_{abs,2}, (\Delta \theta_{e,\rho V_x r})_2) \\
k_{a,n,inc,stator} &= k_{a,n,inc,stator}(\bar{i}_{stator}, \overline{M}_{abs,2}, (\Delta n_{inc})_2) \\
k_{a,\theta_s,inc,stator} &= k_{a,\theta_s,inc,stator}(\bar{i}_{stator}, \overline{M}_{abs,2}, (\Delta \theta_{s,inc})_2) \\
k_{a,\theta_o,inc,stator} &= k_{a,\theta_o,inc,stator}(\bar{i}_{stator}, \overline{M}_{abs,2}, (\Delta \theta_{o,inc})_2) \\
k_{a,\theta_e,inc,stator} &= k_{a,\theta_e,inc,stator}(\bar{i}_{stator}, \overline{M}_{abs,2}, (\Delta \theta_{e,inc})_2)
\end{aligned}
\tag{A.45}
$$

The transfer functions and the $\Delta(SH)$ at station 2 are used to calculate the $\Delta(SH)$ at station 3:

$$
\begin{aligned}
(\Delta n_{\rho V_x r})_3 &= k_{a,n,\rho V_x r,stator}(\Delta n_{\rho V_x r})_2 \\
(\Delta \theta_{s,\rho V_x r})_3 &= k_{a,\theta_s,\rho V_x r,stator}(\Delta \theta_{s,\rho V_x r})_2 \\
(\Delta \theta_{o,\rho V_x r})_3 &= k_{a,\theta_o,\rho V_x r,stator}(\Delta \theta_{o,\rho V_x r})_2 \\
(\Delta \theta_{e,\rho V_x r})_3 &= k_{a,\theta_e,\rho V_x r,stator}(\Delta \theta_{e,\rho V_x r})_2 \\
(\Delta n_{inc})_3 &= k_{a,n,inc,stator}(\Delta n_{inc})_2 \\
(\Delta \theta_{s,inc})_3 &= k_{a,\theta_s,inc,stator}(\Delta \theta_{s,inc})_2 \\
(\Delta \theta_{o,inc})_3 &= k_{a,\theta_o,inc,stator}(\Delta \theta_{o,inc})_2 \\
(\Delta \theta_{e,inc})_3 &= k_{a,\theta_e,inc,stator}(\Delta \theta_{e,inc})_2
\end{aligned}
\tag{A.46}
$$

A.2.2 Stator Performance with Impact of Inlet Flow Non-Uniformity

The stator loss coefficient and deviation angle are calculated from the databases as are the performance sensitivities:

$$\overline{\omega}_{stator} = \overline{\omega}_{stator}(\bar{i}_{stator}, \overline{M}_{abs,2}), \quad \overline{\delta}_{stator} = \overline{\delta}_{stator}(\bar{i}_{stator}, \overline{M}_{abs,2}) \tag{A.47}$$

$$\begin{aligned}
\frac{\partial \overline{\omega}_{stator}}{\partial n_{\rho V_x r,2}} &= \frac{\partial \overline{\omega}_{stator}}{\partial n_{\rho V_x r,2}}(\bar{i}_{stator}, \overline{M}_{abs,2}) \\
\frac{\partial \overline{\omega}_{stator}}{\partial \theta_{s,\rho V_x r,2}} &= \frac{\partial \overline{\omega}_{stator}}{\partial \theta_{s,\rho V_x r,2}}(\bar{i}_{stator}, \overline{M}_{abs,2}) \\
\frac{\partial \overline{\omega}_{stator}}{\partial \theta_{o,\rho V_x r,2}} &= \frac{\partial \overline{\omega}_{stator}}{\partial \theta_{o,\rho V_x r,2}}(\bar{i}_{stator}, \overline{M}_{abs,2}) \\
\frac{\partial \overline{\omega}_{stator}}{\partial \theta_{e,\rho V_x r,2}} &= \frac{\partial \overline{\omega}_{stator}}{\partial \theta_{e,\rho V_x r,2}}(\bar{i}_{stator}, \overline{M}_{abs,2})
\end{aligned} \tag{A.48}$$

$$\begin{aligned}
\frac{\partial \overline{\omega}_{stator}}{\partial n_{inc,2}} &= \frac{\partial \overline{\omega}_{stator}}{\partial n_{inc,2}}(\bar{i}_{stator}, \overline{M}_{abs,2}) \\
\frac{\partial \overline{\omega}_{stator}}{\partial \theta_{s,inc,2}} &= \frac{\partial \overline{\omega}_{stator}}{\partial \theta_{s,inc,2}}(\bar{i}_{stator}, \overline{M}_{abs,2}) \\
\frac{\partial \overline{\omega}_{stator}}{\partial \theta_{o,inc,2}} &= \frac{\partial \overline{\omega}_{stator}}{\partial \theta_{o,inc,2}}(\bar{i}_{stator}, \overline{M}_{abs,2}) \\
\frac{\partial \overline{\omega}_{stator}}{\partial \theta_{e,inc,2}} &= \frac{\partial \overline{\omega}_{stator}}{\partial \theta_{e,inc,2}}(\bar{i}_{stator}, \overline{M}_{abs,2})
\end{aligned} \tag{A.49}$$

$$\begin{aligned}
\frac{\partial \overline{\delta}_{stator}}{\partial n_{\rho V_x r,2}} &= \frac{\partial \overline{\delta}_{stator}}{\partial n_{\rho V_x r,2}}(\bar{i}_{stator}, \overline{M}_{abs,2}) \\
\frac{\partial \overline{\delta}_{stator}}{\partial \theta_{s,\rho V_x r,2}} &= \frac{\partial \overline{\delta}_{stator}}{\partial \theta_{s,\rho V_x r,2}}(\bar{i}_{stator}, \overline{M}_{abs,2}) \\
\frac{\partial \overline{\delta}_{stator}}{\partial \theta_{o,\rho V_x r,2}} &= \frac{\partial \overline{\delta}_{stator}}{\partial \theta_{o,\rho V_x r,2}}(\bar{i}_{stator}, \overline{M}_{abs,2}) \\
\frac{\partial \overline{\delta}_{stator}}{\partial \theta_{e,\rho V_x r,2}} &= \frac{\partial \overline{\delta}_{stator}}{\partial \theta_{e,\rho V_x r,2}}(\bar{i}_{stator}, \overline{M}_{abs,2})
\end{aligned} \tag{A.50}$$

$$\begin{aligned}
\frac{\partial \overline{\delta}_{stator}}{\partial n_{inc,2}} &= \frac{\partial \overline{\delta}_{stator}}{\partial n_{inc,2}}(\bar{i}_{stator}, \overline{M}_{abs,2}) \\
\frac{\partial \overline{\delta}_{stator}}{\partial \theta_{s,inc,2}} &= \frac{\partial \overline{\delta}_{stator}}{\partial \theta_{s,inc,2}}(\bar{i}_{stator}, \overline{M}_{abs,2}) \\
\frac{\partial \overline{\delta}_{stator}}{\partial \theta_{o,inc,2}} &= \frac{\partial \overline{\delta}_{stator}}{\partial \theta_{o,inc,2}}(\bar{i}_{stator}, \overline{M}_{abs,2}) \\
\frac{\partial \overline{\delta}_{stator}}{\partial \theta_{e,inc,2}} &= \frac{\partial \overline{\delta}_{stator}}{\partial \theta_{e,inc,2}}(\bar{i}_{stator}, \overline{M}_{abs,2})
\end{aligned} \tag{A.51}$$

$$
\begin{aligned}
\frac{\partial k_{b,3}}{\partial n_{\rho V_x r,2}} &= \frac{\partial k_{b,3}}{\partial n_{\rho V_x r,2}}(\bar{i}_{stator}, \overline{M}_{abs,2}) \\
\frac{\partial k_{b,3}}{\partial \theta_{s,\rho V_x r,2}} &= \frac{\partial k_{b,3}}{\partial \theta_{s,\rho V_x r,2}}(\bar{i}_{stator}, \overline{M}_{abs,2}) \\
\frac{\partial k_{b,3}}{\partial \theta_{o,\rho V_x r,2}} &= \frac{\partial k_{b,3}}{\partial \theta_{o,\rho V_x r,2}}(\bar{i}_{stator}, \overline{M}_{abs,2}) \\
\frac{\partial k_{b,3}}{\partial \theta_{e,\rho V_x r,2}} &= \frac{\partial k_{b,3}}{\partial \theta_{e,\rho V_x r,2}}(\bar{i}_{stator}, \overline{M}_{abs,2})
\end{aligned}
\tag{A.52}
$$

$$
\begin{aligned}
\frac{\partial k_{b,3}}{\partial n_{inc,2}} &= \frac{\partial k_{b,3}}{\partial n_{inc,2}}(\bar{i}_{stator}, \overline{M}_{abs,2}) \\
\frac{\partial k_{b,3}}{\partial \theta_{s,inc,2}} &= \frac{\partial k_{b,3}}{\partial \theta_{s,inc,2}}(\bar{i}_{stator}, \overline{M}_{abs,2}) \\
\frac{\partial k_{b,3}}{\partial \theta_{o,inc,2}} &= \frac{\partial k_{b,3}}{\partial \theta_{o,inc,2}}(\bar{i}_{stator}, \overline{M}_{abs,2}) \\
\frac{\partial k_{b,3}}{\partial \theta_{e,inc,2}} &= \frac{\partial k_{b,3}}{\partial \theta_{e,inc,2}}(\bar{i}_{stator}, \overline{M}_{abs,2})
\end{aligned}
\tag{A.53}
$$

The stator loss coefficient and deviation angle can then be altered as:

$$
\begin{aligned}
\overline{\omega}_{stator,altered} = \overline{\omega}_{stator} + & \frac{\partial \overline{\omega}_{stator}}{\partial n_{\rho V_x r,2}}(\Delta n_{\rho V_x r})_2 + \frac{\partial \overline{\omega}_{stator}}{\partial \theta_{s,\rho V_x r,2}}(\Delta \theta_{s,\rho V_x r})_2 + \\
& \frac{\partial \overline{\omega}_{stator}}{\partial \theta_{o,\rho V_x r,2}}(\Delta \theta_{o,\rho V_x r})_2 + \frac{\partial \overline{\omega}_{stator}}{\partial \theta_{e,\rho V_x r,2}}(\Delta \theta_{e,\rho V_x r})_2 + \\
& \frac{\partial \overline{\omega}_{stator}}{\partial n_{inc,2}}(\Delta n_{inc})_2 + \frac{\partial \overline{\omega}_{stator}}{\partial \theta_{s,inc,2}}(\Delta \theta_{s,inc})_2 + \\
& \frac{\partial \overline{\omega}_{stator}}{\partial \theta_{o,inc,2}}(\Delta \theta_{o,inc})_2 + \frac{\partial \overline{\omega}_{stator}}{\partial \theta_{e,inc,2}}(\Delta \theta_{e,inc})_2
\end{aligned}
\tag{A.54}
$$

$$
\begin{aligned}
\overline{\delta}_{stator,altered} = \overline{\delta}_{stator} + & \frac{\partial \overline{\delta}_{stator}}{\partial n_{\rho V_x r,2}}(\Delta n_{\rho V_x r})_2 + \frac{\partial \overline{\delta}_{stator}}{\partial \theta_{s,\rho V_x r,2}}(\Delta \theta_{s,\rho V_x r})_2 + \\
& \frac{\partial \overline{\delta}_{stator}}{\partial \theta_{o,\rho V_x r,2}}(\Delta \theta_{o,\rho V_x r})_2 + \frac{\partial \overline{\delta}_{stator}}{\partial \theta_{e,\rho V_x r,2}}(\Delta \theta_{e,\rho V_x r})_2 + \\
& \frac{\partial \overline{\delta}_{stator}}{\partial n_{inc,2}}(\Delta n_{inc})_2 + \frac{\partial \overline{\delta}_{stator}}{\partial \theta_{s,inc,2}}(\Delta \theta_{s,inc})_2 + \\
& \frac{\partial \overline{\delta}_{stator}}{\partial \theta_{o,inc,2}}(\Delta \theta_{o,inc})_2 + \frac{\partial \overline{\delta}_{stator}}{\partial \theta_{e,inc,2}}(\Delta \theta_{e,inc})_2
\end{aligned}
\tag{A.55}
$$

The blockage is not yet altered because the stator outlet blockage is set by the stator outlet conditions which themselves depend on the blockage. This requires an iteration loop to converge on the station 3 conditions. The blockage will be altered for the impact of stator inlet radial flow non-uniformity inside the iteration loop.

A.2.3 Station 3 Stagnation Conditions and Flow Angle

The station 3 flow angle and absolute stagnation pressure and temperature can be calculated prior to entering the iteration loop. The stator outlet flow angle can be calculated using the altered deviation and stator exit metal angle:

$$\alpha_3 = \chi_{outlet,stator} + \overline{\delta}_{stator,altered} \tag{A.56}$$

There is no work done on the fluid across the stator so the absolute stagnation temperature is unchanged across the blade row ($T_{t,3} = T_{t,2}$). The stator outlet absolute stagnation pressure can be determined from the loss coefficient:

$$P_{t,3} = P_{t,2} - \overline{\omega}_{stator,altered}(P_{t,2} - P_2) \tag{A.57}$$

A.2.4 Iteration Loop for Station 3 Blockage

In order to determine the remaining station 3 quantities, the axial velocity $V_{x,3}$ is iterated upon. An initial guess is made, and the stator outlet absolute Mach number is calculated as:

$$M_{abs,3} = \sqrt{\frac{1}{\frac{V_{x,3}^2(1+tan(\alpha_3)^2)}{\gamma R T_{t,3}} - \frac{\gamma-1}{2}}} \tag{A.58}$$

The stator outlet static temperature and pressure are given by:

$$T_3 = \frac{T_{t,3}}{1 + \frac{\gamma-1}{2} M_{abs,3}^2} \tag{A.59}$$

$$P_3 = \frac{P_{t,3}}{(\frac{T_{t,3}}{T_3})^{\frac{\gamma}{\gamma-1}}} \tag{A.60}$$

The magnitude of the velocity in the absolute frame is given by $V_3 = M_{abs,3}\sqrt{\gamma R T_3}$, and the flow coefficient is then $\phi_3 = \frac{V_{x,3}}{U_3}$, where U_3 is the blade speed calculated using the stator exit meanline radius. The relative flow angle is given by:

$$\beta_3 = atan\left(\frac{1 - \phi_3 tan(\alpha_3)}{\phi_3}\right) \tag{A.61}$$

The incidence of the downstream rotor is then the difference between relative flow angle and blade inlet metal angle, $\bar{i}_{downstream\ rotor} = \beta_3 - \chi_{inlet,downstream\ rotor}$. The relative velocity at the rotor exit is given by $W_3 = \frac{V_{x,3}}{cos(\beta_3)}$, and the relative Mach number at station 3 is then $\overline{M_{rel,3}} = \frac{W_3}{\sqrt{\gamma R T_3}}$.

With blade row outlet incidence and relative Mach number known, the blade row outlet blockage factor is calculated from the database as $k_{b,3} = k_{b,3}(\bar{i}_{downstream\ rotor}, \overline{M}_{rel,3})$. In this case the blade row outlet station is at a rotor inlet, so the Mach number used in the database representation is in the rotating reference frame. The blockage is altered for the impact of the stator inlet non-uniformity:

$$\begin{aligned} k_{b,3,altered} = k_{b,3} + & \frac{\partial k_{b,3}}{\partial n_{\rho V_x r,2}}(\Delta n_{\rho V_x r})_2 + \frac{\partial k_{b,3}}{\partial \theta_{s,\rho V_x r,2}}(\Delta \theta_{s,\rho V_x r})_2 + \\ & \frac{\partial k_{b,3}}{\partial \theta_{o,\rho V_x r,2}}(\Delta \theta_{o,\rho V_x r})_2 + \frac{\partial k_{b,3}}{\partial \theta_{e,\rho V_x r,2}}(\Delta \theta_{e,\rho V_x r})_2 + \\ & \frac{\partial k_{b,3}}{\partial n_{inc,2}}(\Delta n_{inc})_2 + \frac{\partial k_{b,3}}{\partial \theta_{s,inc,2}}(\Delta \theta_{s,inc})_2 + \\ & \frac{\partial k_{b,3}}{\partial \theta_{o,inc,2}}(\Delta \theta_{o,inc})_2 + \frac{\partial k_{b,3}}{\partial \theta_{e,inc,2}}(\Delta \theta_{e,inc})_2 \end{aligned} \tag{A.62}$$

The meanline $(\overline{\rho V_x r})_3$ is calculated from the blockage factor using Equation A.42. Equation A.37 is adapted for use in the absolute frame and solved for $V_{x,3}$:

$$V_{x,3} = \frac{(\overline{\rho V_x r})_3 R T_{t,3}\left(1 + \frac{\gamma-1}{2}\left(\frac{1}{\frac{\gamma R T_{t,3}}{V_{x,3}^2(1+tan^2(\alpha_3))} - \frac{\gamma-1}{2}}\right)\right)^{\frac{1}{\gamma-1}}}{P_{t,3} r_{mean,3}} \tag{A.63}$$

If the $V_{x,3}$ determined using this equation is not equal to the initial guess, the process is repeated with an updated initial guess until the values converge.

A.2.5 Station 3 Non-Uniformity

With the relative Mach number and downstream rotor incidence known, the datum shape parameters can be calculated using the databases:

$$\begin{aligned}
n_{\rho V_x r,datum,3} &= n_{\rho V_x r,datum,3}(\bar{i}_{downstream\ rotor}, \overline{M}_{rel,3}) \\
\theta_{s,\rho V_x r,datum,3} &= \theta_{s,\rho V_x r,datum,3}(\bar{i}_{downstream\ rotor}, \overline{M}_{rel,3}) \\
\theta_{o,\rho V_x r,datum,3} &= \theta_{o,\rho V_x r,datum,3}(\bar{i}_{downstream\ rotor}, \overline{M}_{rel,3}) \\
\theta_{e,\rho V_x r,datum,3} &= \theta_{e,\rho V_x r,datum,3}(\bar{i}_{downstream\ rotor}, \overline{M}_{rel,3}) \\
n_{inc,datum,3} &= n_{inc,datum,3}(\bar{i}_{downstream\ rotor}, \overline{M}_{rel,3}) \\
\theta_{s,inc,datum,3} &= \theta_{s,inc,datum,3}(\bar{i}_{downstream\ rotor}, \overline{M}_{rel,3}) \\
\theta_{o,inc,datum,3} &= \theta_{o,inc,datum,3}(\bar{i}_{downstream\ rotor}, \overline{M}_{rel,3}) \\
\theta_{e,inc,datum,3} &= \theta_{e,inc,datum,3}(\bar{i}_{downstream\ rotor}, \overline{M}_{rel,3})
\end{aligned} \tag{A.64}$$

And the station 3 shape parameters are given by:

$$\begin{aligned}
n_{\rho V_x r,3} &= n_{\rho V_x r,datum,3} + (\Delta n_{\rho V_x r})_3 \\
\theta_{s,\rho V_x r,3} &= \theta_{s,\rho V_x r,datum,3} + (\Delta \theta_{s,\rho V_x r})_3 \\
\theta_{o,\rho V_x r,3} &= \theta_{o,\rho V_x r,datum,3} + (\Delta \theta_{o,\rho V_x r})_3 \\
\theta_{e,\rho V_x r,3} &= \theta_{e,\rho V_x r,datum,3} + (\Delta \theta_{e,\rho V_x r})_3 \\
n_{inc,3} &= n_{inc,datum,3} + (\Delta n_{inc})_3 \\
\theta_{s,inc,3} &= \theta_{s,inc,datum,3} + (\Delta \theta_{s,inc})_3 \\
\theta_{o,inc,3} &= \theta_{o,inc,datum,3} + (\Delta \theta_{o,inc})_3 \\
\theta_{e,inc,3} &= \theta_{e,inc,datum,3} + (\Delta \theta_{e,inc})_3
\end{aligned} \tag{A.65}$$

All values required as inlet conditions for the downstream rotor are now known.